



Laser frequency stabilization to spectral hole burning frequency references in erbium-doped crystals :
material and device optimization
by Thomas Bottger

A dissertation submitted in partial fulfillment of the requirements for the degree of Doctor of
Philosophy in Physics
Montana State University
© Copyright by Thomas Bottger (2002)

Abstract:

Narrow spectral holes in the absorption lines of Er^{3+} doped crystals have been explored as references for frequency stabilizing external cavity diode lasers at the important $1.5 \mu\text{m}$ optical communication wavelength. Allan deviations of the beat signal between two independent stabilized lasers as low as 200 Hz over 10 ms integration time have been achieved using regenerative spectral holes in $\text{Er}^{3+}:\text{Y}_2\text{SiO}_5$ and $\text{Er}^{3+}:\text{KTP}$, while drift was reduced to $\sim 7 \text{ kHz/min}$ by incorporating the inhomogeneous absorption line as a fixed reference. During active stabilization, the transient spectral hole was continuously regenerated as hole burning balanced relaxation. In contrast, persistent spectral holes in $\text{Er}^{3+}:\text{D}^{\text{e}}:\text{CaF}_2$, with lifetimes of several weeks, provided programmable and transportable secondary frequency references that maintained sub-kilohertz stability over several seconds and enabled 6 kHz stability over $1.6 \times 10^3 \text{ s}$. The error signal was derived from the spectral hole transmission using frequency modulation spectroscopy. A servo amplifier applied fast frequency corrections to the injection current of the laser diode and slower adjustments to the piezo-driven feedback prism plate.

These stabilized lasers provide ideal sources for spectral hole burning applications based on optical coherent transients, where laser stability is required over the storage time of the material. Since the lifetime of the frequency reference is exactly the material storage time, this requirement is automatically met by using our technique. This was demonstrated in $\text{Er}^{3+}:\text{Y}_2\text{SiO}_5$ and successfully transferred to high-bandwidth signal processing applications.

The material $\text{Er}^{3+}:\text{Y}_2\text{SiO}_5$ was optimized for these applications. The $4I_{15/2}$ and $4I_{13/2}$ crystal field levels were site-selectively determined by absorption and fluorescence spectroscopy. The excited state lifetime was measured to be 11.4 ms for site 1 and 9.2 ms for site 2. Zeeman experiments and two-pulse photon echo spectroscopy as a function of magnetic field orientation were used to determine the anisotropic electronic g-values for both Er^{3+} sites and established a preferred magnetic field orientation for minimizing homogeneous line broadening by spectral diffusion. The spectral diffusion was characterized by stimulated photon echo spectroscopy and successfully described with established theories. In a 0.02 atomic percent $\text{Er}^{3+}:\text{Y}_2\text{SiO}_5$ crystal at $B = 0.8 \text{ T}$ and $T = 1.6 \text{ K}$, line broadening became significant after $10 \mu\text{s}$, increasing the homogeneous linewidth from 7.5 kHz to 75 kHz after $120 \mu\text{s}$. Spectral diffusion, primarily caused by direct phonon driven Er^{3+} spin-flips in the ground state, can be controlled to negligible levels with proper magnetic field strength and orientation, temperature, and erbium concentration. In optimizing $\text{Er}^{3+}:\text{Y}_2\text{SiO}_5$, the narrowest optical resonance in any solid-state material of 73 Hz was measured.

LASER FREQUENCY STABILIZATION TO SPECTRAL HOLE BURNING
FREQUENCY REFERENCES IN ERBIUM-DOPED CRYSTALS:
MATERIAL AND DEVICE OPTIMIZATION

by

Thomas Böttger

A dissertation submitted in partial fulfillment
of the requirements for the degree

of

Doctor of Philosophy

in

Physics

MONTANA STATE UNIVERSITY
Bozeman, Montana

April 2002

D378
B6591

APPROVAL

of a dissertation submitted by

Thomas Böttger

This dissertation has been read by each member of the dissertation committee and has been found to be satisfactory regarding content, English usage, format, citations, bibliographic style, and consistency, and is ready for submission to the College of Graduate Studies.

Rufus L. Cone, III

Rufus L. Cone
(Signature)

4/18/2002
(Date)

Approved for the Department of Physics

John C. Hermanson

JCH
(Signature)

4-19-02
(Date)

Approved for the College of Graduate Studies

Bruce R. McLeod

Bruce R. McLeod
(Signature)

4-22-02
(Date)

STATEMENT OF PERMISSION TO USE

In presenting this dissertation in partial fulfillment of the requirements for a doctoral degree at Montana State University, I agree that the Library shall make it available to borrowers under the rules of the Library. I further agree that copying of this dissertation is allowable only for scholarly purposes, consistent with "fair use" as prescribed in the U.S. Copyright Law. Requests for extensive copying or reproduction of this dissertation should be referred to Bell & Howell Information and Learning, 300 North Zeeb Road, Ann Arbor, Michigan 48106, to whom I have granted "the exclusive right to reproduce and distribute my dissertation in and from microform along with the non-exclusive right to reproduce and distribute my abstract in any format in whole or in part."

Signature Thomas B. [unclear]

Date 4-19-2002

ACKNOWLEDGMENTS

I want to thank my advisor, Prof. Rufus L. Cone, for the opportunity to work on this extraordinary project. I very much enjoyed the freedom and independence he gave me. He has been a major influence in my development as a physicist.

I would like to thank Dr. Yongchen Sun for teaching me rare earth spectroscopy and sharing his experimental expertise and Charles W. Thiel for assistance with the spectral diffusion theory and computer data acquisition. I also would like to thank Dr. Geoff J. Pryde who has been a coworker for two years on this project. My fellow lab mates, graduate students Gregory Reinemer and Todd L. Harris and postdoctoral researchers Nick Strickland, Flurin Könz, and Alain Braud all have contributed to my knowledge of physics. I'm greatly indebted to G. Casey Dodge, Dustin Rich and Norm Williams for their quality machining work, to Dr. Gregg W. Switzer and Prof. John L. Carlsten for sharing the initial laser design, and to Drs. Peter B. Sellin and Kevin S. Repasky for teaching me the basics of external cavity diode lasers and laser frequency stabilization. I thank Steve Kelly and Kevin Rosen in the MSU electronic shop for assistance in circuit board fabrication. I'm also grateful to Dr. C. Michael Jefferson of IBM Almaden Research Center for sharing circuit ideas, noise reduction techniques, as well as memorable days at Bridger Bowl.

A special thanks goes to my wife, Tini, who certainly has made the most sacrifices caused by my frequent absence from home and our years of separation. Her love and encouragement made this possible.

TABLE OF CONTENTS

LIST OF TABLES.....	viii
LIST OF FIGURES.....	ix
ABSTRACT.....	xvii
1. INTRODUCTION.....	1
Frequency Stabilized Lasers and Their Applications.....	4
Spectral Hole Burning and Optical Coherent Transients.....	7
Overview of the Dissertation.....	11
References	13
2. MATERIALS – BACKGROUND AND THEORY.....	18
Homogeneous and Inhomogeneous Broadening.....	20
Spectral Hole Burning.....	23
Photon Echoes.....	25
Two Pulse Photon Echo.....	26
Stimulated Photon Echo.....	29
References	31
3. LASER FREQUENCY STABILIZATION – BACKGROUND AND THEORY.....	33
Frequency Modulation Spectroscopy.....	33
Maximizing the Slope of the Error Signal.....	41
Measuring and Characterizing Laser Frequency Stability.....	49
Measurement Techniques.....	50
Frequency Domain-The Spectral Noise Density.....	53
Time Domain-The Allan Variance.....	56
The External Cavity Diode Laser.....	59
Principle of Operation.....	61
ECDL Construction and Characterization.....	63
ECDL Transducer Response.....	70
Spectral Noise Density of the free running ECDL.....	74
References	80

4. LASER FREQUENCY STABILIZATION TO SPECTRAL HOLES.....	83
Laser frequency stabilization to regenerative spectral holes in $\text{Er}^{3+}:\text{Y}_2\text{SiO}_5$	85
Methods and Apparatus.....	86
Results and Discussion.....	92
Incorporating the Absorption Line as a Fixed Reference.....	94
Improved Photon Echo Stability for Applications.....	100
Frequency response of a regenerative spectral hole	103
Methods and Apparatus.....	104
Discussion.....	107
Laser frequency stabilization to regenerative spectral holes in $\text{Er}^{3+}:\text{KTP}$	109
Methods and Apparatus.....	110
Results and Discussion.....	113
Conclusions.....	116
Laser frequency stabilization to persistent spectral holes in $\text{Er}^{3+}:\text{D CaF}_2$	117
Methods and Apparatus.....	117
Results and Discussion.....	122
Conclusion.....	126
References	128
5. SPECTROSCOPY AND DYNAMICS OF $\text{Er}^{3+}:\text{Y}_2\text{SiO}_5$	132
Introduction and Motivation.....	132
Conventional spectroscopy.....	136
Methods and Apparatus.....	136
Results and Discussion.....	140
Lifetime Measurements.....	145
Methods and Apparatus.....	146
Results and Discussion.....	148
Zeeman experiments.....	151
Methods and Apparatus.....	156
The Zeeman Effect.....	160
Zeeman Experiments as a Function of Field Orientation.....	162
Results.....	163
Discussion.....	173
Nonlinear Spectroscopy.....	180
Methods and Apparatus.....	180
Two-Pulse Photon Echo Spectroscopy as a Function of Field Orientation.....	183
Results.....	184

Discussion.....	187
Stimulated Photon Echo Spectroscopy and Spectral Diffusion.....	191
Results.....	193
Discussion of Spectral Diffusion in 0.02% $\text{Er}^{3+}:\text{Y}_2\text{SiO}_5$ as a Function of Magnetic Field.....	199
Discussion of Spectral Diffusion in 0.02% $\text{Er}^{3+}:\text{Y}_2\text{SiO}_5$ as a Function of Temperature.....	204
Discussion of Spectral Diffusion in $\text{Er}^{3+}:\text{Y}_2\text{SiO}_5$ as a Function of Erbium Concentration.....	205
Stimulated Photon Echo T -Decays.....	206
Results and Discussion.....	208
Ultraslow Dephasing.....	211
Results and Discussion.....	211
Operation of $\text{Er}^{3+}:\text{Y}_2\text{SiO}_5$ at elevated temperatures.....	213
Results and Discussion.....	214
References	218
 6. SUMMARY.....	 221
 APPENDICES.....	 227
 APPENDIX A – ELECTRONIC FEEDBACK.....	 228
 APPENDIX B – REFERENCE CAVITY.....	 251
 APPENDIX C – BAI-FAYER THEORY OF SPECTRAL DIFFUSION.....	 258
References	263

LIST OF TABLES

Table		Page
1	Common noise types found in frequency standards and their relation to the spectral noise density, $S_v(f)$, and Allan deviation, $\sigma_y(\tau)$	59
2	Crystal field levels of $\text{Er}^{3+}:\text{Y}_2\text{SiO}_5$ as determined from absorption and site selective fluorescence experiments.....	145
3	Fitted g-tensor values for ground and excited state of site 1 and 2 with respective orientations 1 and 2 in the three optical planes.....	172

LIST OF FIGURES

Figure	Page
2.1 Line broadening and spectral hole burning	22
2.2 A typical two pulse photon echo sequence.....	27
2.3 A typical stimulated photon echo pulse sequence.....	27
3.1 Block diagram of the experimental setup for frequency modulation (FM) spectroscopy based on phase sensitive detection.....	34
3.2 Spectrum of the electric field after passing the phase modulator.....	35
3.3 Calculated FM-signals for $\Gamma = 1$, $M = 1$, and $\omega_m = 10$	40
3.4 Calculated FM-signals for modulation index, $M = 1$, as a function of modulation frequency, ω_m	43
3.5 Calculated FM-signals for modulation frequency $\omega_m = 5$ as a function of frequency, the modulation index, M , varies between subplots.....	45
3.6 Calculated FM-signal slopes at line center as a function of modulation frequency, ω_m	47
3.7 Calculated FM-signal slopes at line center as a function of modulation index, M	48
3.8 Experimental setup to characterize the frequency stability of a laser using error signal analysis.....	51
3.9 Experimental setup to characterize the frequency stability of a laser using beat note analysis.....	51
3.10 Illustration of the power law model for the spectral noise density as a function of frequency (a) and the Allan	

deviation as a function of integration time (b).....	55
3.11 Schematic of the external cavity diode laser in the Littman-Metcalf configuration.....	64
3.12 ECDL-spectrum near 1535 nm showing a side-mode suppression ratio of ~ 51 dB.....	66
3.13 Optical output power versus injection current (PI curve) for the ECDL "Max".....	67
3.14 Continuous tuning curve for ECDL "Max". Continuous tuning is demonstrated over ~ 47 GHz, center wavelength ~ 1535 nm, I = 60 mA.....	69
3.15 Experimental setup used to measure the transducer response of the ECDL with a low finesse cavity as a frequency discriminator.....	71
3.16 Transducer response of the tuning elements of the ECDL.....	72
3.17 Experimental setup for measuring the spectral noise density of the free running laser.....	75
3.18 Spectral noise density of the free running ECDL as a function of noise frequency; note double logarithmic scales.....	78
4.1 Transmission spectrum of 0.005% Er ³⁺ :Y ₂ SiO ₅ scanned by a diode laser showing the entire inhomogeneously broadened absorption profile at zero applied field (B = 0 T).....	88
4.2 Experimental apparatus for laser frequency locking to spectral holes and beat frequency measurement of laser stability.....	90
4.3 (a) Transmission spectrum, as probed by a phase-modulated laser with sidebands, of a single spectral hole burned in the inhomogeneously broadened absorption profile by an unmodulated second laser, in an applied field of B = 0.2 T. (b) Error signals derived from the spectral hole and the inhomogeneous line using different	

phase delay settings.....	91
4.4 Allan deviation values for the beat between two lasers: (a) lasers free-running (triangles), (b) locked to spectral holes in different crystals using straight quadrature detection of the error signal at applied field $B = 0.5$ T (squares), and (c) locked to spectral holes using the strategy of intermediate phase detection of the combined error signal from the spectral hole and inhomogeneous line at applied field $B = 0.2$ T (circles).....	94
4.5 Change in heterodyne beat signal between (a) free-running and (b) independently locked lasers to separate spectral holes and inhomogeneous lines in different crystals at field $B = 0.2$ T.....	98
4.6 Stimulated photon echo decay on the ${}^4I_{15/2}(1) \rightarrow {}^4I_{13/2}(1)$ transition in $\text{Er}^{3+}:\text{Y}_2\text{SiO}_5$	102
4.7 Experimental setup used to measure the frequency response of a regenerative spectral hole in 0.001 % $\text{Er}^{3+}:\text{Y}_2\text{SiO}_5$	105
4.8 Frequency response of the error signal generated from a regenerative spectral hole frequency reference in 0.001 % $\text{Er}^{3+}:\text{Y}_2\text{SiO}_5$	108
4.9 (a) Transmission spectrum of 0.004 % $\text{Er}^{3+}:\text{KTP}$ at 1537 nm showing the entire inhomogeneously broadened ${}^4I_{15/2} \rightarrow {}^4I_{13/2}$ optical absorption scanned by a diode probe laser. The arrow indicates a spectral hole, which has been burned by a second laser. (b) Transmission of a phase-modulated probe laser through a single spectral hole created by a second laser, using an applied magnetic field of $B=0.25$ T. (c) Demodulated FM-error signal derived from the spectral hole in (b)	111
4.10 Allan deviation for the heterodyne beat frequency between two lasers: (a) lasers free-running, (b) independently locked to transient spectral holes in the ${}^4I_{15/2} \rightarrow {}^4I_{13/2}$ transition in $\text{Er}^{3+}:\text{KTP}$ at 1537 nm.....	114
4.11 (a) Transmission spectrum of $\text{Er}^{3+}:\text{D}:\text{CaF}_2$ at 1523 nm. A number of spectral holes have been burned into the	

inhomogeneously broadened ${}^4I_{15/2} \rightarrow {}^4I_{13/2}$ optical absorption for demonstrating the programmability of the material. Spectral hole burning is not limited to the center of the line. The arrow indicates a spectral hole, which is enlarged in (b). (c) Demodulated FM-error signal derived from the spectral hole in (b).....	120
4.12 Root Allan variance for the heterodyne beat frequency between two lasers: (a) lasers free-running, (b) independently locked to persistent spectral holes in the ${}^4I_{15/2} \rightarrow {}^4I_{13/2}$ transition in $\text{Er}^{3+}:\text{D}:\text{CaF}_2$ at 1523 nm.....	123
4.13 Subset of the change in heterodyne beat frequency between (a) free running and (b) independently locked lasers to persistent spectral holes in separate crystals over a period of 10 minutes.....	125
5.1 Experimental setup for broadband absorption and site-selective fluorescence.....	137
5.2 Polarized $E // D_2$ lamp absorption spectrum of 2% $\text{Er}^{3+}:\text{Y}_2\text{SiO}_5$ at $T = 1.95 \text{ K}$	141
5.3 Site selective fluorescence spectra of 0.001 % $\text{Er}^{3+}:\text{Y}_2\text{SiO}_5$ at $T = 10 \text{ K}$; linecenters are given in wavenumbers.	143
5.4 Crystal field levels of ${}^4I_{15/2}$ and ${}^4I_{13/2}$ multiplets of $\text{Er}^{3+}:\text{Y}_2\text{SiO}_5$ as determined from absorption and site selective fluorescence excitation for site 1 and site 2.....	144
5.5 Experimental setup to measure the ${}^4I_{13/2}$ fluorescence lifetime for $\text{Er}^{3+}:\text{Y}_2\text{SiO}_5$	147
5.6 Fluorescence lifetime decay for 0.001% $\text{Er}^{3+}:\text{Y}_2\text{SiO}_5$ ${}^4I_{13/2}(Y_1) \rightarrow {}^4I_{15/2}(Z_1)$ transition at $T = 10 \text{ K}$	149
5.7 Transition labelling scheme in Zeeman laser absorption experiments.....	153
5.8 Projections of the magnetic field B onto the primary \tilde{g} -tensor axes for the case of B lying in the $b\text{-}D_I$ plane	155

5.9	Experimental setup for laser Zeeman absorption; ECDL 2 serves to calibrate the optical frequency.....	157
5.10	Experimental configuration for full rotational Zeeman measurements illustrated for the D_1 - D_2 plane.....	158
5.11	Laser absorption Zeeman spectra for 0.001 % $\text{Er}^{3+}:\text{Y}_2\text{SiO}_5$ as a function of magnetic field for $\mathbf{B} // \mathbf{D}_1$, $\mathbf{k} // \mathbf{b}$ at $T = 10$ K.....	161
5.12	Angle dependent Zeeman laser absorption scans, with the B-field in \mathbf{b} - D_2 plane.....	164
5.13	(a) Orientational-dependent g values of magnetically inequivalent orientations of site 2 in the \mathbf{b} - D_2 plane determined from data of (b).....	166
5.14	(a) Orientational-dependent g values of magnetically inequivalent orientations of site 1 in the \mathbf{b} - D_2 plane determined from data of (b).....	167
5.15	(a) Orientational-dependent g values of magnetically inequivalent orientations of site 1 in the \mathbf{b} - D_1 plane determined from data of (b).....	168
5.16	(a) Orientational-dependent g values of magnetically inequivalent orientations of site 2 in the \mathbf{b} - D_1 plane determined from data of (b).....	169
5.17	(a) Full orientational dependent g values of site 1 in the D_1 - D_2 plane determined from data of (b).....	170
5.18	(a) Orientational-dependent g values of site 2 in the D_1 - D_2 plane determined from data of (b).....	171
5.19	Schematic of the spin flip broadening mechanism in $\text{Er}^{3+}:\text{Y}_2\text{SiO}_5$	174
5.20	Schematic of the direct phonon process in the Zeeman split Er^{3+} ground state.....	177
5.21	Experimental setup to measure two pulse photon echoes, stimulated echoes and optical nutation with a spectral hole stabilized laser.....	181

- 5.22 (a) Orientation-dependent g values of site 1 and site 2 in the D_1 - D_2 plane, g_{1g} denotes the g value for the ground state of site 1, g_{2e} the g value for the excited state of site 2, etc.; solid lines are fits to the data. (b) Correlation with the homogeneous linewidth of site 1 measured with two pulse echoes in the D_1 - D_2 plane as a function of magnetic field orientation.....185
- 5.23 (a) Orientational dependent g values of site 1 and 2 sub-sites in the b - D_2 plane, g_{1g} denotes the g value for the ground state of orientation 1, g_{2e} the g value for the excited state of orientation 2, etc.; solid lines are fits to the data. (b) Correlation with the homogeneous linewidth of site 1 orientation 2 measured with two-pulse photon echoes in the b - D_2 plane as a function of magnetic field orientation.....186
- 5.24 Energy level structure of $\text{Er}^{3+}:\text{Y}_2\text{SiO}_5$ at a magnetic field of $B = 3$ T with angle $\Phi = 95^\circ$ between B and D_1189
- 5.25 Stimulated photon echo decays in 0.02 % $\text{Er}^{3+}:\text{Y}_2\text{SiO}_5$ at a magnetic field of $B = 1.75$ T at 1.6 K as the waiting time T is varied between 0 μs (equivalent to a two-pulse photon echo decay) and 5000 μs194
- 5.26 Evolution of the homogeneous linewidth of site 1 in 0.02 % $\text{Er}^{3+}:\text{Y}_2\text{SiO}_5$ at 1.6 K as the waiting time, T , between pulses two and three is varied in a stimulated photon echo measurement.....195
- 5.27 Evolution of the homogeneous linewidth of site 1 in 0.02 % $\text{Er}^{3+}:\text{Y}_2\text{SiO}_5$ at $B = 2.25$ T as the waiting time, T , between pulses two and three is varied in a stimulated photon echo measurement.....196
- 5.28 Evolution of the homogeneous linewidth of site 1 in 0.1 % $\text{Er}^{3+}:\text{Y}_2\text{SiO}_5$ at 1.6 K as the waiting time, T , between pulses two and three is varied in a stimulated photon echo measurement.....197

5.29 Evolution of the homogeneous linewidth of site 1 in 0.001 % $\text{Er}^{3+}\text{Y}_2\text{SiO}_5$ at 1.6 K as the waiting time, T , between pulses two and three is varied in a stimulated photon echo measurement.....198

5.30 (a) Relaxation rate, R , as a function of magnetic field as measured in 0.02 % $\text{Er}^{3+}\text{Y}_2\text{SiO}_5$ at 1.6 K. Solid lines are least square fits using the expression (5.15) and show excellent agreement; fitting parameters are given in the figure. (b) Saturated spectral diffusion linewidth, Γ_1 , for long waiting times, T , as a function of magnetic field in 0.02 % $\text{Er}^{3+}\text{Y}_2\text{SiO}_5$ at 1.6 K. Data points were fitted to expression (5.14) and show good agreement. Fitting parameters are given in the figure.....203

5.31 Stimulated echo T-decays in 0.001% $\text{Er}^{3+}\text{Y}_2\text{SiO}_5$ at $T = 1.6$ K, $\mathbf{B} // \mathbf{D}_1$, $\mathbf{k} // \mathbf{b}$ as a function of time delay, T , between pulse two and three.....209

5.32 Two-pulse photon echo decay in 0.001% $\text{Er}^{3+}\text{Y}_2\text{SiO}_5$ at $B = 7$ T, $T = 1.5$ K, the lasers \mathbf{k} vector is parallel to \mathbf{b} and \mathbf{B} is in the \mathbf{D}_1 - \mathbf{D}_2 plane at an angle of $\Phi = 140^\circ$ to the \mathbf{D}_1 axis.....212

5.33 (a) Two-pulse photon echo decays measured in 0.005% $\text{Er}^{3+}\text{Y}_2\text{SiO}_5$ as a function of temperature for a fixed magnetic field strength of $B = 2$ T, $\mathbf{k} // \mathbf{b}$, $\mathbf{B} // \mathbf{D}_1$. Solid lines are fits to expression (2.5) to extract the homogeneous linewidth; each case shows excellent agreement. (b) Homogeneous linewidths as a function of temperature obtained from (a), the solid line serves to guide the eye.....215

5.34 Evolution of the linewidth of site 1 in 0.005% $\text{Er}^{3+}\text{Y}_2\text{SiO}_5$ at $T = 4.2$ K and $B = 3$ T as the waiting time, T , between pulse two and three is varied in a stimulated photon echo measurement.....216

A.1 Conceptual block diagram of the laser frequency stabilization system.....230

A.2 Block diagram of the diode laser frequency stabilization Apparatus.....233

A.3	Electronic schematic of the diode laser injection current servo (1 MHz bandwidth).....	235
A.4	Electronic schematics of the PZT servo (low bandwidth).....	238
A.5	Electronic schematic of the bridged-T notch filter.....	240
A.6	Electronic schematic of the resonant EOM-tank circuit.....	242
A.7	Electronic schematic of the post-mixer amplifier.....	244
A.8	Electronic schematic of the RF phaseshifter (first part).....	246
A.9	Electronic schematic of the RF phase shifter (second part).....	247
A.10	Electronic schematic of the low noise diode laser driver; arrows indicate the signal flow.....	249
B.1	Electronic schematic for cavity-ringdown measurements.....	255
B.2	(a) Cavity-ringdown (lifetime) measurement, straight line is a least square fit exponential fit to the data. (b) Transmission spectrum of the TEM ₀₀ mode matched cavity showing one full free spectral range (FSR).....	257
C.1	Two-level system with energy splitting, $\Delta E = \mu B$, and populations in the upper (lower) state, ρ_{++} (ρ_{--}) employed in the Bai-Fayer theory.....	259

ABSTRACT

Narrow spectral holes in the absorption lines of Er^{3+} doped crystals have been explored as references for frequency stabilizing external cavity diode lasers at the important $1.5 \mu\text{m}$ optical communication wavelength. Allan deviations of the beat signal between two independent stabilized lasers as low as 200 Hz over 10 ms integration time have been achieved using regenerative spectral holes in $\text{Er}^{3+}:\text{Y}_2\text{SiO}_5$ and $\text{Er}^{3+}:\text{KTP}$, while drift was reduced to $\sim 7 \text{ kHz/min}$ by incorporating the inhomogeneous absorption line as a fixed reference. During active stabilization, the transient spectral hole was continuously regenerated as hole burning balanced relaxation. In contrast, persistent spectral holes in $\text{Er}^{3+}:\text{D}:\text{CaF}_2$, with lifetimes of several weeks, provided programmable and transportable secondary frequency references that maintained sub-kilohertz stability over several seconds and enabled 6 kHz stability over $1.6 \times 10^3 \text{ s}$. The error signal was derived from the spectral hole transmission using frequency modulation spectroscopy. A servo amplifier applied fast frequency corrections to the injection current of the laser diode and slower adjustments to the piezo-driven feedback prism plate.

These stabilized lasers provide ideal sources for spectral hole burning applications based on optical coherent transients, where laser stability is required over the storage time of the material. Since the lifetime of the frequency reference is exactly the material storage time, this requirement is automatically met by using our technique. This was demonstrated in $\text{Er}^{3+}:\text{Y}_2\text{SiO}_5$ and successfully transferred to high-bandwidth signal processing applications.

The material $\text{Er}^{3+}:\text{Y}_2\text{SiO}_5$ was optimized for these applications. The $^4\text{I}_{15/2}$ and $^4\text{I}_{13/2}$ crystal field levels were site-selectively determined by absorption and fluorescence spectroscopy. The excited state lifetime was measured to be 11.4 ms for site 1 and 9.2 ms for site 2. Zeeman experiments and two-pulse photon echo spectroscopy as a function of magnetic field orientation were used to determine the anisotropic electronic g-values for both Er^{3+} sites and established a preferred magnetic field orientation for minimizing homogeneous line broadening by spectral diffusion. The spectral diffusion was characterized by stimulated photon echo spectroscopy and successfully described with established theories. In a 0.02 atomic percent $\text{Er}^{3+}:\text{Y}_2\text{SiO}_5$ crystal at $B = 0.8 \text{ T}$ and $T = 1.6 \text{ K}$, line broadening became significant after $10 \mu\text{s}$, increasing the homogeneous linewidth from 7.5 kHz to 75 kHz after $120 \mu\text{s}$. Spectral diffusion, primarily caused by direct phonon driven Er^{3+} spin-flips in the ground state, can be controlled to negligible levels with proper magnetic field strength and orientation, temperature, and erbium concentration. In optimizing $\text{Er}^{3+}:\text{Y}_2\text{SiO}_5$, the narrowest optical resonance in any solid-state material of 73 Hz was measured.

CHAPTER 1

INTRODUCTION

Many classes of solids have inhomogeneously broadened optical absorption lines. When a narrow spectral region in such a material is saturated by a laser, notches, called spectral holes, are "burned" into the line shape, either transiently or persistently modifying the optical properties of the medium. At low temperatures, these holes have useful lifetimes ranging from fractions of a second to weeks or longer, and these narrow features have been widely used for spectroscopy at Montana State University, IBM, and elsewhere. The transient or persistent modification of optical properties that arises from spectral hole burning (SHB) also offers opportunities to build powerful and interesting devices for signal processing or data storage. Many of these devices rely on a combination of spectral hole burning and extensions of the concepts of holography to the time domain, leading to holography in "four dimensions".

In this research, the ultra-narrow resonances provided by spectral holes have been exploited as references for frequency stabilization of external cavity diode lasers (ECDL). In particular, Er^{3+} doped materials that exhibit SHB in the important optical communication band at $1.5 \mu\text{m}$ were investigated. Relatively short-lived (transient) spectral holes with lifetimes of $T_1 \sim 10 \text{ ms}$ and kilohertz hole linewidths supplied frequency references that provided stabilities over timescales that are

especially appropriate for coherent nonlinear spectroscopy and SHB device applications. [1, 2] Continuously regenerated, lifetime-limited (regenerative) spectral hole frequency references in $\text{Er}^{3+}:\text{Y}_2\text{SiO}_5$ produced laser frequency stabilities (Allan Deviation) of 500 Hz over 2 ms. [3] Further system development allowed improvement to 200 Hz over 5 ms using regenerative spectral hole frequency references in $\text{Er}^{3+}:\text{KTP}$. [4, 5] Persistent spectral holes in $\text{Er}^{3+}:\text{CaF}_2$, with lifetimes of several weeks, permitted extension of laser frequency stability to longer integration times, achieving stabilities of 6 kHz over 1600 s while maintaining sub-kilohertz stabilities over integration times of several seconds. [6]

For SHB applications using materials optimized for correlators or memories, stable laser sources are required at wavelengths and timescales specific to each individual material. We have demonstrated that using a spectral hole in a separate spatial region or a separate piece of the SHB correlator or memory material automatically provides frequency references meeting these requirements. Together with previously developed 793nm laser systems [7, 8], these 1.5 μm lasers stabilized to spectral holes have been successfully transferred to SHB correlator devices at the Montana State University Spectrum Lab, Cone lab, and Babbitt lab. [9, 10]

The material $\text{Er}^{3+}:\text{Y}_2\text{SiO}_5$ plays an important role in the arena of SHB devices covering the telecommunication band at 1.5 μm . [11] It has been used for SHB proof-of-principle demonstrations at Montana State University such as real-time address header decoding for optical data routing [12] and spatial-spectral holographic correlation. [13] Very recently, the improved material and laser

frequency stabilization that is reported in this thesis allowed demonstration of much higher bandwidth (500 MHz) analog signal processing at temperatures of 4.2 K. [10] Other research groups around the world, including the University of Colorado, the Laboratoire Aimé Cotton, Orsay, France, and the Australian National University, are already using this material to develop SHB applications that will include massively parallel computing, radio frequency spectrum analysis [14], electromagnetically induced transparency, and quantum information demonstrations [15] based on our development.

The importance of $\text{Er}^{3+}:\text{Y}_2\text{SiO}_5$ for SHB applications provided the motivation for fundamental research to further explore the parameters that influence materials critical to these applications. Spectroscopic investigations using conventional and coherent nonlinear methods allowed the characterization and optimization of the spectral hole burning in the $\text{Er}^{3+}:\text{Y}_2\text{SiO}_5$ material [16] and have led to the measurement of a 73 Hz linewidth, the narrowest optical resonance, to the best of our knowledge, in any solid-state material. Furthermore, the methods developed during the material optimization are directly applicable to other Er^{3+} doped compounds. These studies have advanced our fundamental understanding of these materials.

Frequency Stabilized Lasers and Their Applications

Many applications require laser frequency stability that is impossible to achieve with a free-running laser. Fortunately, dramatic stabilization is possible with an external frequency reference and feedback control of the laser cavity. Such lasers find widespread and important uses. Laser frequency stabilization is important in long-baseline interferometry for gravitational wave detection [17], ultrahigh-resolution spectroscopy of solids, molecules, and atoms [18], optical communication systems [19], for solid state optoelectronic devices based on spectral hole burning (SHB) [20] such as GHz-scale time-domain optical signal processing [21, 22, 13, 9] and network packet switching [23, 12], for precision laser ranging, for spatial coordination of satellite arrays, and for optical communication using coherent light detection. These stabilized lasers are also suitable for sensitive vibration monitoring devices and a variety of other optical and fiber optical sensors.

One of the most prominent applications for which stable laser sources are being developed is optical frequency standards based on trapped ions [24, 25, 26, 27, 28] and neutral atoms [29, 30], particles which are nearly at rest in the laboratory frame, eliminating Doppler effects while producing very narrow, several-Hz-wide resonance lines. Recent developments suggest that an optical frequency clock can offer significant improvement over the resolution of the current Cesium microwave atomic clock. In the tera-hertz domain, optical frequencies provide four orders of magnitude higher operating frequencies than microwave references, while the higher

quality factors of optical reference transitions allow determination of center frequencies to greater precision. The recent advent of air-silica microstructure optical fiber, which broadens the frequency comb of a femtosecond laser to span the optical octave from 532 nm to 1064 nm, furthers the trend toward an all-optical frequency standard. For the first time, optical frequencies in the 10^{15} Hz range can be directly measured and compared to microwave standards [31, 32, 33, 34] without the use of elaborate frequency chains. These new techniques will likely lead to new, super-accurate clocks based on optical frequencies, with projected performance approaching 10^{-18} accuracy. In addition, a stable frequency in the radio frequency (RF) domain can now be derived with improved accuracy using an optical standard. Recent reviews of the field can be found in Ref. [35, 36]. The basic ideas how to build an optical frequency standard apply to any laser source to be stabilized.

In order to achieve an optical frequency standard, the laser system must include the optical frequency reference, must maintain a single spatial and frequency mode, and have an actuator that allows frequency tuning with sufficient bandwidth to suppress the intrinsic laser noise so that the laser's short-term linewidth can be narrowed to allow interrogation of the optical reference transition. The lasers' long-term stability derives from the optical frequency reference.

Pre-stabilizing a laser to a reflection mode of a Fabry-Perot cavity often achieves this goal. These laser clocks, frequently called flywheel oscillators, provide a cavity-derived reference with sufficient short-term stability to interrogate the atomic or ion optical frequency standard of interest. While our research goal did not encompass the

development of absolute frequency standards, our lasers stabilized to spectral hole frequency references have already been considered to become flywheel oscillators of an optical frequency standard [37].

During the 1980's, a number of technical developments made Fabry-Perot cavities an attractive choice to achieve an ultra-stable laser. The Pound-Drever-Hall technique [38], a detection scheme capable of exploiting the narrow linewidth of a high finesse cavity, proved to be the most effective method of locking a laser to a cavity. The lowest *relative* instability for a laser that is frequency locked to a cavity reached 8×10^{-17} , measured by locking two lasers to adjacent modes of a single Fabry-Perot. [39] The main problem associated with Fabry-Perot cavities is vibration-induced and thermally-induced length changes. The thermal instability was reduced with introduction of Ultra Low Expansion (ULE) glass [40] or Zerodur [41] as cavity spacer materials, providing nearly zero thermal expansion, with expansion coefficient of $\alpha \approx 4 \times 10^{-8} / K$ at room temperature. Even more extreme measures have been undertaken in the work of Mlynek and Schiller *et al.* [42] by operating optical reference cavities at cryogenic temperatures to minimize thermal expansion, which is described by $\alpha \propto T^3$ for $T \rightarrow 0$, giving a value of $\alpha \approx 6 \times 10^{-13} T^3 / K$ in sapphire. Next, the development of very high finesse dielectric mirrors led to extremely narrow cavity linewidths, providing a very steep discriminator slope for a tight laser servo lock.

It was also appreciated that achieving a tight servo lock is necessary but not sufficient for an ultra-stable laser. The stability of the laser frequency can never

exceed that of the frequency reference. To assess real stability requires a second, independent reference cavity stabilized laser. The best *absolute* stability for cavity-stabilized lasers has been 3×10^{-16} [43], which is half an order of magnitude less than the 8×10^{-17} value mentioned previously.

Reduction of perturbations to the reference cavity, mainly due to temperature fluctuations and vibrations exciting mechanical modes or causing deformations of the cavity, has been the focus of much of the work in the past 15 years. Applying these considerations to practical systems should take into account cost, size, portability, and degree of complexity.

Spectral Hole Burning and Optical Coherent Transients

Spectral holes provide alternative references that are complimentary to precision atomic resonances or reflection modes of Fabry-Perot cavities. The relative immunity of the spectral hole reference to vibrational disturbances greatly simplifies the experimental setup. The entire system developed here fits on a 3' by 4' breadboard including optics, two sets of lasers, and feedback electronics, cryostat, and beat measurement for characterization. Further system development could lead to compact, transportable, stable laser sources based on SHB technology, miniaturized external cavity diode lasers, and mechanical closed-cycle cryo-coolers. Other state-of-the-art stable laser systems based on Fabry-Perot cavities and atomic resonances occupy several optical tables and require extreme isolation from the

environment to stabilize the local oscillator. [43] Note also that the best performance with traditional Fabry-Perot cavities, atomic or ion resonances requires cryogenic temperatures. [24, 42]

Spectral hole burning is a property found in certain materials, such as inorganic and organic solids, and Doppler broadened atomic vapors. Of particular interest for this research are rare earth doped solids, which exhibit an inhomogeneously broadened absorption at low temperatures. In particular, an individual homogeneous packet of rare earth ions in a crystalline or glassy solid manifests an absorption linewidth, known as the homogeneous linewidth, Γ_h . At optical frequencies and cryogenic temperatures, this width can be as narrow as 73 Hz, as reported in this work. These rare earth ion subgroups comprise part of the broader distribution of the strain-broadened absorption line described by the inhomogeneous linewidth, Γ_{inh} . Inhomogeneous linewidths in rare earth doped crystals range from sub-GHz values up to hundreds of GHz.

When ions are temporarily or permanently removed from the inhomogeneously broadened absorption, a spectral hole is produced. This selective bleaching of a particular subgroup of ions may occur when the ions are exposed to a narrow band laser. The process of producing a narrow spectral hole in the absorption line is called spectral hole burning. Spectral holes may be as narrow as $2\Gamma_h$, which can approach 100 Hz, so they provide resonances whose widths are competitive with those of super-cavities and isolated single atoms or ions.

The large difference between the magnitudes of inhomogeneous and homogeneous linewidths can be exploited in optical memories. In the frequency domain, the inhomogeneous line is subdivided into "frequency bins", with each bin having a potential minimum frequency width equal to the homogeneous linewidth. Binary information can be spectrally addressed while stored in the combination of either the presence (binary 1) or absence (binary 0) of a spectral hole. The approximate number of spectral holes burned in a single spatial location depends on the ratio of inhomogeneous to homogeneous linewidths, which has been measured to be as high as 10^8 in some materials. [44]

Spectral hole burning in the time domain leads to coherent phenomena, called optical coherent transients. The same rare earth materials can be used to store temporally structured, optical pulse patterns, with duration limited by the material coherence time, T_2 . Stored pulse patterns can be recalled temporally, leading to optical memory [45] with a storage duration determined by the material's hole burning mechanisms. Storage times can vary between milliseconds, in cases of two-level saturation or population bottlenecks formed by a metastable intermediate state, to several weeks, for optical pumping of hyperfine-split sublevels of the ground state or optically induced local ion site distortion. Stored pulse patterns can also be used for correlation with an incident optical data stream, which leads to optical processing. [46] Most applications of coherent transients use photon echoes, treated in detail in chapter 2. A review of memory, processing, and routing applications can be found in Ref. 47.

Stable laser technology accommodates frequency and time domain spectral hole burning applications as well as spectroscopy. Frequency domain applications reach their limit at the laser linewidth, often significantly larger than the associated homogeneous linewidth of the particular material. In memory applications, this causes considerable reduction of the possible number of holes burned into the inhomogeneous line, thus limiting the achievable storage capacity. For optimal exploitation of the photon echo and stimulated photon echo, which are the basis for time-domain spectroscopy and the associated range of proposed optical devices [47], laser frequency stability must exceed the spectral resolution needed to store the spectrum of the excitation pulse sequences. The entire pulse sequence length is limited by the storage duration for the material.

Lasers stabilized to spectral hole frequency references offer distinct advantages in frequency as well as time-domain spectral hole burning applications and spectroscopy. In stabilizing the laser to a spectral hole in a second piece of the same signal processing material, automatic frequency compatibility between the signal processing material and the stabilized laser source is provided. There is a natural correspondence between the timescales governing optical processing and laser frequency stabilization. The relative vibrational immunity of the spectral holes provides an important simplification in system design and performance, especially when both the frequency reference and spectroscopic sample or SHB device are mounted on the same platform.

Overview of the Dissertation

After this chapter of introduction, Chapter 2 discusses general rare earth material properties, spectral hole burning, and optical coherent transient phenomena.

Chapter 3 introduces the basic concepts of laser frequency stabilization. Special emphasis is placed on frequency modulation spectroscopy as well as methods of measurement and characterization of laser frequency stability. The external cavity diode laser system, built for all the research conducted, is described and characterized in this chapter.

Chapter 4 reports our results on laser frequency stabilization to regenerative spectral holes in $\text{Er}^{3+}:\text{Y}_2\text{SiO}_5$ and $\text{Er}^{3+}:\text{KTP}$, as well as persistent spectral holes in $\text{Er}^{3+}:\text{CaF}_2$. The reliability of stimulated photon echoes produced by a laser stabilized to a spectral hole, spatially separated in the same crystal, is demonstrated. Regenerative spectral holes, because of their limited lifetime, differ fundamentally from traditional frequency references. They are dynamic references. The interplay of the laser field with the dynamic hole reference was experimentally investigated.

Chapter 5 presents a study of the spectroscopic and dynamic properties of $\text{Er}^{3+}:\text{Y}_2\text{SiO}_5$ and explores optimization strategies for better performance in SHB applications. Use of broadband absorption and site-selective fluorescence spectroscopy allowed mapping the relevant energy levels for operation at $1.5\mu\text{m}$ as well as measuring the fluorescence lifetime of the excited state. Paramagnetic g

values of the ground and excited states were characterized as a function of magnetic field orientation with Zeeman spectroscopy. The g value is one of the key variables in controlling the Er^{3+} spin dynamics of the material, which leads to a linewidth broadening referred to as spectral diffusion. Stimulated photon echo spectroscopy was used to characterize spectral diffusion as a function of magnetic field, temperature, and erbium ion concentration. Experimental results were successfully described by established theories and advanced our fundamental understanding of these materials. [48] Conventional and nonlinear spectroscopic methods, when utilized together, enabled material optimization for SHB applications and the measurement of the narrowest optical resonance in any solid-state material.

Additional information is summarized in the appendices. A complete description of the electronic feedback system is included in appendix A. Appendix B describes the reference cavity. Appendix C presents a detailed derivation of Bai-Fayer theory relevant to describe spectral diffusion in $\text{Er}^{3+}:\text{Y}_2\text{SiO}_5$.

REFERENCES

1. T. Böttger, G. J. Pryde, N. M. Strickland, P. B. Sellin, and R. L. Cone, *Optics-&-Photonics-News* **12**, no.12; Dec. 2001; p.23.
2. R. L. Cone, T. Böttger, G. J. Pryde, N. M. Strickland, Y. Sun, P. B. Sellin, and R. L. Carlsten, *Semiconductor lasers stabilized to spectral holes in rare earth crystals*, *Proceeding of SPIE* **4283**, 335 (2001).
3. P. B. Sellin, N. M. Strickland, T. Böttger, J. L. Carlsten, and R. L. Cone, *Phys. Rev. B* **63** 155111 (2001).
4. G. J. Pryde, T. Böttger, R. L. Cone, and R. C. C. Ward, *Semiconductor Lasers Stabilized to Spectral Holes in Rare Earth Crystals to a Part in 10^{13} and their Application to Devices and Spectroscopy*, *J. of. Luminescence*, to appear (2002).
5. G. J. Pryde, T. Böttger, and R. L. Cone, *J. Lumin.* **94-95**, 76 (2001)
6. T. Böttger, G. J. Pryde, R. L. Cone, and G. D. Jones, *Programmable sub-kHz laser frequency stabilization at 1523 nm using persistent spectral hole burning*, submitted to *Opt. Lett.* 2002.
7. P. B. Sellin, N. M. Strickland, J. L. Carlsten, and R. L. Cone, *Opt. Lett.* **24**, 1038 (1999).
8. N. M. Strickland, P. B. Sellin, Y. Sun, J. L. Carlsten, and R. L. Cone, *Phys. Rev. B* **62**, 1473 (2000).
9. K. D. Merkel, R. W. Peters, P. B. Sellin, K. S. Repasky, and W. R. Babbitt, *Opt. Lett.* **25**, 1627 (2000).

10. Z. Cole, T. Böttger, R. Krishna Mohan, R. Reibel, W. R. Babbitt, R. L. Cone and K. D. Merkel to be published. Accepted for presentation at Conference of Lasers and Electro Optics (CLEO), Long Beach, CA, May 2002.
11. R. M. Macfarlane, T. L. Harris, Y. Sun, R. L. Cone, and R. W. Equall, *Opt. Lett.* **22**, 871 (1997).
12. T. L. Harris, Y. Sun, R. L. Cone, R. M. Macfarlane, and R. W. Equall, *Opt. Lett.* **23**, 636 (1998).
13. T. L. Harris, Y. Sun, W. R. Babbitt, R. L. Cone, J. A. Ritcey, and R. W. Equall, *Opt. Lett.* **25**, 85 (2000)
14. L. Menager, I. Lorgere, J. L. Le-Gouet, D. Dolfi, and J. P. Huignard, *Opt. Lett.* **26**, 1245 (2001).
15. N. Ohlsson, R. Krishna Mohan, and Stefan Kröll, *Opt. Comm.* **201**, 71 (2002).
16. T. Böttger, Y. Sun, G.J. Pryde, G. Reinemer, and R.L. Cone *J. Lumin.* **94-95**, 55 (2001).
17. A. Abramovici, W. E. Althouse, R. W. P. Drever, Y. Gürsel, S. Kawamura, F. J. Raub, D. Shoemaker, L. Sievers, R. E. Spero, K. S. Thorne, R. E. Vogt, R. Weiss, S. E. Whitcomb, and M. E. Zucker, *Science* **256**, 325 (1992).
18. R. G. DeVoe and R. G. Brewer, *Phys. Rev. Lett.* **50**, 1269 (1983); R. M. Macfarlane and R. M. Shelby in *Spectroscopy of Crystals Containing Rare-Earth Ions*, edited by A. A. Kaplyanskii and R. M. Macfarlane (North-Holland, Amsterdam, 1987); M. J. Sellars, R. S. Meltzer, P. T. H. Fisk, and N. B. Manson, *J. Opt. Soc. Am. B* **11**, 1468 (1994).

19. S. L. Gilbert, W. C. Swann, and T. Dennis in *Laser Frequency Stabilization, Standards, Measurement and Applications*, Proc. SPIE 4269, 184 (2001) and references therein.
20. T. W. Mossberg, *Opt. Lett.* **7**, 77 (1982); A. Rebane, R. Kaarli, P. Saari, A. Anijalg, and K. Timpmann, *Opt. Commun.* **47**, 173 (1983); M. Mitsunaga, R. Yano, and N. Uesugi, *Opt. Lett.* **16**, 1890 (1991); M. Mitsunaga, N. Uesugi, H. Sasaki, and K. Karaki, *Opt. Lett.* **19**, 752 (1994); H. Lin, T. Wang, and T. W. Mossberg, *Opt. Lett.* **20**, 1658 (1995).
21. N. W. Carlson, L. J. Rothberg, A. G. Yodh, W. R. Babbitt, and T. W. Mossberg, *Opt. Lett.* **8**, 483 (1983); M. Zhu, W. R. Babbitt, and C. M. Jefferson, *Opt. Lett.* **20**, 2514 (1995); K. D. Merkel and W. R. Babbitt, *Opt. Lett.* **24**, 172 (1999).
22. T. R. Dyke, M. J. Sellars, G. J. Pryde, N. B. Manson, U. Elman, and S. Kröll, *J. Opt. Sci. Am. B* **16**, 805 (1999); G. J. Pryde, M. J. Sellars, and N. B. Manson, *Phys. Rev. Lett.* **84**, 1152 (2000); M. J. Sellars, G. J. Pryde, N. B. Manson, and E. R. Krausz, *J. of Luminescence* **87**, 833 (2000).
- [23]. X. A. Shen and R. Kachru, *Opt. Lett.* **20**, 2508 (1995); T. Wang, H. Lin, and T. W. Mossberg, *Opt. Lett.* **20**, 2541 (1995).
24. D. J. Berkeland, J. D. Miller, J. C. Bergquist, W. M. Itano, and D. J. Wineland, *Phys. Rev. Lett.* **80**, 2089 (1998).
25. R. J. Rafac, B. C. Young, J. A. Beall, W. M. Itano, D. J. Wineland, and J. C. Bergquist, *Phys. Rev. Lett.* **85**, 2462 (2000).
26. M. Roberts, P. Taylor, G. P. Barwood, P. Gill, H.A. Klein, and W. R. C. Rowley, *Phys. Rev. Lett.* **78**, 1876 (1997).
27. J. E. Bernard, A. A. Madej, L. Marmet, B. G. Whitford, K. M. Siemsen, and S. Cundy, *Phys. Rev. Lett.* **82**, 3228 (1999).

28. E. Peik, G. Hollemann, and H. Walther, *Phys. Rev. A* **49**, 402 (1994).
29. H. Schnatz, B. Lippart, J. Helmcke, F. Riehle, and G. Zinner; *Phys. Rev. Lett.* **76**, 18 (1996).
30. C. W. Oates, E. A. Curtis, and L. Hollberg, *Opt. Lett.* **25**, 1603 (2000).
31. S. A. Diddams, D. J. Jones, J. Ye, S. T. Cundiff, J. Hall, J. K. Ranka, R. S. Windeler, R. Holzwarth, T. Udem, and T. W. Hänsch, *Phys. Rev. Lett.* **84**, 5102 (2000).
32. D. J. Jones, S. A. Diddams, J. K. Ranka, A. Stentz, R. S. Windeler, J. L. Hall, and S. T. Cundiff, *Science* **288**, 635 (2000).
33. S. A. Diddams, D. J. Jones, L.-S. Ma, S. T. Cundiff, and J. Hall, *Opt. Lett.* **25**, 186 (2000).
34. J. Reichert, M. Niering, R. Holzwarth, M. Weitz, T. Udem, and T. W. Hänsch, *Phys. Rev. Lett.* **84**, 3232 (2000).
35. J. L. Hall and Jun Ye, *Optics & Photonics News* **44**, February 2001.
36. J. L. Hall, *IEEE Journal on Selected Topics in Quantum Electronics* **6**, 1136 (2000).
37. Jun Ye, private communication.
38. R.W. Drever, J. L. Hall, F. V. Kowalski, J. Hough, G. M. Ford, A. J. Munley, and H. Ward, *Appl. Phys. B* **31**, 97 (1983).
39. D. Hils and J. L. Hall in *Proceedings of the 4th Symposium of Frequency Standards and Metrology*, Ed. A De Marchi, Springer Verlag Berlin 1989;

- C. Salomon, D. Hils, and J. L. Hall, *J. Opt. Soc. Am. B* **5**, 1576 (1988).
40. ULE, ultra low expansion glass, trademark of Corning Glass Works, Corning, NY 14831.
41. Zerodur is a trademark of Schott Glaswerk, Mainz, Germany.
42. S. Seel, R. Storz, G. Ruoso, J. Mlynek, and S. Schiller, *Phys. Rev. Lett.* **78**, 4741 (1997).
43. B.C. Young, F.C. Cruz, W.M. Itano, and J.C. Bergquist, *Phys. Rev. Lett.* **82**, 3799 (1999).
44. R. W. Equall, Y. Sun, R. L. Cone, and R. M. Macfarlane, *Phys. Rev. Lett.* **72**, 2179 (1994).
45. T. W. Mossberg, *Opt. Lett.* **7**, 77 (1982).
46. Y. S. Bai, W. R. Babbitt, N. W. Carlson, and T. W. Mossberg, *Appl. Phys. Lett.* **45**, 714 (1984).
47. W. R. Babbitt, *Advanced Optical Memories and Interfaces to Computer Storage Proc. SPIE* **3468**, 304 (1998).
48. Y. S. Bai and M. D. Fayer, *Phys. Rev. B* **39**, 11066 (1989).

CHAPTER 2

MATERIALS-BACKGROUND AND THEORY

The rare earth ions, or lanthanides, form a special group of elements in the periodic table. Triply-ionized rare earth ions have a partially filled 4f shell, shielded from the environment by the outer lying filled 5s² and 5p⁶ electron shells. These partially filled shells give rise to narrow spectral lines due to inner shell 4f-4f transitions that span the spectrum from the far infrared to the vacuum ultraviolet. [1] Even when doped into a crystal host material, the shielding of the 4f levels is so efficient, that the "crystal field" acts only as a weak perturbation to the free ion levels. The levels obtained from observed spectra closely resemble those of free ions.

Here the discussion is restricted to the Er³⁺ doped materials that were investigated in this research. The Er³⁺ energy levels arise from the odd-numbered 4f¹¹ electron configuration. For the free ion, the angular momenta J and M_J are good quantum numbers, and the energy levels are $2J+1$ fold degenerate and give rise to multiplets that are labeled by J . When the ion is incorporated into the crystal, the reduced crystal field symmetry causes partial lifting of the $2J+1$ fold M_J degeneracy. For ions with an odd number of electrons, Kramers theorem [2] dictates that all levels have electronic degeneracy that can only be lifted by a magnetic field. Because of Kramers degeneracy, the crystal field can lift the degeneracy only to a

maximum of $J+1/2$ crystal field levels depending on the ions' site symmetry. As a result, the ${}^4I_{15/2}$ ground multiplet can be split into 8 Kramers doublets, the ${}^4I_{13/2}$ multiplet into 7. For the laser spectroscopy experiments, a simple two level system model is used, where the lowest crystal field-split levels of the ${}^4I_{15/2}$ and ${}^4I_{13/2}$ serve respectively as the ground and excited state. Applying an external magnetic field lifts the remaining Kramers degeneracy. This electronic degeneracy and the associated electronic magnetic moments lead to strong Zeeman interactions.

Transitions between the ${}^4I_{15/2} \rightarrow {}^4I_{13/2}$ multiplets in Er^{3+} doped compounds are in the $1.5 \mu\text{m}$ spectral region, where optical fiber transmission losses are a minimum. This situation makes Er^{3+} materials attractive for technological applications and explains why so much effort in recent years went into developing Erbium materials for all-optical signal processing applications based on spectral hole burning. [3, 4, 5]. Conversely, the well developed infrastructure for $1.5 \mu\text{m}$ telecommunication devices including diode lasers, with Er-doped fiber amplifiers, high bandwidth detectors and modulators, fiber beamsplitters etc., can be exploited for spectroscopy and demonstrations of SHB devices. This interest continued in this work by exploiting, optimizing and demonstrating the potential of $\text{Er}^{3+}\text{Y}_2\text{SiO}_5$ for applications in laser frequency stabilization and high bandwidth all-optical correlation.

Homogeneous and Inhomogeneous Broadening

In rare earth doped materials, two major broadening mechanisms influence the observed optical spectra - homogeneous broadening and inhomogeneous broadening. Homogeneous broadening is experienced equally by individual ions in the crystal and is governed by dynamical processes acting as perturbations on the ion's transition frequency or phase. For Er^{3+} doped compounds, the homogeneous linewidth can be expressed as the sum of several contributions

$$\Gamma_{\text{hom}} = \Gamma_{\text{pop}} + \Gamma_{\text{Er-Er}} + \Gamma_{\text{Phonon}} + \Gamma_{\text{Er-Host}} + \Gamma_{\text{ISD}}. \quad (2.1)$$

The contribution Γ_{pop} corresponds to the fundamental linewidth associated with the excited state population lifetime, T_1 ; Γ_{pop} relates to the population lifetime, T_1 , as

$$\Gamma_{\text{pop}} = \frac{1}{2\pi T_1}. \quad (2.2)$$

The T_1 lifetimes can be extremely long for these rare earth ion levels and have been measured in excess of 10 ms for the lowest ${}^4\text{I}_{13/2}$ level. Other erbium ions undergo phonon-induced electronic spin flip transitions in their ground state and therefore modulate the energy levels of the optical transition causing the contribution, $\Gamma_{\text{Er-Er}}$. The $\Gamma_{\text{Er-Er}}$ contributions have been measured, modeled, and optimized in this work by choosing a proper Er^{3+} -ion concentration, operating temperature, and magnetic field strength and direction. The Γ_{Phonon} contribution includes dephasing from temperature-dependent phonon scattering. Working at cryogenic temperatures minimizes higher order phonon contributions. Only direct phonon processes are

important. Nuclear and electronic spins of the host lattice contribute $\Gamma_{Er-Host}$. Using a host such as Y_2SiO_5 that exhibits low or zero nuclear magnetic moment or low isotopic abundance of magnetic nuclei, can control these contributions. Changes in the local environment due to the optical excitation of neighboring ions, an effect termed instantaneous spectral diffusion (ISD), contributes Γ_{ISD} and can be minimized by using low optical excitation densities or low ion concentrations. Under optimal experimental conditions, the homogeneous linewidth can be ultra-narrow (< 1 kHz). The values measured in this work approach the fundamental lifetime limit. In fact, this thesis reports the narrowest optical transition, 73 Hz, observed in any solid-state material.

Due to local strains in the crystal caused by crystal growth, impurities, or lattice imperfections and dislocations, each individual optical center experiences a very slightly different local environment in the host crystal. These strains and imperfections cause the center of the homogeneous linewidth of individual optical centers to subtly shift in frequency space, leading to a distribution of transition frequencies. The combination of many homogeneously broadened lines, each with a Lorentzian absorption profile centered at its own resonant frequency, results in a much broader, often Gaussian, frequency distribution with a width called the inhomogeneous linewidth, Γ_{inh} .

Depending on rare earth dopant concentration and crystal composition, the inhomogeneous linewidth can be as much as 10^8 times broader than the individual homogeneous linewidth in some material systems [3-8,11], and may be even

broader in rare earth doped glasses. As the crystal composition is changed, the absorption frequency may be “tuned” over a considerable range. Figure 2.1 shows inhomogeneous and homogeneous broadening; each homogeneous line or “packet” represents a subgroup of ions experiencing the same local environment in the crystal. The erbium materials investigated in this work have inhomogeneous linewidths between 150 MHz and 10 GHz.

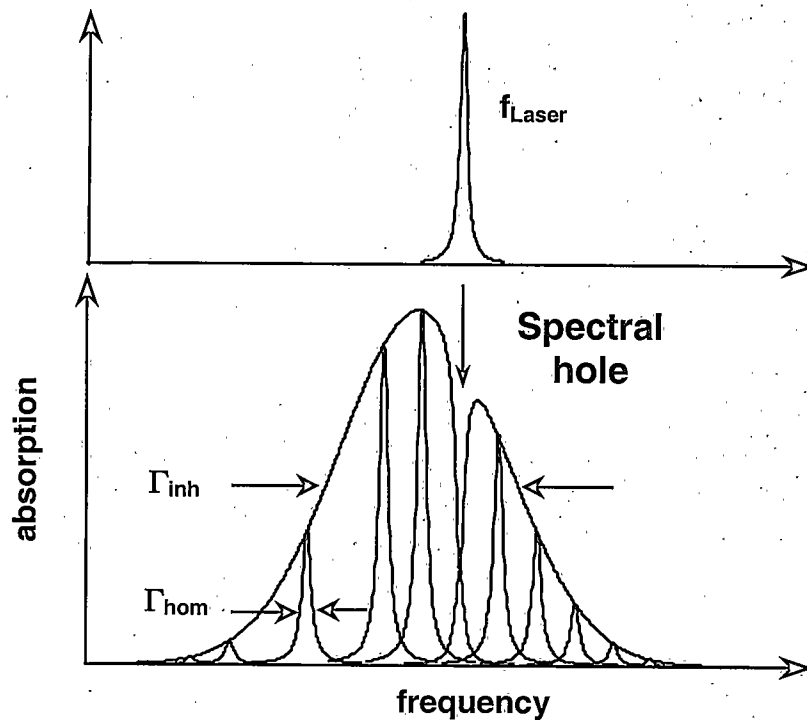


Figure 2.1 Line broadening and spectral hole burning. Each homogeneous line corresponds to a subgroup of ions experiencing the same local strain environment in the crystal. The envelope over all homogeneous linewidths defines the inhomogeneous line. A narrowband laser is used to selectively excite a subgroup of ions underneath the inhomogeneous profile from the ground to the excited state at the laser frequency f_{Laser} . A spectral hole is created at the laser frequency f_{Laser} and can be seen as a reduction in absorption.

Spectral Hole Burning

Homogeneous and inhomogeneous broadening leads to a phenomenon called spectral hole burning (SHB). In order to burn a spectral hole into the inhomogeneously broadened transition, a narrowband laser selectively excites a subset or packet of ions underneath the inhomogeneous profile, as shown in Fig. 2.1. Ions resonant with the laser are pumped from the ground state to the excited state, thereby bleaching the absorption and leaving behind a spectral hole, which can be seen as a reduction of optical material absorption at the laser frequency. This process of saturating a particular homogeneous packet in a material is one mechanism for spectral hole burning. The hole lifetime is determined by the lifetime of the population reservoir when SHB proceeds by this mechanism. In the case of Er^{3+} materials such as $\text{Er}^{3+}:\text{Y}_2\text{SiO}_5$, $\text{Er}^{3+}:\text{KTP}$ or $\text{Er}^{3+}:\text{Y}_2\text{O}_3$, hole burning does take place by population storage in the excited state of the two-level system, with the hole lifetime determined by the lifetime of the excited state, the lowest level of the $^4\text{I}_{13/2}$ multiplet. Since $^4\text{I}_{13/2}$ lifetimes for the above materials are nominally 10 ms, ions relax back into the ground state where the laser may excite them again. Under continuous laser illumination, this process takes place until a balance between spontaneous hole relaxation and hole burning occurs. Hole burning, where the hole lifetime is limited by T_1 of the excited state or an intermediate bottleneck state [6], is called transient spectral hole burning.

When the hole lifetime surpasses T_1 and extends over much larger timescales, such SHB is called persistent. Longer spectral hole lifetimes have been measured at 1.5 μm in $\text{Er}^{3+}:\text{D}^-:\text{CaF}_2$, where a different photo-physical hole burning mechanism changes the local environment of the optical center. This spectral hole burning mechanism involves photo-induced D^- ion migration into nearby interstitial sites. Spectral holes in $\text{Er}^{3+}:\text{D}^-:\text{CaF}_2$ with a full width at half maximum (FWHM) of ~ 40 MHz have been measured to be persistent without change for at least forty-eight hours. [7] Based on temperature-dependent studies of this material, it is reasonable to expect the persistence to be much greater.

In SHB materials covering the 1.5 μm wavelength region explored to date, transient holes, such as those found in $\text{Er}^{3+}:\text{Y}_2\text{SiO}_5$ and $\text{Er}^{3+}:\text{KTP}$, have proven to be orders of magnitude narrower in frequency than persistent holes, such as those in $\text{Er}^{3+}:\text{D}^-:\text{CaF}_2$, which is the only material known to date exhibiting persistent spectral hole burning at 1.5 μm .

As mentioned previously, the ratio of inhomogeneous linewidth to homogeneous linewidth can be extremely large. This becomes important, for example, in the context of frequency domain optical memory. Binary information can be stored using spectral holes, such as those found in $\text{Eu}^{3+}:\text{Y}_2\text{SiO}_5$ [8] that are being used in the development of massive optical memories at Montana State University.

Photon Echoes

In 1981 T. Mossberg discussed the possibility of storing data as a temporal stream in the time domain. [9] This method of data storage is equivalent to burning the Fourier transform of the data stream into the inhomogeneous line. Coherent phenomena in the time domain, called optical coherent transients, include photon echoes of various types, optical nutation, and free induction decay. Optical coherent transients can overcome the resolution limit imposed by inhomogeneous broadening [11]. A large body of literature on coherent transients exists and the reader is referred to Ref. [10, 11, 12] and to references therein for a detailed theoretical treatment. A brief summary relevant to the work presented in this thesis will be given.

Photon echoes are the optical analogue of spin echoes, long known in nuclear magnetic resonance (NMR) [13], and were first observed by Kurnit *et al.* [14] and Abella *et al.* [15] in ruby. The photon echo technique uses a sequence of short pulses to indirectly measure the homogeneous linewidth without significant spectral selection by the laser. The spectral width of the pulses may be large compared to the homogeneous linewidth, thus relaxing the need for an ultra-stable laser source. The effect of inhomogeneous broadening is removed by the pulse sequence itself.

Two Pulse Photon Echo

In a two-pulse photon echo experiment, two laser pulses, separated by a time delay, τ , excite the sample, as shown in Fig. 2.2. The first pulse creates a coherent superposition of the ground and excited states. After the first pulse, this coherent superposition state has a macroscopic oscillating dipole moment, whose re-radiation is the free induction decay. [16] As time elapses, this dipole moment quickly dephases as the ions accumulate phase according to their frequency offset from the laser frequency within the inhomogeneous distribution. The second pulse, at time, τ , acts to exchange the amplitudes of ground and excited state in the coherent superposition, which leads to a phase reversal for each individual ion; the ions begin to rephase. After a waiting period, τ , following the second pulse, the net phase shift cancels for each ion, leading to a rephasing of the coherence in the form of a macroscopic oscillating dipole, detected as the photon echo. To optimize the strength of the photon echo signal, the first pulse should be a $\pi/2$ pulse to excite the sample to a coherent superposition state with equal amplitudes, meaning it should be of area

$$\Theta = \int (\mu_{12} E(t) / \hbar) dt = \frac{\pi}{2} \quad (2.3)$$

with the transition dipole moment, μ_{12} , and the electric field strength, E , of the pulse. The second pulse should be a π -pulse to exactly interchange amplitudes and phase factors for the ground and excited states.

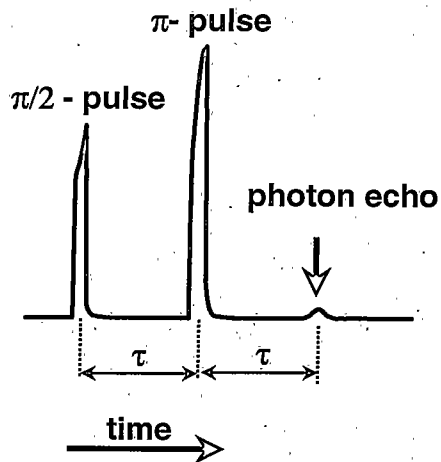


Figure 2.2 A typical two-pulse photon echo sequence. The first excitation pulse is chosen to be of area $\pi/2$ and the second pulse of area π follows pulse 1 after a time delay of τ ; note the optical absorption of the pulses. The two pulse photon echo occurs after a time delay τ after the π -pulse. This figure shows an experimental trace; the shape and heights of the transmitted excitation pulses are modified by coherent absorption by the sample.

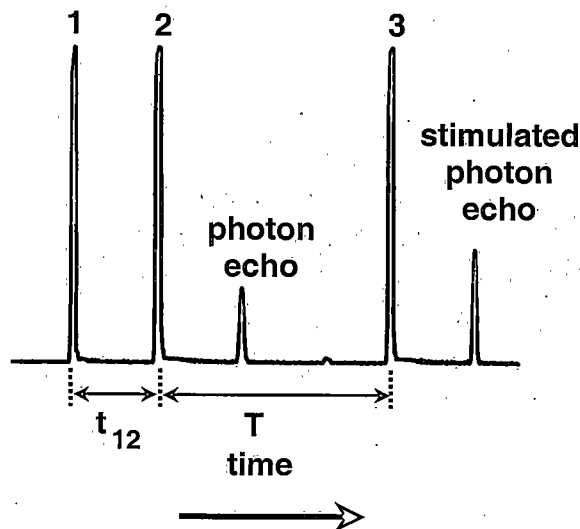


Figure 2.3 A typical stimulated photon echo pulse sequence. The first two excitation pulses are separated by a time delay t_{12} and pulse 2 and 3 are separated by the waiting time T . The stimulated photon echo occurs after a time delay t_{12} after pulse 3, a two pulse echo can be observed after a time delay t_{12} after pulse 2; note that the excitation pulse area is $\sim \pi/2$ for all 3 pulses causing the stimulated photon echo to be stronger than the two pulse photon echo.

As τ is increased, a reduction in intensity of the echo reflects the decay of coherence during the time, 2τ , as the result of stochastic processes in the crystal. Measuring the photon echo intensity, as a function of the time delay, τ , between the two pulses, yields for ideal two-level systems a single exponential decay as $\exp(-4\tau/T_2)$ whose time constant allows determining the dephasing time, T_2 . The homogeneous linewidth can be determined from the dephasing time T_2 by

$$\Gamma_{\text{hom}} = \frac{1}{\pi T_2} \quad (2.4)$$

and provides a method to measure very narrow, sub-kilohertz linewidths with a laser, whose linewidth can be several 100 kHz. In some material systems [8] the observed decays depend on the power of the pulses used due to instantaneous spectral diffusion (ISD). The measured values of the linewidth must then be plotted as a function of pulse power and extrapolated to zero power to obtain the true value for T_2 ; for such cases, $\pi/2$ and π -pulses are not optimum. The optical Bloch equations and the optical Bloch vector model provide a visual picture of the population dynamics and the coherence of an ensemble of ions in the interaction with an excitation pulse sequence of the laser field. [10]

In the presence of spectral diffusion, where the homogenous linewidth evolves on a timescale of the pulse sequence, observed echo decays are non-exponential and can be described by the Mims [17] expression

$$I(t) = I_0 \exp\left(-\frac{4t_{12}}{T_M}\right)^x \quad (2.5)$$

first introduced in the context of electron spin echoes and later used in the analysis of photon echoes. [18] The parameter, x , describes the deviation from a pure exponential, while T_M corresponds to T_2 , in the specific case of $x = 1$. An effective homogeneous linewidth can be extracted from the phase memory time, T_M , as

$$\Gamma_{\text{hom}} = \frac{1}{\pi T_M}. \quad (2.6)$$

Stimulated Photon Echo

Stimulated photon echoes conveniently allow studying spectral diffusion. The stimulated photon echo requires a three $\pi/2$ -pulse sequence and can be thought of as a modified two-pulse echo, where the second π -pulse is broken up into two $\pi/2$ -pulses, separated by the waiting time, T . The pulse separation between pulses one and two is t_{12} . Figure 2.3 shows a typical stimulated photon echo pulse sequence. As in the two-pulse echo case, the first pulse creates a coherent superposition state. After a period, t_{12} , the phases of the superposition states evolve, according to the frequency offset from the laser frequency within the excited packets. Rather than completely reversing the phases with pulse two, the second pulse has an area of $\pi/2$ and thus stores ions that have accumulated less than π in phase in the excited state and ions that have accumulated more than π in phase in the ground state. As a result, the total phase information is stored as a population grating between ground and excited state with a frequency period given by $1/t_{12}$. This grating decays due to

population decay with the lifetime of the excited state, T_1 , and gets smeared out due to frequency shifting interactions (i.e. spectral diffusion) during the waiting time T . The grating can be probed with a short $\pi/2$ -pulse after the waiting time, T , which causes a rephasing of the stored coherence after a time delay, t_{12} , and the stimulated photon echo is emitted. The stimulated photon echo amplitude contains information about dephasing during the two t_{12} -delays and spectral diffusion and population decay during the waiting time, T . Systematic measurements of the stimulated echo decay as a function of the waiting time allow mapping out the time evolution of the homogeneous linewidth as excited ions undergo spectral diffusion. Results for $\text{Er}^{3+}:\text{Y}_2\text{SiO}_5$ are presented in chapter 5.

REFERENCES

1. S. Hufner, *Optical Spectra of Transparent Rare Earth Compounds*, Academic Press, London (1978).
2. H. A. Kramers, *Proc. Amsterdam Acad.* **33**, 959 (1930).
3. R. M. Macfarlane, T. L. Harris, Y. Sun, R. L. Cone, and R. W. Equall, *Opt. Lett.* **22**, 871 (1997).
4. T. L. Harris, PhD thesis *Erbium based Optical Coherent Transient Correlator for the 1.5 Micron Communication Bands*, Montana State University, Bozeman, April 2001.
5. Y. Sun, C. W. Thiel, R. L. Cone, R. W. Equall, and R. W. Hutcheson, *Recent Progress in Developing New Rare Earth Materials for Hole Burning and Coherent Transient Applications*, to appear in *J. Lumin.* (2002).
6. R. M. Macfarlane, *Opt. Lett.* **18**, 1958 (1993).
7. N. M. Strickland, R.L. Cone, and R.M. Macfarlane, submitted to *Phys. Rev. B*.
8. R. W. Equall, Y. Sun, R. L. Cone, and R. M. Macfarlane, *Phys. Rev. Lett.* **72**, 2179 (1994).
9. T. W. Mossberg, *Opt. Lett.* **7**, 77 (1982).
10. L. Allen and J. H. Eberly, *Optical Resonance and two level atoms*, Dover Publications Inc., New York, 1987.

11. R. M. Macfarlane and R. M. Shelby, Chapter 3 *Coherent Transient and Hole Burning Spectroscopy of Rare Earth Ions in Solids*, in *Spectroscopy of Solids containing Rare Earth Ions*, Eds. A.A. Kaplyanskii and R. M. Macfarlane, Elsevier Science Publishers North Holland, Amsterdam, 1987.
12. M. D. Levenson, *Introduction to Nonlinear Laser Spectroscopy*, Academic Press, New York 1982.
13. E. L. Hahn, *Phys. Rev.* **80**, 580 (1950).
14. N. A. Kurnit, I. D. Abella, and S. R. Hartmann, *Phys. Rev. Lett.*, **13**, 567 (1964).
15. I. D. Abella, N. A. Kurnitt, and S. R. Hartmann, *Phys. Rev.* **141**, 391 (1966).
16. A. Z. Genack, R. M. Macfarlane, and R. G. Brewer, *Phys. Rev. Lett.* **37**, 1078 (1976).
17. W. B. Mims, *Phys. Rev.* **168**, 370 (1968).
18. R. M. Macfarlane, R. Wannemacher, D. Boye, Y. P. Wang, and R. S. Meltzer, *J. of Lumin.* **48-49**, 313 (1991).

CHAPTER 3

LASER FREQUENCY STABILIZATION-BACKGROUND AND THEORY

Frequency Modulation Spectroscopy

The laser frequency stabilization technique reported uses ultra-narrow spectral holes as a laser frequency reference. To detect the center of the spectral hole, frequency modulation (FM) spectroscopy provided a very sensitive method. FM-spectroscopy was described and refined about 20 years ago by Bjorklund [1, 2,] as a means to sensitively detect weak absorption features, such as spectral holes, and independently by Hall [3, 4] in the context of servo locking a tunable laser to a high finesse cavity [5]. Both techniques are closely related optical analogs of methods developed in the microwave region by Pound in the 1940's. [6] The following section presents the basics of general optical FM-spectroscopy theory following references [7, 8, 9]. The FM-lineshapes were calculated, and the error signal slope was determined as a function of modulation frequency and modulation index.

Figure 3.1 shows the basic setup for FM-spectroscopy [1]. The output of a single-mode laser of carrier frequency, ω_c , passes through an electro-optic phase modulator (EOM) driven sinusoidally by an applied electric field at the RF-modulation frequency, ω_m , with a modulation index, M . The modulation index, M , in

radian units is related to the modulation amplitude, $2\pi\delta\nu$, and modulation frequency,

$\omega_m = 2\pi f_m$, by

$$M = \frac{2\pi\delta\nu}{2\pi f_m} = \frac{\delta\nu}{f_m}. \quad (3.1)$$

The optical field after passing through the EOM is given by

$$E(t) = E_0 \exp(i\omega_c t + M \sin \omega_m t), \quad (3.2)$$

which can be written using a Bessel series expansion as

$$E(t) = E_0 \exp(i\omega_c t) \sum_{n=-\infty}^{\infty} J_n(M) \exp(in\omega_m t). \quad (3.3)$$

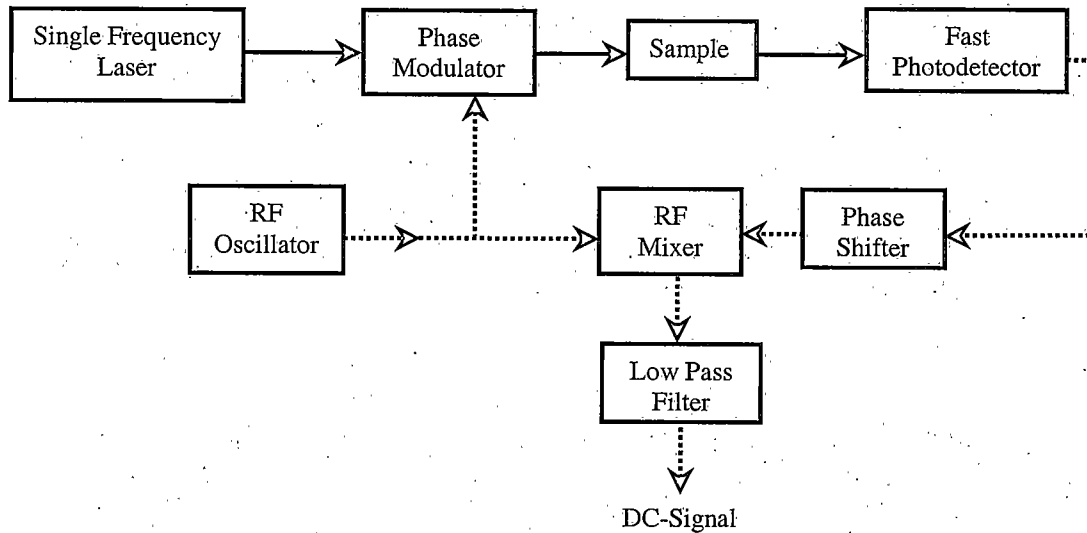


Figure 3.1 Block diagram of the experimental setup for frequency modulation (FM) spectroscopy based on phase sensitive detection. Solid lines denote optical signals, and dashed lines denote electrical signals.

The phase modulation generates frequency sidebands, spaced above and below the laser carrier frequency, ω_c , at integer multiples of the modulation frequency, ω_m , as shown in Fig. 3.2. Because $J_{-n}(M) = (-1)^n J_n(M)$, the lower frequency components with odd n are 180° out of phase with the upper sidebands, with the even-order sidebands exactly in phase. Upper and lower sidebands of the same order are matched in amplitude.

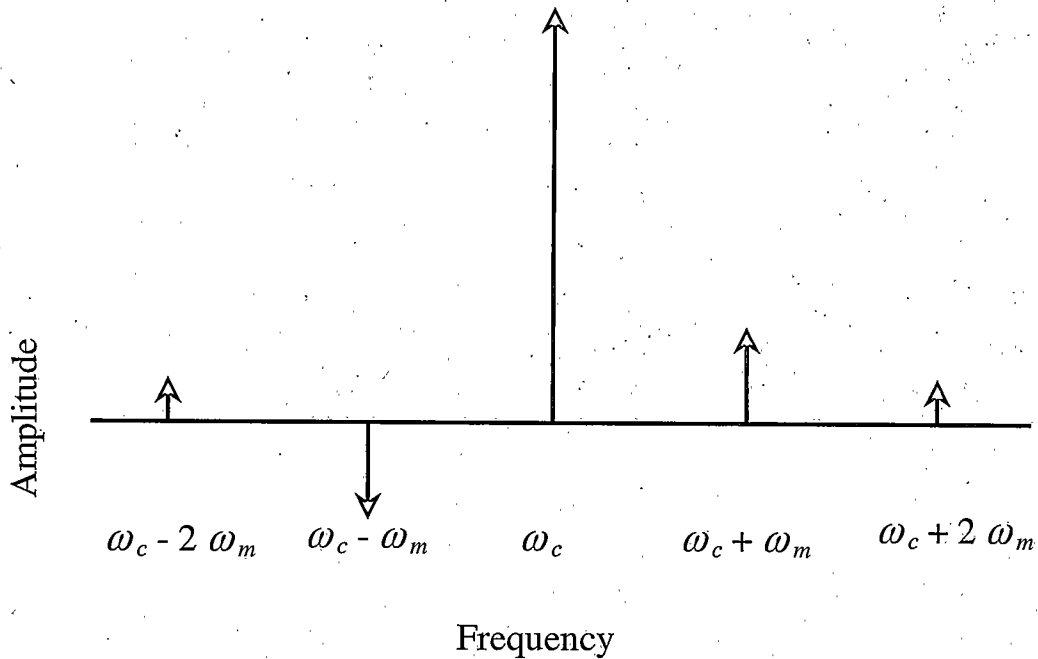


Figure 3.2 Spectrum of the electric field after passing the phase modulator. Frequency sidebands appear spaced above and below the laser carrier frequency ω_c at integer multiples of the modulation frequency ω_m . Lower frequency components with odd n are exactly 180° out of phase with the upper sidebands; and the even order sidebands must be exactly in phase. Upper and lower sidebands of the same order are matched in amplitude.

The choices of modulation index, M , and modulation frequency, ω_m , define two major regions of operation, FM-spectroscopy and wavelength modulation (WM) spectroscopy. In FM-spectroscopy, the modulation index is chosen so that the light spectrum consists of a strong carrier and only one significant pair of sidebands. The intensity, I_1 , of the sideband relative to that of the carrier, I_0 , for $M \leq 1$ is approximately given by

$$\frac{I_1}{I_0} = \left(\frac{M}{2}\right)^2. \quad (3.4)$$

The modulation frequency is best chosen large compared to the linewidth, Γ , of the spectral feature. This serves to put the resonance information at an RF frequency where laser noise is minimal and the detection becomes shot noise limited.

In the region of WM spectroscopy, a strong modulation index, M , is chosen, so that many sidebands appear, even larger in amplitude than the carrier at ω_c itself. The number of side bands contributing significantly to the sum for $M \gg 1$ is roughly approximated by

$$-M \leq n \leq M. \quad (3.5)$$

Going back to Fig. 3.1, the beam emerging from the EOM then passes through the sample of length, L , spectral half width half maximum (HWHM), Γ , intensity absorption coefficient, α , and index of refraction, n , with the latter two being functions of the optical frequency. Hence, each frequency sideband, ω_n , of the optical field will experience a different attenuation and phase shift, which can be accounted for by introducing a complex transmission function

$$T(\omega_n) = \exp(-\delta_n - i\phi_n), \quad (3.6)$$

with δ_n , being the amplitude attenuation, and ϕ_n , being the optical phase shift for frequency component, ω_n . The transmitted optical field is then

$$E_T(t) = E_0 \exp(i\omega_c t) \sum_{n=-\infty}^{\infty} T(\omega_n) J_n(M) \exp(in\omega_m t). \quad (3.7)$$

Without the presence of an absorptive feature, the FM-spectrum does not distort and a null signal can be detected arising from a perfect cancellation of the RF signal due to the upper and lower sidebands beating against the carrier. With an absorptive feature present, the perfect balance is broken and the effect of attenuation and phase shift experienced differently by each sideband leads to a disturbance of the phase modulated light, resulting in a time varying intensity. A signal at the modulation frequency, ω_m , can be recorded with a fast photodetector as indicated in Fig. 3.1. Supplee *et al.* [7] have calculated the detector signal for arbitrary modulation index, M , as

$$\begin{aligned} |E_{\omega_m}(t)|^2 = E_0^2 \exp(-2\delta_0) [& 1 + 2 \cos \omega_m t \sum_{n=0}^{\infty} J_n J_{n+1} (\delta_{-n-1} - \delta_{n+1} + \delta_{-n} - \delta_n) \\ & + 2 \sin \omega_m t \sum_{n=0}^{\infty} J_n J_{n+1} (\phi_{-n-1} - \phi_{-n} + \phi_{n+1} - \phi_n)] \end{aligned} \quad (3.8)$$

The signal consists of a DC part (constant) and two time varying components, modulated at ω_m due to a beating of adjacent frequency sidebands. Terms coming from higher order sidebands interfering with each other ($\sim 2\omega_m$, $\sim 3\omega_m$, etc.) have been omitted because the detection bandwidth is at ω_m . Use of an AC-coupled photodiode allows exclusive detection of the time-varying part of the signal. Phase

sensitive detection with a mixer and phase shifter allows isolation of both the absorptive ($\sim \cos \omega_m t$) and dispersive ($\sim \sin \omega_m t$) components. A mixer is a nonlinear device whose output is the product of its inputs. Choosing the detected optical signal as one input and the modulation signal of the local oscillator at ω_m as the other input, the mixer output will contain a signal at the sum and difference frequencies of the input signals. The difference frequency signal, which will be at DC, can be further isolated with a low pass filter. In practice, the phase shifter is important to compensate for unequal delays between signals and to detect the pure absorptive or dispersive FM-signal. Intermediate settings of the phase shifter produce mixed lineshapes and, as later described, allow implementing a hybrid locking technique to improve the long-term laser frequency stability (see section: incorporating the inhomogeneous absorption line as a fixed reference in Chapter 4).

In the case of FM-spectroscopy, the Bessel series expansion can be terminated after the first set of side bands so that expression (3.8) simplifies to [1,7,8]

$$|E(t)|^2 = E_0^2 \exp(-2\delta_0) [1 + M(\delta_{-1} - \delta_1) \cos \omega_m t + M(\phi_{-1} + \phi_1 - 2\phi_0) \sin \omega_m t]. \quad (3.9)$$

In FM-spectroscopy, ω_m is chosen large compared to Γ ($\omega_m \gg \Gamma$), so that the spectral feature can be probed by an isolated sideband where either the carrier frequency, ω_c , of the laser or alternatively the RF modulation frequency, ω_m , is scanned across the optical transition. The $\cos \omega_m t$ component then directly displays the absorption profile when the upper or lower sideband resonates with the optical

transition, whereas the $\sin\omega_m t$ component displays three dispersion curves, one for each frequency component resonant with the spectral feature as shown in Fig. 3.3.

In the case of a Lorentzian line shape, a good representation for the homogeneous linewidth given by a spectral hole, attenuation and optical phase shift can be written as

$$\delta(\omega) = A \left(\frac{\Gamma^2}{(\omega - \Omega)^2 + \Gamma^2} \right) \quad (3.10)$$

$$\phi(\omega) = A \left(\frac{(\omega - \Omega)\Gamma}{(\omega - \Omega)^2 + \Gamma^2} \right) \quad (3.11)$$

with A denoting the maximum absorption, Ω , the line center frequency and Γ , the half width at half maximum (HWHM) of the Lorentzian. From these expressions, the theoretical FM-lineshapes for absorption and dispersion signals can be computed. All the lineshapes presented have been computed using relation (3.8), (3.10) and (3.11) by taking the first 100 sidebands in the Bessel series expansion into account. The above expressions (3.10) and (3.11) have been normalized using $A = 0.1$, $\Gamma = 1$ and $\Omega = 0$. Ordinate axes were normalized in units where $c\varepsilon_0/2E_0^2 = 1$, and the abscissa ranges from -30 to $+30$ in units where the absorption peak HWHM, Γ , has been set equal to 1.

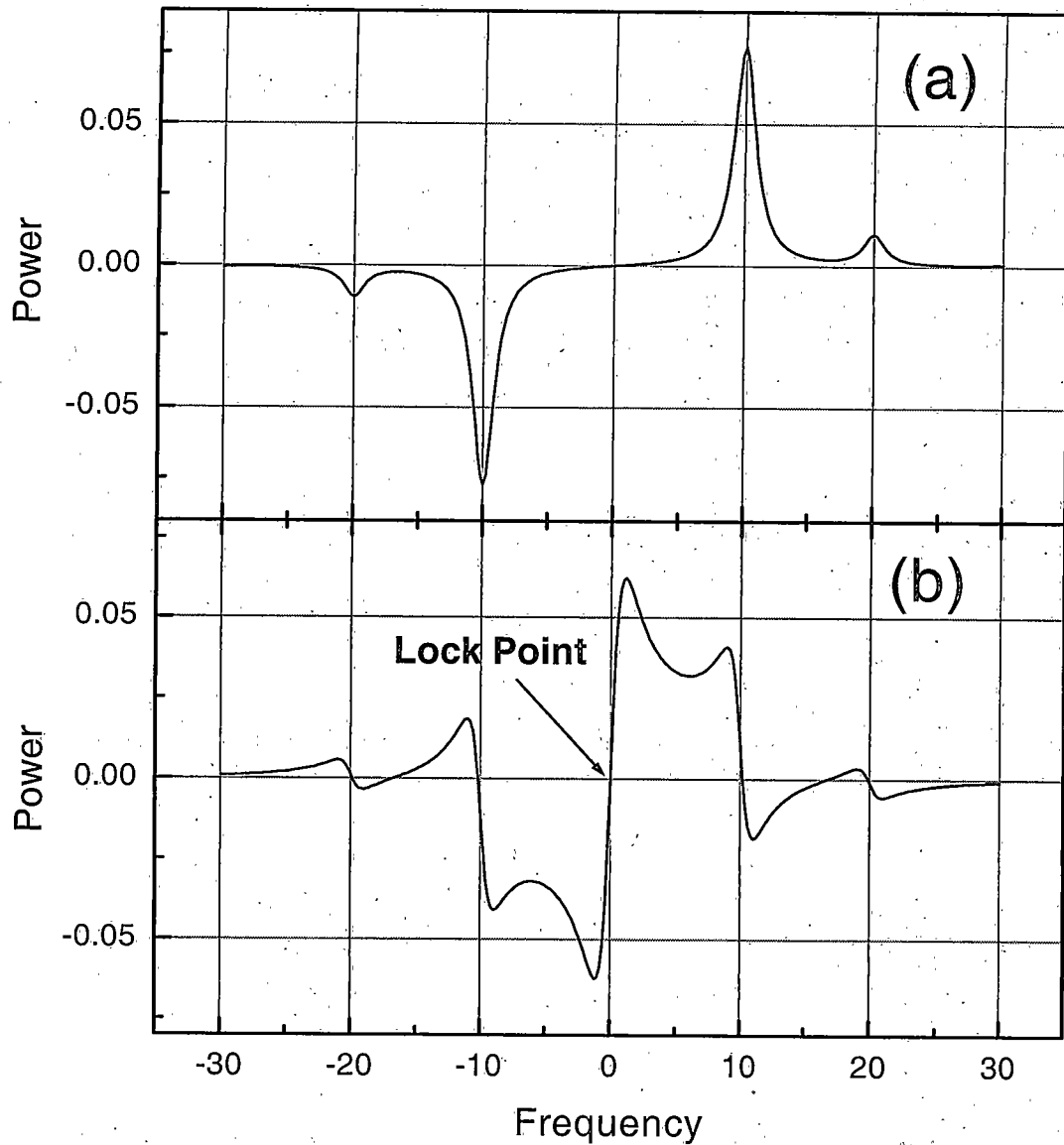


Figure 3.3 Calculated FM-signals for $\Gamma = 1$, $M = 1$, and $\omega_m = 10$. (a) FM-absorption signal ($\sim \cos \omega_m t$). (b) FM-dispersion signal ($\sim \sin \omega_m t$). The FM-dispersion signal serves as an error signal for laser frequency stabilization. The lock point is indicated at the line center zero crossing. The phase was adjusted for positive error signal slope.

Figure 3.3(a) shows an FM-absorption and Fig. 3.3(b) an FM-dispersion signal for $M = 1$ and $\omega_m = 10$. Note the spectral features due to the second order sidebands at a frequency of ± 20 . The amplitude of the FM-dispersion signal serves as an excellent error signal. The lock point, the resonance center of the spectral feature, corresponds to the zero crossing of the FM-dispersion signal. Active feedback is provided whenever a non-zero error signal is produced. If the laser drifts to the right off the line center, a positive voltage is measured. When the laser drifts to the left off the line center, a negative voltage is measured. Those voltages can be electronically translated into a correction signal, which drives the transducer element(s) of the laser. The steep slope of the error signal ensures a tight lock, so that small deviations from the lock point translate into large error signal voltages. A frequency window of $2\omega_m$ about the lock point provides the correct phase for the error signal and assures reliable relocking, even in the presence of large environmental disturbances. [5] As mentioned earlier, the modulation frequency is chosen at RF to minimize intrinsic laser and detection noise allowing a high degree of sensitivity. The AC response of the error signal derived from a regenerative spectral hole has been measured and calculated in Chapter 4.

Maximizing the Slope of the Error Signal

The error signal slope is a measure of its sensitivity to laser frequency fluctuations and should have maximum gain, K (V/Hz), for practical laser frequency

stabilization applications. Given a spectral feature like a narrow spectral hole of fixed width, Γ , serving as a frequency reference, issues to be resolved include determination of modulation frequency, ω_m , and modulation index, M , to maximize the slope of the error signal. Often experimental constraints restrict a free choice of these parameters, but one would like to know which of the two parameters would give room for further improvement.

To develop an intuition for the FM-signals as a function of modulation frequency and modulation index, a number of lineshapes have been computed, as shown in Fig. 3.4, using the normalizing procedure described above, with each subplot having the same abscissa and ordinate scales. Figure 3.4(a) shows calculated FM-absorption signals, $(\sim \cos \omega_m t)$, for a fixed modulation index $M = 1$ as a function of frequency for the modulation frequency, ω_m , range between 0.1 and 10. For $\omega_m = 2$ and higher, the sideband structure begins to emerge. The FM-absorption signal can be used as an error signal for small modulation frequencies relative to the absorption linewidth, Γ . For modulation frequencies up to $\omega_m \sim 0.67$, the FM-absorption signal provides a steeper slope than the FM-dispersion signal; a maximum slope is obtained for $\omega_m \sim 0.54$.

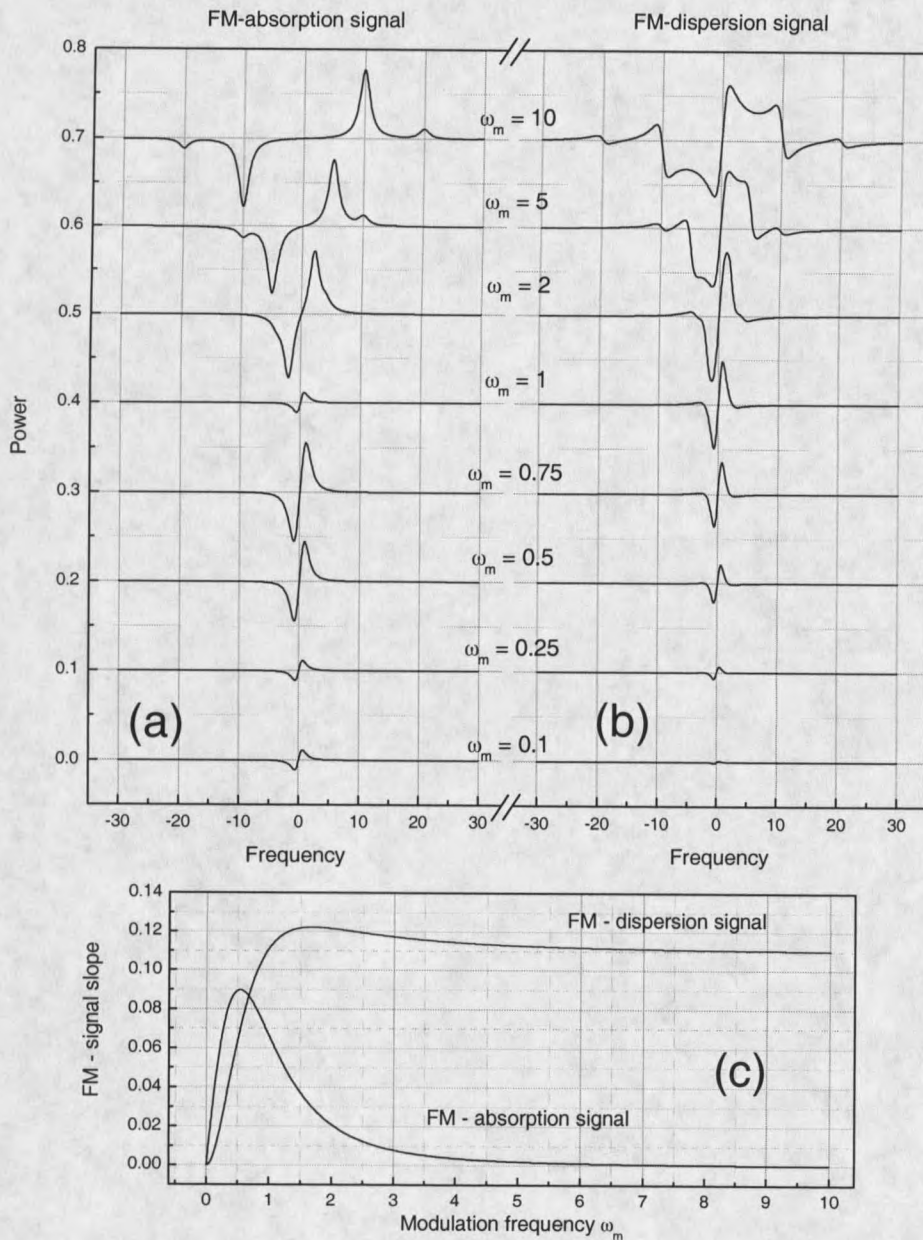


Figure 3.4 Calculated FM-signals for modulation index, $M = 1$, as a function of modulation frequency, ω_m . Each subplot has the same abscissa and ordinate scales; the frequency axes (abscissas) are given in units where the absorption peak width has been set to $\Gamma = 1$. (a) FM-absorption signal ($\sim \cos \omega_m t$). (b) FM-dispersion signal ($\sim \sin \omega_m t$). (c) Calculated FM-signal slopes for modulation index $M = 1$ at the line center zero-crossing as a function of modulation frequency.

Figure 3.4(b) shows the calculated FM-dispersion signal ($\sim \sin \omega_m t$) for comparison. At larger modulation frequencies ($\omega_m = 5$), the expected error signal emerges. To compare the FM-absorption and FM-dispersion signals for their suitability as an error signal, the FM-signal slopes for fixed modulation index $M = 1$ have been calculated at the linecenter zero crossing, as a function of modulation frequency, with results shown in Fig. 3.4(c). The FM-dispersion signal slope is maximized at $\omega_m \sim 1.69$, a larger value than the FM-absorption slope, and remains large for increasing ω_m , with the additional advantage of an increased locking window.

Figure 3.5 shows FM-signals computed for fixed modulation frequency $\omega_m = 5$, as the modulation index, M , increases from $M = 0.01$ to $M = 10$. Figure 3.5(a) shows the FM-absorption signal. Increasing M to approximately 1 causes the power in the first set of sidebands to increase. Further increase of M causes the power of the next pair of sidebands to increase, leading to a transfer of power from the inner sidebands to the outer sidebands, with the total number of significant sidebands to appear given by relation (3.5) above. The slope at linecenter goes through a maximum but does not change its sign. Figure 3.5(b) contrasts the FM-absorption signal with the FM-dispersion signal. As M increases, the sideband power transfers from the inner to the outer sidebands. The slope at linecenter steadily increases up to $M = 1$, proceeds through a maximum, and after reversal of sign reaches a second smaller peak.

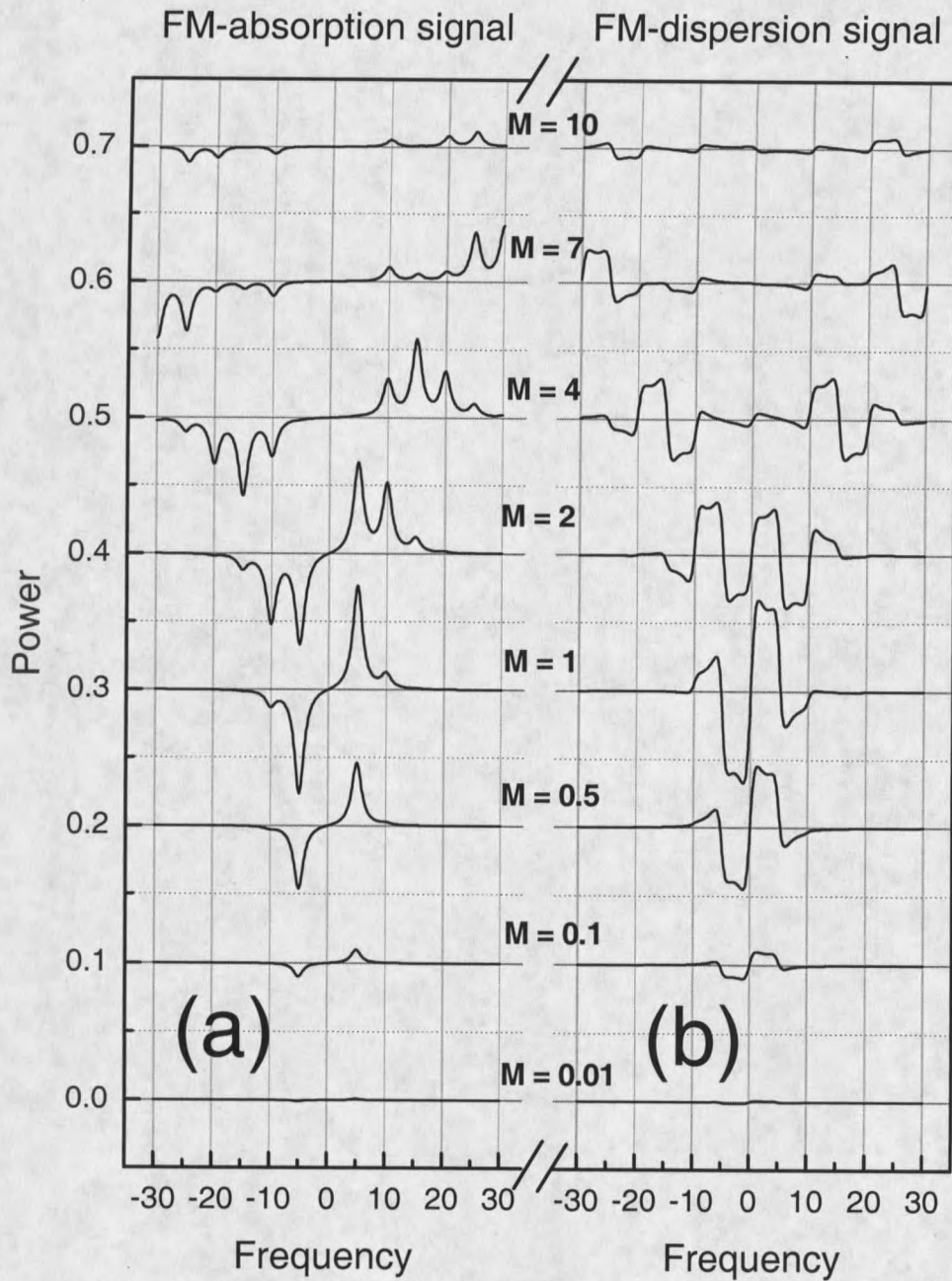


Figure 3.5 Calculated FM-signals for modulation frequency $\omega_m = 5$ as a function of frequency, the modulation index, M , varies between subplots. Each subplot has the same abscissa and ordinate scales; the frequency (abscissas) are given in units where the absorption peak width has been set equal to $\Gamma = 1$. (a) FM-absorption signal ($\sim \cos \omega_m t$). (b) FM-dispersion signal ($\sim \sin \omega_m t$).

Figures 3.6 and 3.7 quantify the error signal slope as a function of modulation frequency, ω_m , and modulation index, M , that have been varied between 0 and 10. Lines representing dotted plots show the envelope of maximum slope that can be used as a guide in choosing the right combination of M and ω_m for a given linewidth, Γ .

Figure 3.6(a) shows the slope of the FM-dispersion signal as a function of modulation frequency, while the modulation index, M , is varied for each subplot. The overall achievable FM-dispersion signal slope increases with the modulation index from $M = 0.1$ to $M = 1.08$. A further increase in M leads to a decrease in slope. The FM-dispersion signal slope is optimized at $M = 1.08$. This number is consistent with the analytical result by Day *et al.* [10] obtained for a Pound-Drever-Hall error signal in the small modulation index approximation. The observed maximum is very broad and an increase of modulation frequency beyond the optimum value of $\omega_m \sim 1.69$ does not degrade the slope.

Figure 3.6(b) shows results obtained for the FM-absorption signal. High FM-absorption signal slopes can be achieved for small modulation frequencies and high values of the modulation index (the wavelength modulation spectroscopy limit); however, the maxima in this range are rather narrow and practical implementation presents a difficult technical challenge. A decreased locking window and an increased contribution of intrinsic laser noise to the detector signal, due to the small RF modulation frequency, give added disadvantages for those cases.

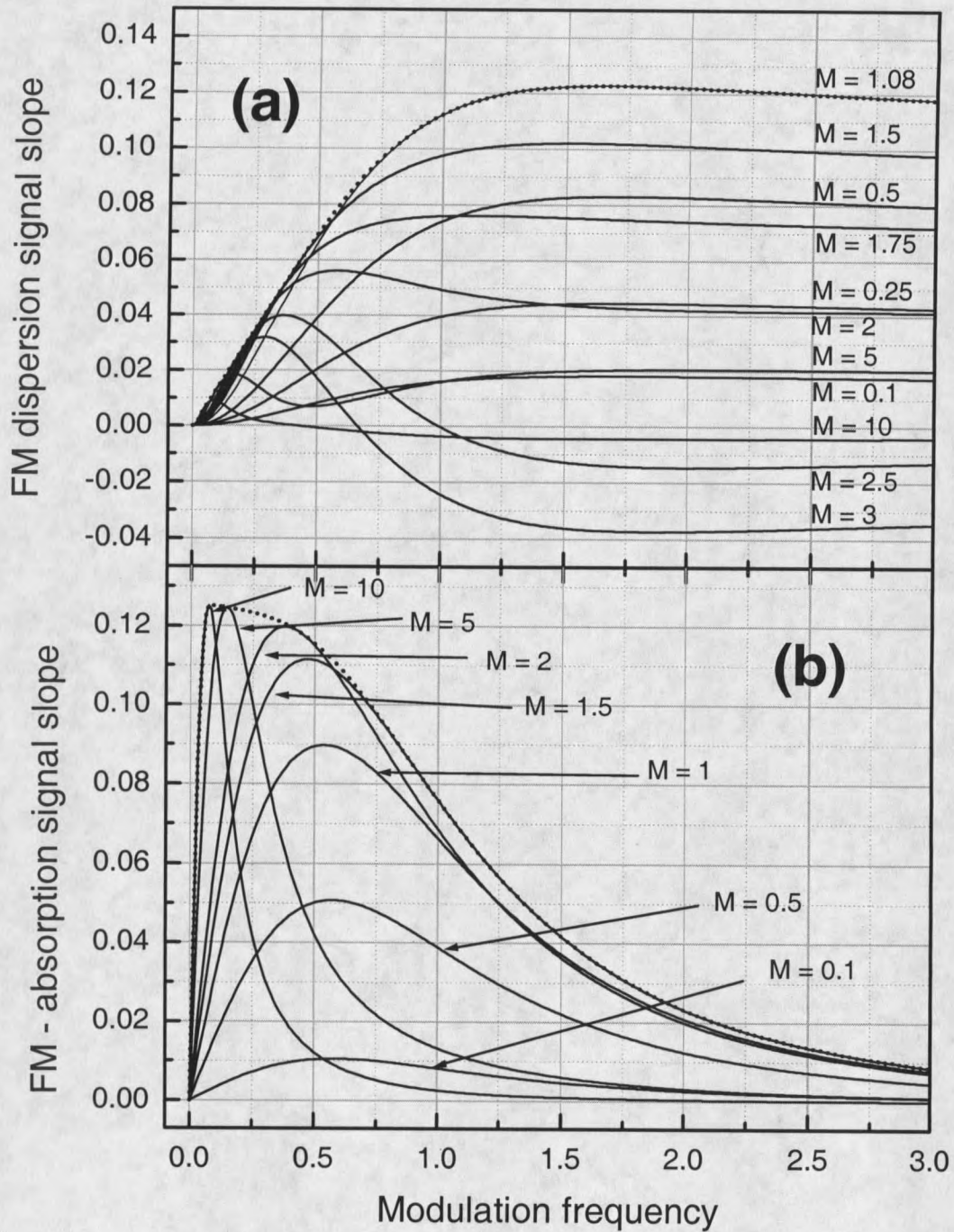


Figure 3.6 Calculated FM-signal slopes at line center as a function of modulation frequency, ω_m . The modulation index, M , has been varied between the subplots, the dotted line shows the maximum slope. (a) FM-dispersion signal slope, (b) FM-absorption signal slope.

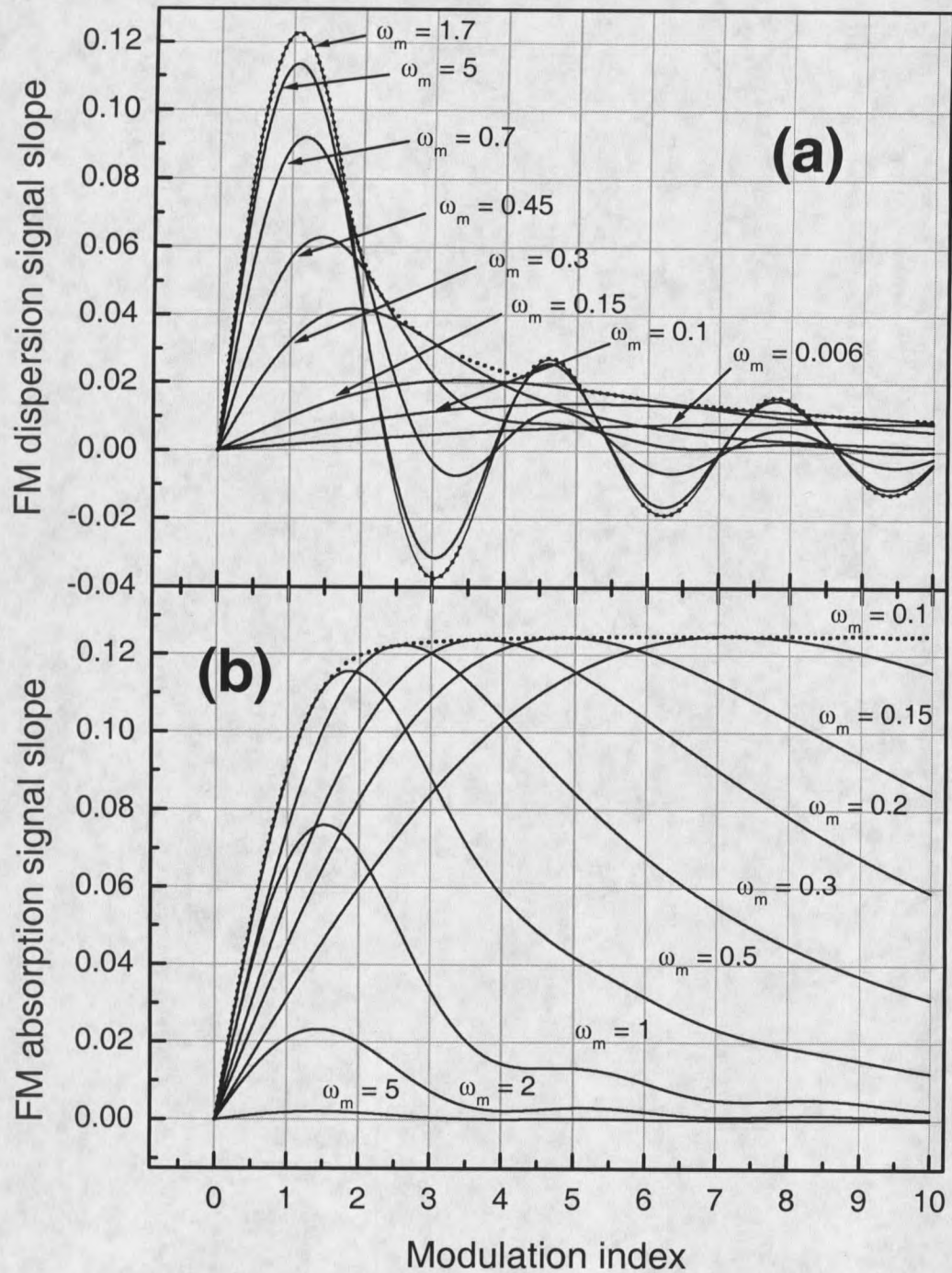


Figure 3.7 Calculated FM-signal slopes at line center as a function of modulation index, M . The modulation frequency, ω_m , has been varied between the subplots, the dotted line shows the maximum slope. (a) FM-dispersion signal slope, (b) FM-absorption signal slope.

The FM-dispersion signal is the preferred error signal to use. Figure 3.7(a) shows the FM-dispersion signal slope as a function of modulation index, as the modulation frequency varies between subplots. Maximum slope occurs for $M \sim 1.08$ and $\omega_m \sim 1.69$, as already inferred from Fig. 3.6(a). The FM-dispersion signal slope actually undergoes sign changes as inferred from Fig. 3.5(b). Figure 3.7(b) shows the corresponding FM-absorption signal slope as a function of modulation index, with the modulation frequency varying in the subplots. Optimum FM-absorption signal slope can be achieved by using a high modulation index and small modulation frequency, which has the distinct limitations described above.

In conclusion, the general theory of FM-spectroscopy has been laid out. The FM-signal lineshapes and the corresponding computed error signal slopes have been presented as a function of modulation index and modulation frequency, allowing the user to tailor and optimize the FM-signal to a specific application.

Measuring and Characterizing Laser Frequency Stability

“Of course, the real test of the achieved performance can only be accomplished with a second, independent detector system. Disappointment is the experimenters’ first reward for this measurement” J. L. Hall (1986)

This section discusses methods for measuring the frequency stability of a laser. The aim is to provide some physical insight regarding different measurement

techniques used in characterizing frequency standards; different noise types common in frequency standards, and existing relations between frequency domain and time domain quantities relevant to this work. Since time and frequency domain characterization of oscillators is a very extensive subject, only a brief overview is given and the reader is referred to references [11, 12] that describe and cite key papers in this field.

Measurement Techniques

Two basic diagnostic techniques are commonly used to characterize the frequency stability of a laser, error signal analysis (Fig. 3.8) and beat note analysis (Fig. 3.9). Error signal analysis requires only one laser beam and a suitable frequency reference such as a narrow spectral feature or a reference cavity for deducing a calibrated error signal. This method is limited in that it obtains only information about laser stability relative to the frequency reference and does not reveal noise on the discriminator itself.

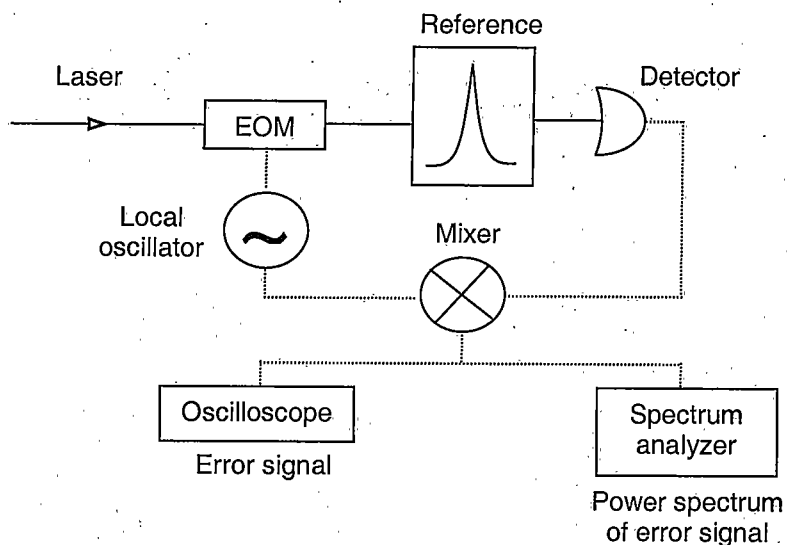


Figure 3.8 Experimental setup to characterize the frequency stability of a laser using error signal analysis.

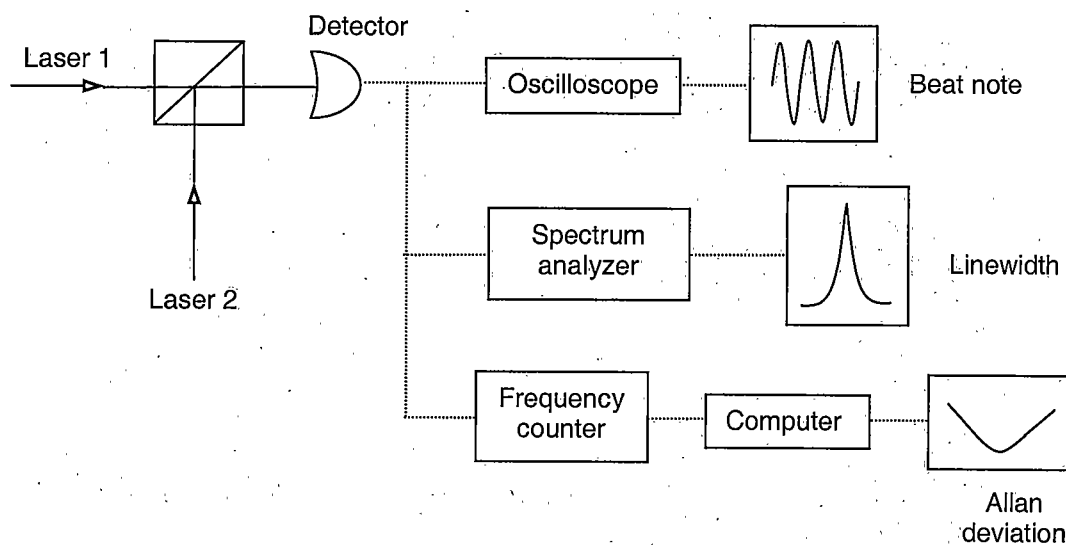


Figure 3.9 Experimental setup to characterize the frequency stability of a laser using beat note analysis.

Error signal analysis is a useful tool to gather information about gain and bandwidth of the servo loop or to measure the spectral noise density of the free running laser. In error signal analysis only the spectral noise density is readily available, other quantities, such as laser linewidth and Allan deviation, can be obtained by mathematical manipulation of the data [13], with some limitations.

The preferred method, beat note analysis (Fig. 3.9), requires two independent lasers, where the second laser serves as a local oscillator, and allows one to obtain the linewidth, spectral noise density and Allan deviation. However, obtaining information on the absolute frequency stability of the laser carries a significant economic cost incurred by the requirement of a second independently stabilized laser system. To ensure that no common mode signal is hidden, elaborate steps to decouple the two stabilized sources have to be taken [14]. In beat note analysis, unmodulated beams split off from each laser are overlapped on a fast photo detector. The measured photocurrent contains a signal that oscillates at the difference of the two optical frequencies (beat note).

Fourier transform techniques calculating the Fourier amplitude spectrum of the beat signal, as indicated by the spectrum analyzer in Fig. 3.9, help to identify noise sources, which often arise from electrical grounding (60 Hz) or shielding problems (RF-pickup) in the servo loop.

Frequency Domain-The Spectral Noise Density

The spectral noise density of frequency fluctuations, $S_\nu(f)$, characterizes frequency standards in the frequency domain. $S_\nu(f)$ describes the mean squared frequency fluctuations, $\langle \nu^2 \rangle$, occurring at some rate within a narrow bandwidth, B , around the Fourier frequency, f , giving

$$S_\nu(f) = \frac{\langle \nu^2 \rangle}{B}. \quad (3.12)$$

The spectral noise density, a measure of the power present at different frequencies, f , around the nominal carrier frequency value, is quantified with a spectrum analyzer and has the dimensions of $[\text{Hz}^2/\text{Hz}]$. A frequency discriminator translating optical or beat frequency fluctuations $[\text{Hz}]$ into amplitude fluctuations $[\text{V}]$ has to be employed to measure the spectral noise density of the frequency fluctuations of the laser. The vertical scale $[\text{dBm}]$ of the spectrum analyzer has to be calibrated using the slope, D $[\text{Hz}/\text{V}]$, of the frequency discriminator, and the measured spectrum has to be divided by the measurement bandwidth, B $[\text{Hz}]$, of the spectrum analyzer. Applying the relation

$$S_\nu(f) = \frac{\text{noise} [\text{Hz}^2]}{B} = \frac{V^2 \times D^2}{B} \quad (3.13)$$

with the conversion from power $[\text{dBm}]$ to Volts $[\text{V}]$, turns spectrum analyzer units $[\text{dBm}]$ into spectral noise density units $[\text{Hz}^2/\text{Hz}]$. The DC spike of the power spectrum on the analyzer is an artifact of the spectrum analyzer. The root-mean-

square (rms) variation of the laser frequency may be calculated from the spectral noise density using

$$\nu_{rms}^2 = \int_0^{\infty} S_{\nu}(f) df. \quad (3.14)$$

In situations with a bandwidth specific to the problem, the upper and lower bounds on the integral have to be adjusted accordingly. The equation

$$S_{\nu}(f) = (2\pi f)^2 S_{\phi}(f) \quad (3.15)$$

relates the spectral noise density of frequency fluctuations, S_{ν} , to the spectral noise density of the phase fluctuations, S_{ϕ} . In the literature, spectral noise density is often quoted as the rms spectral noise density, $\sqrt{S_{\nu}(f)}$, measured in units Hz/\sqrt{Hz} . In addition, the normalized spectral density, $S_{\nu}(f)/\nu_0^2$, and phase spectral density, $S_{\phi}(f)$, are occasionally used. A power law model often can approximately describe the spectral noise density of frequency standards over a band $0 < f \leq f_h$ of Fourier frequencies rather than sharp values, where f_h is an upper cutoff frequency as

$$S_{\nu}(f) = \sum_{\alpha=-2}^{\alpha=2} h_{\alpha} f^{\alpha} = \frac{h_{-2}}{f^2} + \frac{h_{-1}}{f} + h_0 + h_1 f + h_2 f^2. \quad (3.16)$$

Five noise types can be classified by the exponent, α , on the Fourier frequency, f , for the spectral density $S_{\nu}(f)$ with $\alpha = -2$ random walk frequency noise, $\alpha = -1$ flicker frequency noise, $\alpha = 0$ white frequency noise (random walk phase noise), $\alpha = 1$ flicker phase noise and $\alpha = 2$ white phase noise. These noise types are illustrated in Fig. 3.10.

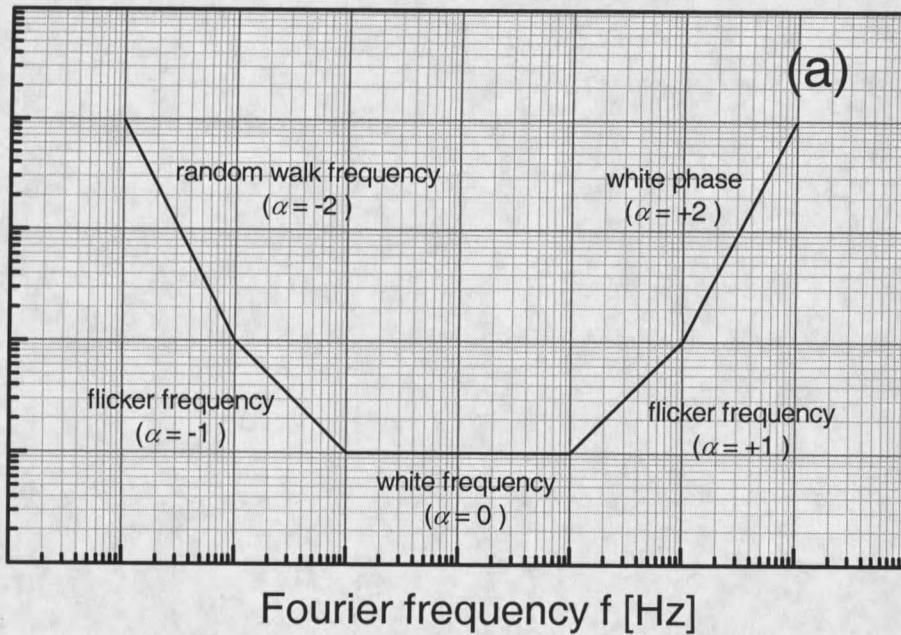
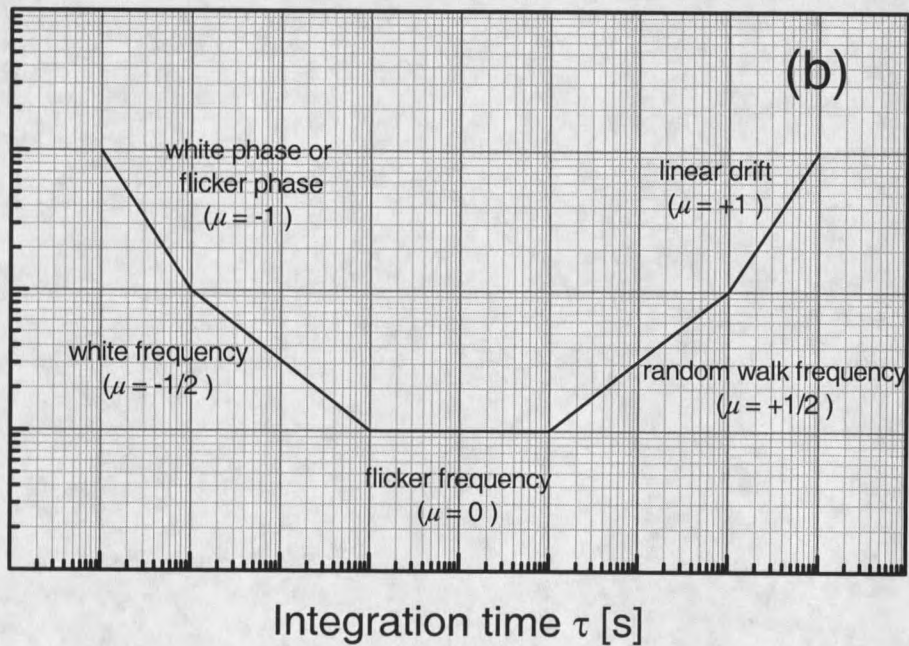
Spectral noise density $S_v(f)$ [Hz^2/Hz]Allan deviation $\sigma_y(\tau)$ [Hz]

Fig.3.10 Illustration of the power law model for the spectral noise density as a function of frequency (a) and the Allan deviation as a function of integration time (b); note double logarithmic scales. [20]

Elliot *et al* [13] have derived a relationship to calculate the laser linewidth from the spectral noise density, assuming a laser with white noise spectral density, S_v , only up to a bandwidth, B , and no noise above this frequency. If the rms frequency fluctuations $\delta v_{rms} \ll B$, then the laser line shape is Lorentzian with linewidth

$$\Delta v_l = \pi S_v \quad (3.17)$$

If $\delta v_{rms} \gg B$, a Gaussian line shape is predicted with linewidth

$$\Delta v_l = 2.35 \delta v_{rms} \quad (3.18)$$

In practice, at low frequencies the spectral noise density of oscillators tends to show random walk frequency noise and flicker frequency noise, invalidating the above relations, and a full numerical integration of the rather complicated expressions in Elliot's paper [13] has to be done.

Time Domain - The Allan Variance

Because it was found that the classical variance diverged for some types of noise commonly found in frequency standards, D. W. Allan [15] introduced what has become known as the Allan variance, $\sigma_y^2(\tau)$, to characterize frequency stability of oscillators in the time-domain. The Allan variance is the measure for instability recommended by the Institute of Electrical and Electronics Engineers (IEEE) and the International Telecommunication Union (ITU); references [11, 15, 16] give detailed information.

The Allan variance assesses the stability of a frequency standard over a time interval, τ , commonly referred to as the integration time. In an Allan variance measurement, a frequency counter determines the average frequency, f_n , over a specific time interval, τ , (Fig. 3.9) which is recorded by a computer for subsequent statistical analysis. For each time interval, τ , a series of N measurements are made. The Allan variance for a finite number of measurements is then estimated using the formula

$$\sigma_y^2(\tau) = \frac{1}{2(N-1)} \sum_{n=1}^{N-1} (f_{n+1} - f_n)^2. \quad (3.19)$$

Division by $N-1$ normalizes σ_y^2 to the number of entries in the sum, and division by 2 facilitates comparison to the classical variance in the case the f_n 's are random and uncorrelated (white noise). Only for white frequency noise ($\alpha=0$) does the classical variance equal the Allan variance. The process is repeated for different values of τ . Fewer samples are typically available for large integration times, τ . To avoid large variations, a minimum of 3 samples is required, meaning that an Allan deviation for a 10 minute integration time requires at least 30 minutes of data recording. The longer the data set duration, the better the confidence in the estimate.

The Allan deviation or root Allan variance is given by taking the square root of the Allan variance

$$\sigma_y(\tau) = \sqrt{\sigma_y^2(\tau)}. \quad (3.20)$$

Plotting the Allan deviation versus the integration time, τ , yields the Allan deviation curve, which allows inference about the type and level of noise present in the system.

Almost exclusively, Allan variance plots are actually Allan deviation plots in the literature. To compare laser systems operating at different frequencies, dividing the Allan deviation by the laser frequency, ν_0 , produces the fractional Allan deviation, $\sigma_y(\tau)/\nu_0$.

Similar to the case of spectral noise density, the nomenclature of frequency noise distributions can be associated with a truncated power law model

$$\sigma_y^2(\tau) \approx \sum_{\mu=-2}^{+1} a_\mu \tau^\mu = \frac{a_{-2}}{\tau^2} + \frac{a_{-1}}{\tau} + a_0 + a_1 \tau. \quad (3.21)$$

The classification is shown for the Allan deviation in Figure 3.10(b).

From frequency domain measurements, time domain predictions can be made using the relation

$$\sigma_y^2(\tau) = 2 \int_0^{f_h} S_\nu(f) \frac{\sin^4(\pi f \tau)}{(\pi f \tau)^2} df, \quad (3.22)$$

where f_h is the high frequency cutoff for the applicable measurement system, i.e. the measurement bandwidth. The conversion process loses some information. Generally, conversions from Allan variance to spectral noise density are impossible. This relation is useful when only one laser system is available [17, 30, 26, 28]. Since we had the luxury of two independently stabilized lasers and wanted to avoid potentially inaccurate conversions, we only used original experimental data for publications.

Table 1 summarizes the most common noise types found in frequency standards and their relation to the spectral noise density, $S_v(f)$, and Allan deviation, $\sigma_y(\tau)$. [18]

Table 1 Common noise types found in frequency standards and their relation to the spectral noise density, $S_v(f)$, and Allan deviation, $\sigma_y(\tau)$. [18]

Type of noise	α	μ	$S_v(f)$	$\sigma_y(\tau)$
Random walk frequency	-2	1/2	$h_{-2}f^{-2}$	$\sqrt{h_{-2} \frac{2\pi^2}{3} \tau^{\frac{1}{2}}}$
Flicker frequency	-1	0	$h_{-1}f^{-1}$	$\sqrt{h_{-1} 2 \ln 2}$
White frequency	0	-1/2	h_0f^0	$\sqrt{\frac{h_0}{2} \tau^{\frac{1}{2}}}$
Flicker phase	1	-1	h_1f^1	$\sqrt{h_1 \frac{3}{4\pi^2} [1.77 + \ln(2\pi f_h \tau)] \tau^{-1}}$
White phase	2	-1	h_2f^2	$\sqrt{h_2 \frac{3f_h}{4\pi^2} \tau^{-1}}$

The External Cavity Diode Laser

The semiconductor laser was invented by Basov *et al.* [19] in the early 1960's and its ease of operation has made it one of the most widely used laser systems covering wavelength windows from ~ 635 nm (AlGaInP) to $10 \mu\text{m}$ (Pb-salt). Diode laser wavelength coverage is not continuous, and performance characteristics vary widely depending on the wavelength. Semiconductor lasers operating at the optical transmission frequencies of optical fibers, at 229 THz ($1.3 \mu\text{m}$) and 193 THz

(1.55 μm), have become particularly important in the optical telecommunication industry, because they can be mass-produced, have low power consumption, and are reliable. For the commercially most important wavelengths, in addition to traditional Fabry-Perot-type lasers, more complex resonator structures on the semiconductor chip have been developed leading to distributed feedback (DFB) and distributed Bragg reflector (DBR) lasers. For these lasers, the selective reflectivity of the distributed grating determines the lasing oscillation wavelength. Recently, diodes emitting blue light (GaN) have become commercially available, of particular importance in optical data storage systems; because the storage density is inversely proportional to the square of the wavelength of the light used, approximately four times higher data storage can be achieved than with near-infrared laser diodes. [20] High-power, wide-stripe laser diodes that run multimode have become important as pump sources in solid-state lasers, fiber amplifiers, and tapered amplifier systems.

Many scientific applications, in particular high-resolution laser spectroscopy, require the laser to operate narrowband, in a single spatial and frequency mode, over the spectral range of interest. Linewidth narrowing, continuous tuning, and stable operation can be accomplished by using dispersive optical feedback to the laser diode.

The external cavity diode laser (ECDL) system used for all of our stabilization and spectroscopy experiments was developed at Montana State University. Gregg W. Switzer and J. L. Carlsten first developed the local design for application in a miniature water vapor lidar system suitable for measurement of water vapor in the

Martian atmosphere at a wavelength of ~ 935 nm. [21] G. C. Dodge further refined and modified the mechanical design to allow easy pivot point adjustment and operation at 1550 nm. Two external cavity diode lasers (named Max & Moritz) were assembled, aligned, and characterized by the author. Performance characteristics of the laser system will be discussed in subsequent sections, and information on electronic drivers and feedback circuitry is presented in appendix A.

Principle of Operation

Free running solitary laser diodes have relatively large linewidths on the order of 10's of MHz, very large relative to atomic transitions, due to a low optical cavity quality factor, a result of the facet reflectivities of $R \sim 30\%$ and cavity lengths of ~ 100 μm . Injecting a current between the n and p cladding layers in the active region of the diode generates laser light. Current injection produces electron-hole pairs that recombine and emit photons with high quantum efficiency. The semiconductor material band gap, a function of temperature and carrier density, determines the nominal emitted wavelength, and a broad gain curve typically leads to multimode operation. Single wavelength operation requires careful selection of operating temperature in conjunction with the diode laser injection current. Wavelength tuning with temperature is often accompanied by sudden jumps in amplitude and phase (mode-hops) as the laser oscillation jumps to the next cavity mode.

External cavity diode lasers, in contrast, allow single mode operation and tuning to any wavelength within the gain curve of the laser diode as long as tuning of wavelength selective elements can be synchronized. Ideally, the laser diode itself becomes a pure gain element; an external resonator acts as a mode selector, allowing gain for only one mode of the external cavity. Apart from excellent tuning characteristics, external cavity diode lasers have linewidths on the order of 10's of kHz over a few milliseconds, sufficient for many applications in spectroscopy and important as a starting point for active frequency stabilization, since servo requirements needed to suppress the inherent frequency noise become less demanding.

The Littman-Metcalf optical feedback configuration, [22] first introduced for dye laser oscillators, was chosen for the lasers constructed and used in this work because it has distinct advantages: a) there is no output beam steering - important for the alignment of subsequent optical elements, b) double passing the dispersion grating at grazing incidence gives better spectral resolution, and c) using a knife-edge prism instead of a plane mirror as the retro reflector makes the cavity configuration mechanically more stable by making the tilt degree of freedom unimportant.

The Littrow configuration, in contrast, operates on only a single pass of the dispersing grating and provides higher optical output power. Beam steering, however, needs compensation, which makes the beam mechanically unstable and causes difficulties in producing long continuous scans.

ECDL Construction and Characterization

Since the laser diode in an ECDL should act only as a gain element, longitudinal facet modes caused by the miniature Fabry-Perot resonator are not desirable. Single angled facet (SAF) diodes offer an alternative, and they were used instead of anti-reflection coated diodes. [23] In SAF-diodes, the wave-guide region was grown so that it intersects the cleavage plane at normal incidence on the back facet and at an angle of ~ 7 degrees at the front facet. Photons reflecting off the front facet are absorbed in the substrate material; this together with the low reflectivity of the angled facet of $R \sim 2 \times 10^{-5}$ removes the Fabry-Perot cavity for this diode structure. The particular GaInAsP/InP diodes used were custom grown by Quantum Photonics, Inc. and packaged in a standard 9 mm can with the output facet open to potential outside contamination. Electrical pin outs were only provided for laser anode and laser cathode, without a photodiode that monitors the output of the lasers' back facet. The gain peak occurred at ~ 1535 nm, very close to the optical transitions of interest, extending ~ 30 nm in either direction (measured @ 150 mA, $T = 20^\circ$ C). The diodes were driven forward biased with a low noise laser driver constructed by the author (see Appendix A).

The optical configuration of the laser is shown in Fig 3.11 (figure courtesy of G. W. Switzer [21]). The highly divergent laser light emitted from the SAF-diode is collimated using an aspheric collimating lens with numerical aperture $NA = 0.55$ and focal length 3.1 mm (Thorlabs). An 8 mm wide region of a gold-coated holographic

grating with 1000 lines/mm obtained from American Holographic, Inc. disperses the collimated light at a grazing incidence of 87 degrees. The grating efficiency was measured to be ~35 % into the first diffraction order.

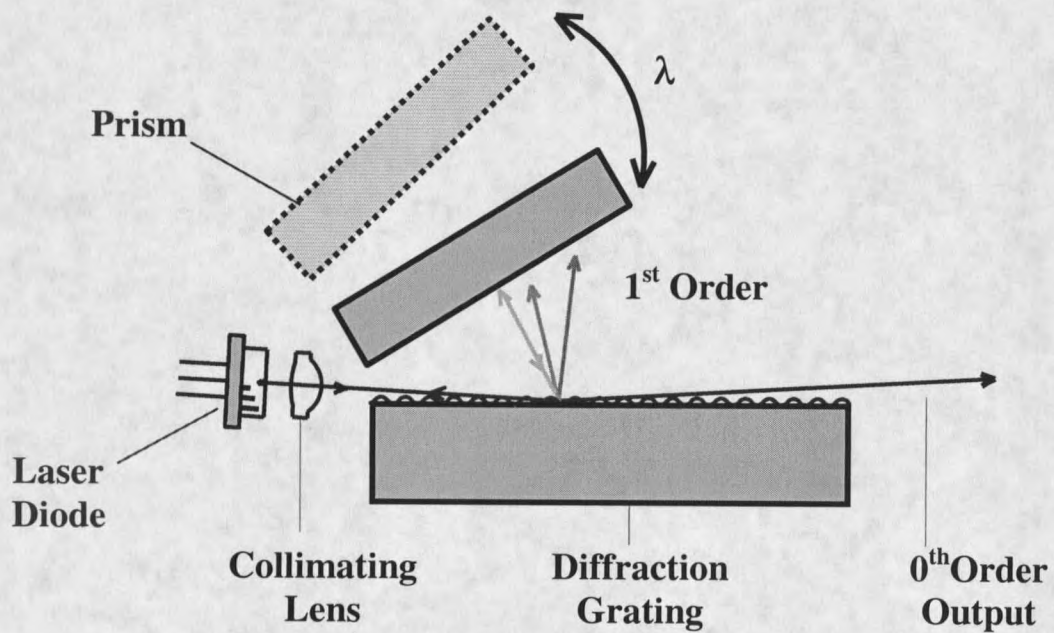


Figure 3.11 Schematic of the external cavity diode laser in the Littman-Metcalf configuration (figure courtesy of G. W. Switzer). [22]

A knife-edge roof prism, custom made by Continental Optics, Inc. and anti-reflection coated by Optosigma, was used to retro-reflect a selected wavelength of the first order back into the diode for oscillation. All other wavelengths exit the cavity below lasing threshold. Using a knife-edge roof prism removes the requirement of a critical tilt adjustment needed with a plane mirror. The 0th order of the diffraction grating has about 50 % efficiency and serves as the optical output coupler.

The ECDL's constructed using SAF-diodes exhibit unparalleled performance relative to those with anti-reflection coated diodes. The side-mode suppression ratio (SMSR), defined as the ratio of optical power in the highest intensity mode to the next highest intensity mode, was measured by coupling part of the laser light into an optical spectrum analyzer Model HP7095OB. Figure 3.12 shows the ECDL spectrum near 1535 nm, the center wavelength of the diode's gain peak, while operated at 100 mA injection current. As a result of the low reflectivity of the angled facet, a side-mode suppression ratio of ~ 51 dB relative to the central mode was achieved, a significant improvement over commercially available ECDL's which typically show SMSR of 40 - 45 dB.

The optical output power of the ECDL named "Max" measured as a function of injection current (PI-curve) is shown in Figure 3.13 along with the PI-curve for the plain diode without feedback. Threshold current is 43 mA with a slope efficiency of 0.12 mW / mA. The optical output power reaches 4 mW at 75 mA. To extend the lifetime and to avoid heating and damage resulting from high optical power densities

on the facets, both lasers were operated with 60 mA injection current, giving ~1.9 mW optical output power for applications. This performance was lower than expected when the diodes were purchased. Amplifying the laser output with an Erbium doped fiber amplifier (EDFA) readily produced higher output power.

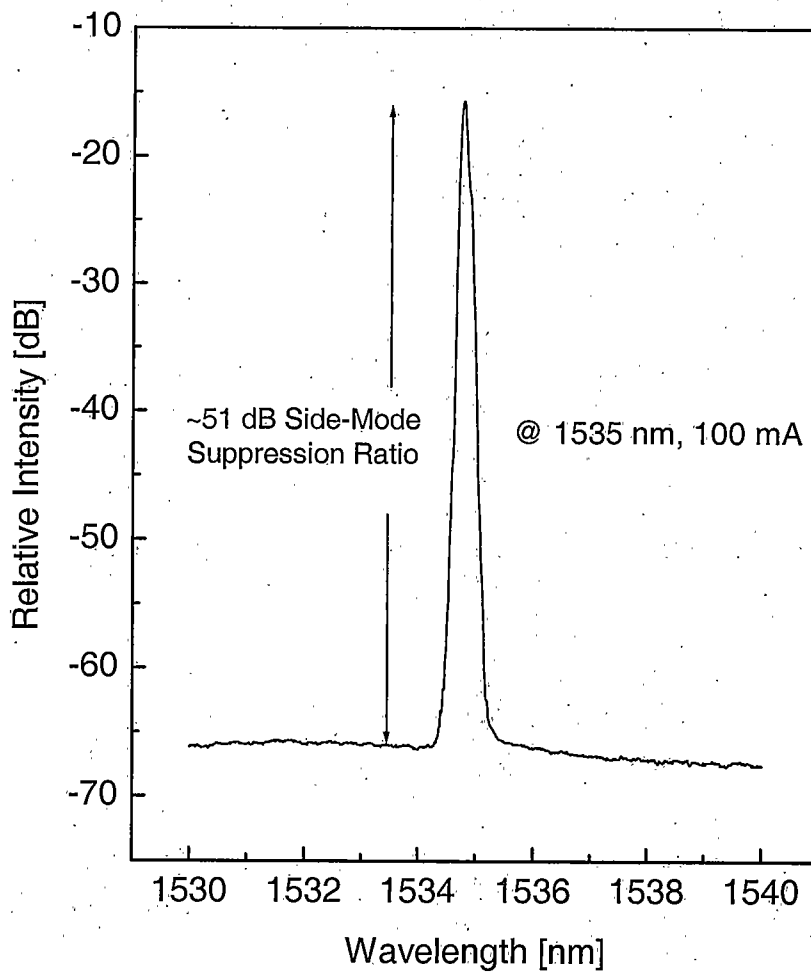


Figure 3.12 ECDL-spectrum near 1535 nm showing a side-mode suppression ratio of ~ 51 dB. The width of the peak was limited by the 0.5 nm resolution of the optical spectrum analyzer.

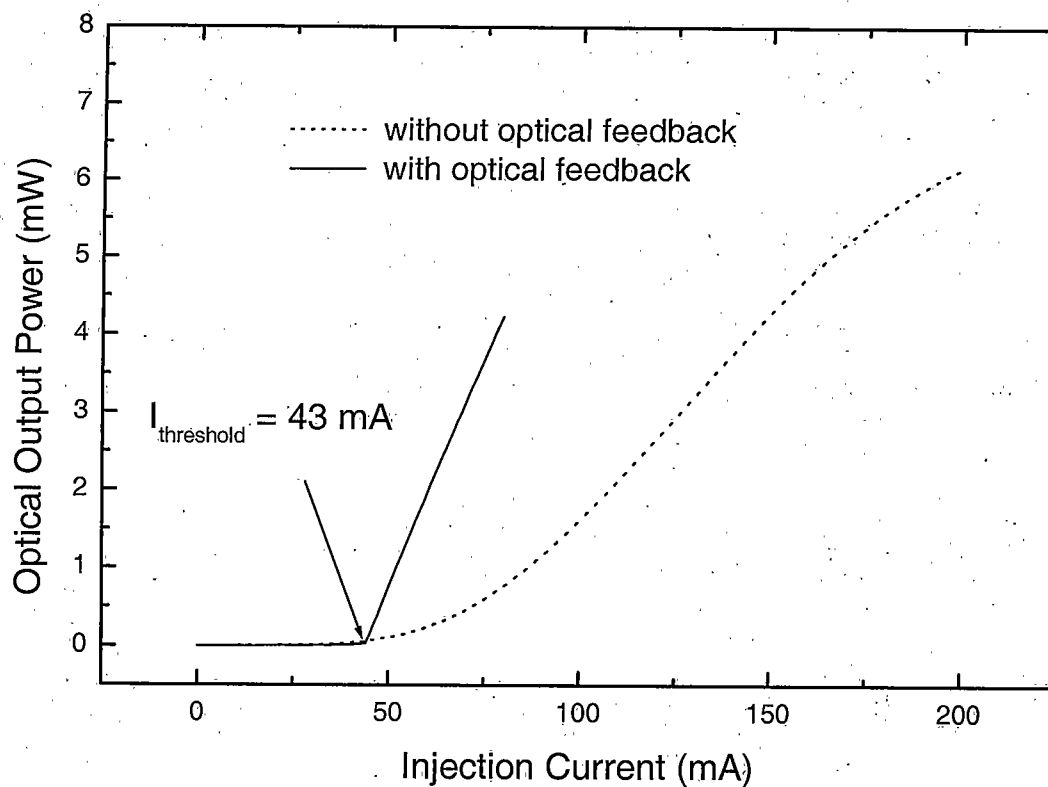


Figure 3.13 Optical output power versus injection current (PI curve) for the ECDL "Max". At a threshold current of 43 mA the ECDL "Max" begins lasing.

As mentioned earlier, diode laser output characteristics are strongly temperature dependent. Hence, flawless diode laser operation requires strict temperature control. This was achieved by placing the aluminum base plate of the laser cavity onto two Melcor 15 x 30 mm thermo-electric coolers with feedback for a control circuit provided by a calibrated 10 k Ω thermistor placed close to the coolers. A Wavelength Electronics model LFI-3526 T- controller exhibiting excellent stability (< 2 mK over 1 h, < 5 mK over 5 h) controlled the temperature and was tuned to stabilize the coolers at just below ambient room temperature of $\sim 19^{\circ}\text{C}$. Maintaining near

ambient room temperature of the laser cavity avoids condensation on the diode laser facets. Due to the lethargic response (minutes) of the lasers' large thermal mass aluminum components, temperature tuning was not used for active laser frequency stabilization.

Frequency tuning the laser in single mode is important for spectroscopic applications, and tuning transducers provide the leverage for frequency stabilizing the ECDL. The output laser wavelength of the ECDL was tuned by changing the angle of the feedback prism plate. The prism plate contains a fine pitch screw that rests on the top of a 20 mm piezo-electric tuning (PZT) stack (Thorlabs) held in the base plate. The screw provides coarse wavelength tuning, whereas applying a voltage to the PZT stack provides continuous tuning. Mode-hop-free tuning of the laser requires the physical length of the cavity and the wavelength selected by the cavity to change simultaneously. The grating pass band must exactly synchronize with the accompanying change in cavity length. This requires very careful positioning of the prism plate pivot point using orthogonal dovetail slides to adjust the pivot point's vertical and horizontal position. [24] When adjusted correctly, all mode hops were eliminated over the full range of the diode's gain bandwidth. The reliability of this technique eliminated retuning of the external cavity during 1.5 years of operation.

At an injection current of 70 mA, coarse tuning (Max) covered a range of 66 nm, between 1493 nm and 1559 nm. Continuous tuning over ~ 47 GHz was possible by applying a 150 V DC-voltage ramp to the PZT stack and is shown in Fig. 3.14.

Measuring the laser output frequency with a Burleigh WA 1500 wavemeter, gave a PZT transducer transfer function of $K = 0.3 \text{ GHz} / \text{V}$. The prism plate assembly was made as light as possible to reduce errors from inertia. Repetitive scans at up to 1 kHz have been demonstrated, limited by mechanical resonances to be investigated in the following sections. Since changing the feedback-prism plate angle is a mechanical process, the response on tuning is rather slow. In contrast, tuning the laser by modulating the injection current to the laser diode is very fast, and a transducer transfer function of $K = 30 \text{ MHz}/\text{mA}$ has been achieved. Knowledge of the tuning limitations is crucial in the context of laser frequency stabilization.

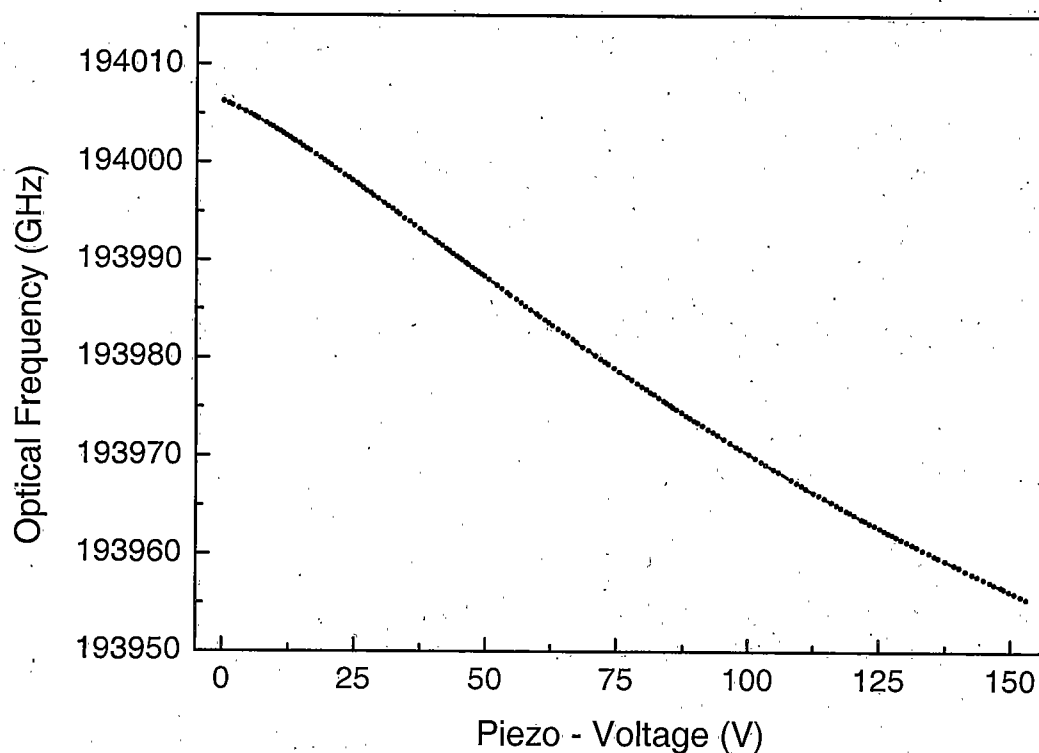


Figure 3.14 Continuous tuning curve for ECDL "Max". Continuous tuning is demonstrated over $\sim 47 \text{ GHz}$, center wavelength $\sim 1535 \text{ nm}$, $I = 60 \text{ mA}$.

ECDL Transducer Response

Assessing the ECDL transducer response and the actual frequency noise present on the free-running ECDL are important steps in designing a proper servo loop necessary to suppress laser frequency noise. Figure 3.15 shows the experimental setup used to measure the transducer frequency response. This setup was similar to that for measuring the spectral noise density of the free running laser described below. A low finesse Fabry-Perot cavity (Burleigh) was used as a discriminator to convert frequency modulation (FM) into amplitude modulation (AM). This cavity had a length of 15cm, giving a free spectral range (FSR) of ~ 1 GHz. The cavity finesse, F , of ~ 2.1 was determined by scanning the cavity across the laser line width and calculating the ratio of the free spectral range to the cavity transmission band. In order to measure the transducer response of the ECDL, the laser was manually tuned to operate at the side of the transmission fringe, so that laser frequency fluctuations could be translated into amplitude fluctuations, detected by a New Focus 1811 InGaAs photodiode. An HP network analyzer, Model HP 3589A, with its source output connected to the current modulation input port of the laser diode driver (see appendix A) measured the injection current frequency response of the ECDL. The HP network analyzer also measured the frequency response of the PZT driven feedback prism plate through the Thorlabs MDT 691 PZT-amplifier. The detector output was connected to the input port of the network analyzer. Logarithmic scans of the network analyzer were performed, covering 10 Hz to 100 kHz for measuring the

PZT frequency response and 10 Hz to 100 MHz for measuring the injection current frequency response. Results of these measurements are shown in Fig. 3.16 (a) and (b) for the PZT amplitude and phase, and Fig. 3.16 (c) and (d) for the injection current amplitude and phase, respectively.

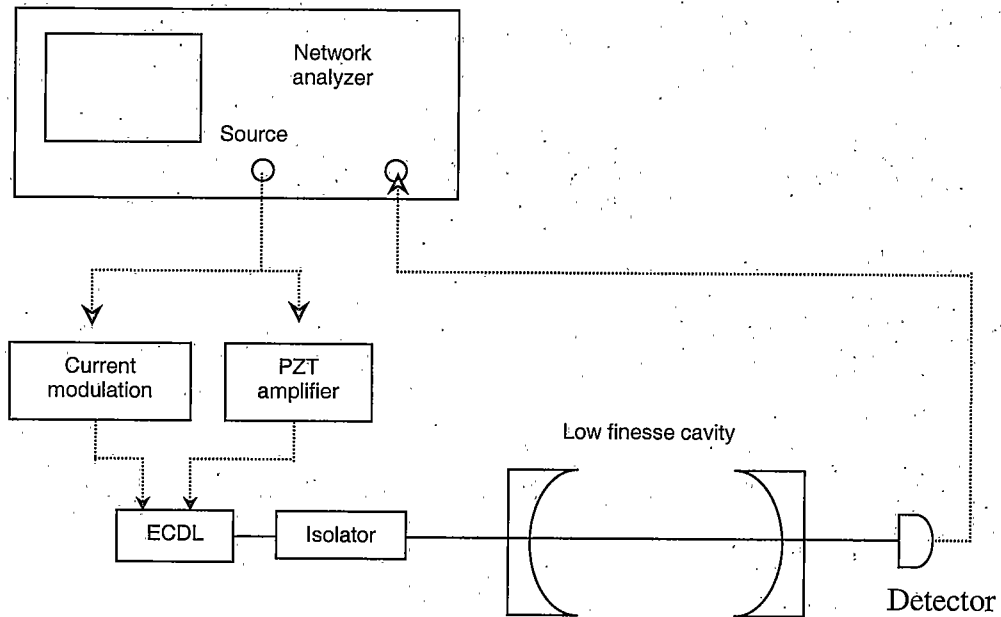
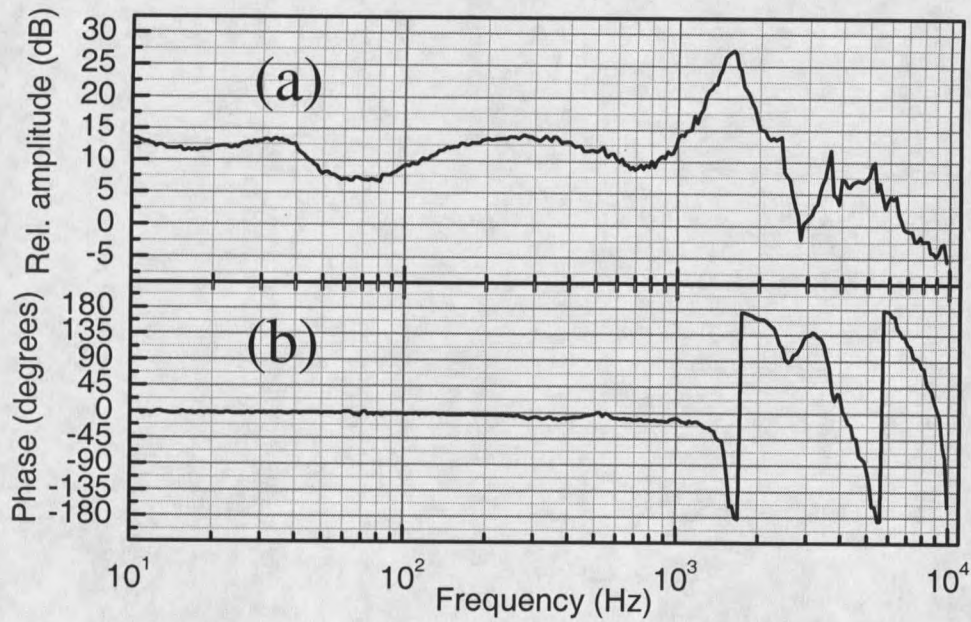


Figure 3.15 Experimental setup used to measure the transducer response of the ECDL with a low finesse cavity as a frequency discriminator.

PZT response



Current response

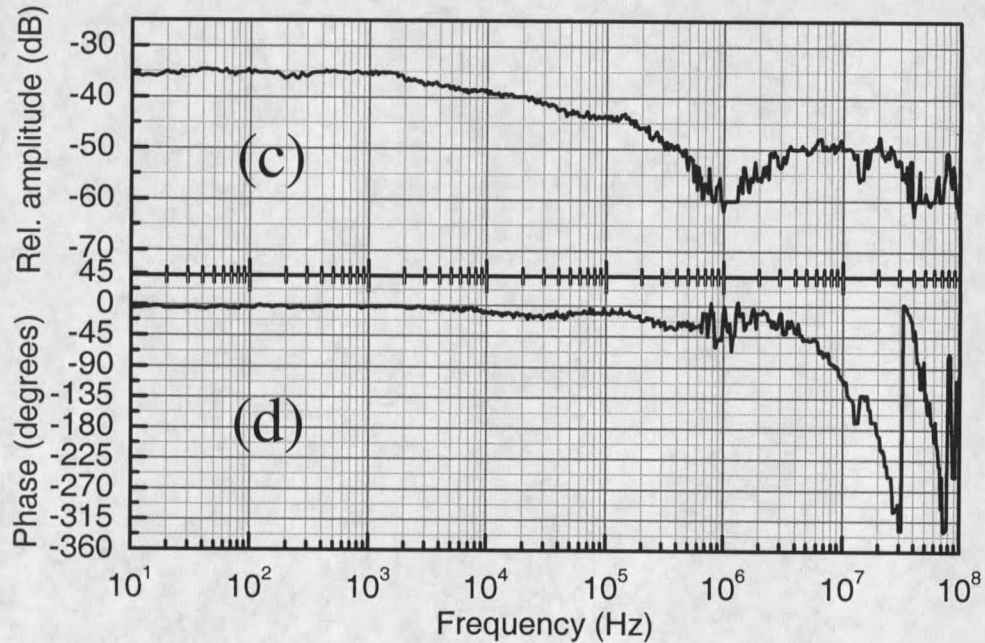


Figure 3.16 Transducer response of the tuning elements of the ECDL, relative amplitude (a) and phase (b) of the piezo-driven (PZT) feedback prism plate assembly, relative amplitude (c) and phase (d) of the diode current modulation.

The PZT displayed a fairly flat response up to about 1 kHz. Beyond 1 kHz, a significant resonance occurs, which leads to a phase shift of 180 degrees. This resonance was attributed to a mechanical resonance in the feedback prism plate assembly of the ECDL, and similar resonances have been observed in other laboratories. Independent spectral noise density measurements, reported in the following section, further supported this conclusion. To properly design the feedback servo circuit, the transducer tuning elements' resonant frequencies must be known and avoided. Positive feedback to the laser, caused by a phase shift of more than 180°, could lead to severe laser oscillations. The low bandwidth PZT loop was designed to keep the high bandwidth loop of the laser diode's injection current frequency control in the center of its dynamic range. Therefore, the unity gain point was confined to a value below 1 kHz (see appendix A).

The frequency and phase response to changes in the injection current showed a fairly flat response up to about 1 MHz. At 1 MHz the amplitude of the response had decreased by ~ 20 dB. Hence, with high bandwidth feedback electronics available, intrinsic noise suppression up to these 1 MHz frequencies can be accomplished without inordinate technical difficulty. Indeed, the injection current servo, detailed in appendix A, provided bandwidths in the order of ~ 1 MHz.

Spectral Noise Density of the free running ECDL

Error signal analysis allowed a direct measurement of the spectral noise density $S_V(f)$ of the free running laser using a static discriminator slope D [V/Hz], which converted the frequency modulation [Hz] on the laser, caused by frequency fluctuations, into amplitude modulation [V], a conveniently measurable quantity. To obtain a large discriminator slope, D , a narrow optical transition in isotopically pure (99.9 % ^7Li) $^{170}\text{Er}^{3+}:\text{YLiF}_4$ was chosen as the frequency reference. [25] Roger M. Macfarlane of IBM and Richard S. Meltzer from the University of Georgia, Athens, kindly provided this crystal, which was grown by Arlette Casanho. During the measurement, the laser frequency was compared to the center frequency of the transition, using an error signal proportional to the frequency difference between the two frequencies. The experimental setup, shown in Fig. 3.17, was based on FM-spectroscopy of a narrow inhomogeneously broadened ~ 150 MHz (FWHM) $\text{Er}^{3+}:\text{YLiF}_4$ transition. This heterodyne technique overcame the problem of low frequency AM of the laser, which could have been wrongly interpreted as FM noise, by detecting at the high RF modulation frequency, where intrinsic laser intensity noise was very small. The ECDL, optically isolated by a Faraday rotator (OFR Model 10-4-1550-VLP), was externally phase modulated by a broadband New Focus electro-optic phase modulator Model 4002 driven at 109.5 MHz by a PTS 500 frequency synthesizer through a custom-made resonant tank built by the author (see appendix A).

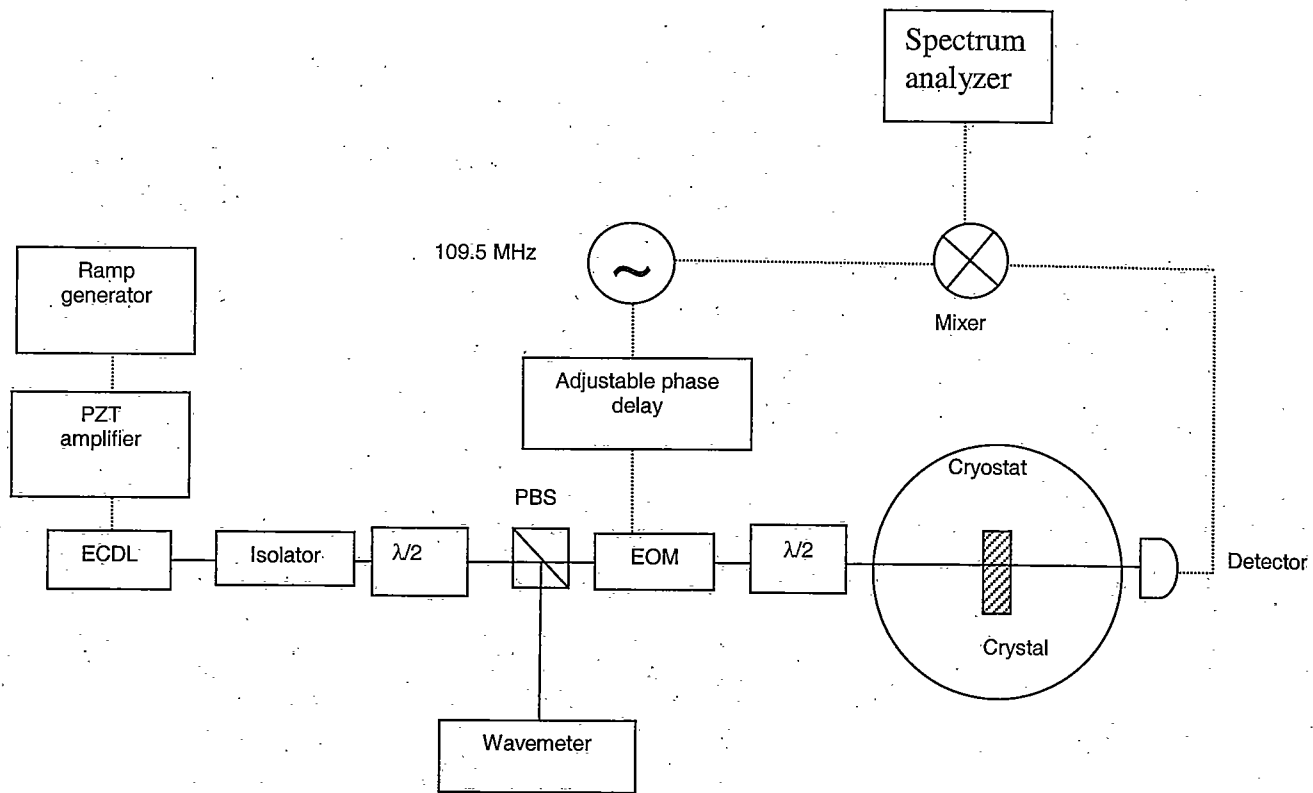


Figure 3.17 Experimental setup for measuring the spectral noise density of the free running laser.

The sideband frequency was chosen to optimize the error signal slope within the 125 MHz bandwidth of the New Focus 1811 InGaAs photo detector. The laser frequency was monitored with a Burleigh WA 1500 wavemeter, which allowed calibration of the error signal to within the 0.1 ppm accuracy of the wavemeter. For this purpose linear scans of the laser frequency were provided by applying a sawtooth voltage ramp to the PZT driving the feedback prism plate of the laser. A Stanford Research Systems SR 345 function generator amplified by a Thorlabs model MDT 691 PZT amplifier generated the ramp. In order to optimize the signal, a $\lambda/2$ -waveplate in front of the cryostat allowed for adjusting the polarization of the beam. The detected transmitted light was heterodyned with the 109.5 MHz local oscillator, and the phase shifter was adjusted to obtain the dispersive error signal. Spectral analysis of the error signal above 1 kHz was performed with an HP-spectrum analyzer Model HP E4411B while a Wavetek spectrum analyzer Model 5820 was used for frequencies below 1 kHz. The optical power of the laser beam was adjusted using the $\lambda/2$ -waveplate/polarizing beam splitter (PBS) combination to 140 μW . The $\text{Er}^{3+}:\text{YLiF}_4$ crystal was placed in an Oxford SpectroMag cryostat at $T = 10$ K to avoid any spectral hole burning. The crystal was oriented with its c-axis parallel to the laser's k -vector and perpendicular to the external B -field. To separate the narrow optical transitions contained in the multiplet located at 6534 cm^{-1} , a small magnetic field of $B = 0.2$ T was applied. The error signal yielded a linear slope at line center of $D = 3.746 \times 10^{-7} \text{ V/Hz}$, which was used to convert the spectrum

analyzer output [dBm] into spectral noise density, $S_{\nu}(f)$, of the laser frequency fluctuations [$\text{Hz}/\sqrt{\text{Hz}}$]. To measure the spectral noise density of the free running ECDDL, the laser was manually tuned to the center of the $\text{Er}^{3+}:\text{LiYF}_4$ transition using the PZT. No active servo feedback was engaged for this measurement. The error signal was spectrally analyzed using specific analyzer resolution bandwidths appropriate to the different frequency measurement intervals; sufficient frequency overlap between individual measurements was assured.

Figure 3.18 shows the result of this measurement on a log-log plot of the rms spectral noise density versus frequency. Three noise types common to frequency standards, indicated by asymptotes of distinct slopes, can be distinguished according to the power law model relation (3.16) for the spectral noise density. For frequencies up to tens of Hz, random walk frequency noise ($\alpha = -2$, slope = -1) was prevalent, followed by flicker frequency noise ($\alpha = -1$, slope = -1/2) for frequencies up to tens of kHz. The white noise frequency floor ($\alpha = 0$, slope = 0) was reached at frequencies at approximately 100 kHz. Structural resonances in the laser cavity caused narrow-band frequency noise. A distinct bump was observed at ~ 1 kHz and can be assigned to a mechanical resonance in the feedback prism plate assembly of the external cavity excited by acoustical laboratory noise, prevalent in the kHz range, coupling into the laser cavity. This issue was already evidenced in the PZT transducer frequency response (see previous section). To alleviate this problem, passive acoustical isolation of the laser was required. An acoustical isolation box

was constructed to cover the optical setup for locking experiments in Er^{3+} :KTP (see section: Laser frequency stabilization to regenerative spectral holes in Er^{3+} :KTP in Chapter 4). The sharp features at 60 Hz and 120 Hz are due to pickup from the power supply.

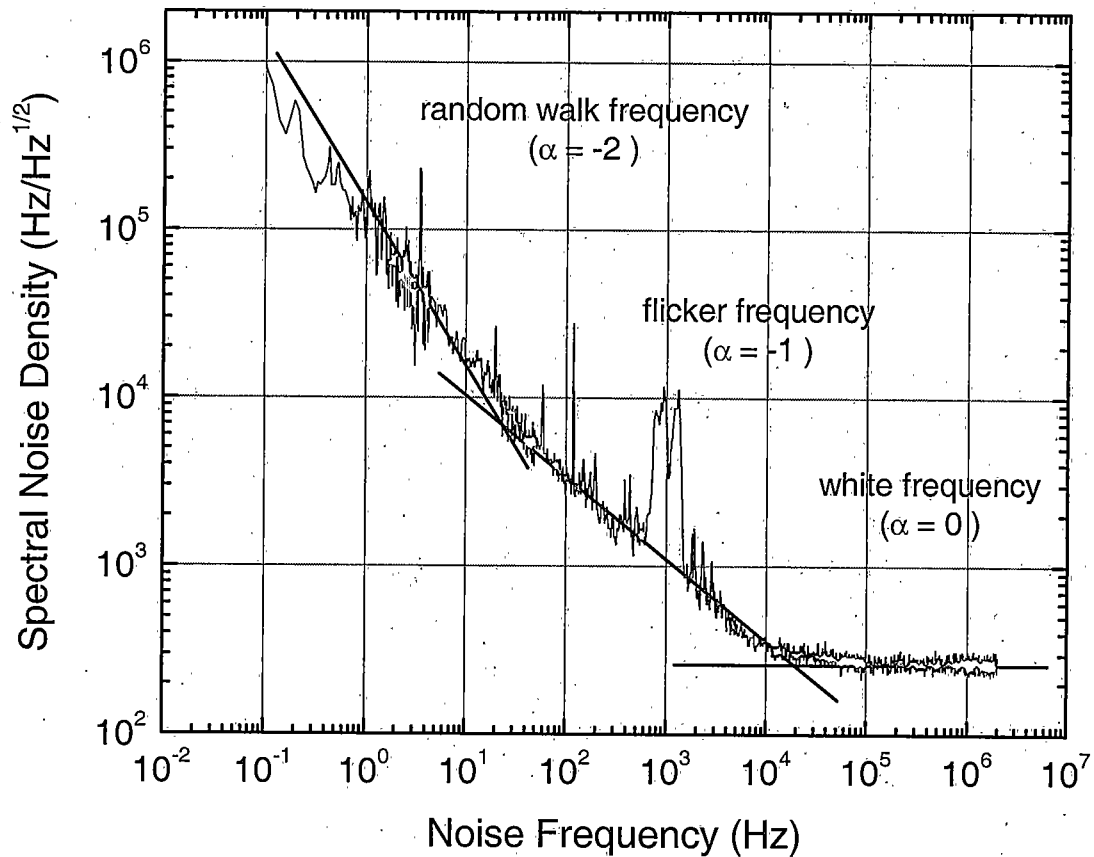


Figure 3.18 Spectral noise density of the free running ECDL as a function of noise frequency; note double logarithmic scales.

The substantial amount of noise present at low frequencies exhibiting a $\sim 1/f$ and $\sim 1/f^2$ frequency dependence, typical for external cavity diode lasers [26,27,28,29,30], indicated the need for a servo loop of high gain at these frequencies. However, a relatively low bandwidth (~ 1 MHz) electronic feedback loop should be sufficient to suppress this laser noise compared to the feedback bandwidths of tens of MHz needed to suppress the noise found in solitary diodes [31, 32]. The injection current servo is documented in Appendix A.

REFERENCES

1. G. C. Bjorklund: IBM Invention Disclosure SA 8790135 (March 1979).
2. G. C. Bjorklund, *Optics Lett.* **5**, 15 (1980).
3. J. L. Hall, *Science* **202**, 147 (1978).
4. J. L. Hall, L. Hollberg, T. Baer, and H. G. Robinson, *Appl. Phys. Lett.* **39**, 680 (1981).
5. R.W. Drever, J. L. Hall, F. V. Kowalski, J. Hough, G. M. Ford, A. J. Munley, and H. Ward, *Appl. Phys. B* **31**, 97 (1983).
6. R. V. Pound, *Rev. Sci. Instrum.* **17**, 490 (1946).
7. J. M. Supplee, E. A. Whittaker, and W. Lenth, *Appl. Optics* **33**, 6294 (1994).
8. G C. Bjorklund and M. D. Levenson, *Appl. Phys. B* **32**, 145 (1983).
9. B. I. Bleaney and B. Bleaney, *Electricity and Magnetism (volume 2)*, Oxford University press, 1989, 3rd edition.
10. T. Day, E. K. Gustafson, and R. L. Byer, *IEEE Journal of Quantum Electronics* **28**, 1106 (1992).
11. NIST Technical Note "*Characterization of Clocks and Oscillators*" (US Government Printing Office), Vol. 1337 (1990).

12. M. Roberts, P. Taylor, P. Gill, NPL report CLM 8, February 1999.
13. D.S. Elliot, R. Roy, and S.J. Smith, Phys. Rev. A **26**, 12 (1982).
14. B.C. Young, F.C. Cruz, W.M. Itano, and J.C. Bergquist, Phys. Rev. Lett. **82**, 3799 (1999).
15. D.W. Allan, IEEE Transactions on Ultrasonics, Ferroelectrics, and Frequency Control, UFFC **34**, 647 (1987).
16. Hewlett Packard Application Note **1289**, 56 (1997).
17. J. Dirscherl, B. Neizert, T. Wegener, and H. Walther, Opt. Comm. **91**, 131 (1992).
18. J. A. Barnes, A.R. Chi, L.S. Cutler, D.J. Healey, D.B. Leeson, T.E. McGunigal, J.A. Mullen, Jr., W.L. Smith, R.L. Sydnor, R.F.C. Vessot, and G.M.R. Winkler, IEEE Trans. Instrum. Meas. **20**, 105 (1971).
19. N.G. Basov, O.N. Krokhin, and Y.M. Popov, JETV **40**, 1320 (1961).
20. S. Nakamura, W. Kaenders, Laser Focus World **35** (4), 69 April (1999).
21. G. Switzer, PhD thesis, Montana State University 1998.
22. K. Liu and M.G. Littman, Opt. Lett. **6**, 117 (1981); P. McNicholl and M.J. Metcalf, Appl. Opt. **24**, 2757 (1985).

23. P.J.S. Heim, Z.F. Fan, S.-H. Cho, Keeyol Nam, M. Dagenais, F.G. Johnson, and R. Leavitt, *Electr. Lett.* **33**, 1387 (1997).
24. The dovetail slides were added to the original external cavity design by mechanical engineering student G. C. Dodge.
25. R.M. Macfarlane, R.S. Meltzer, and A. Cassanho, *Phys. Rev. Lett.* **69**, 542 (1992).
26. T. Kurosu, J. Ishikawa, and N. Ito, *Appl. Phys. B* **63**, 265 (1996).
27. J. Kawakami, M. Kouroggi, and M. Ohtsu, *Jpn. J. Appl. Phys.* **33**, 1623 (1994).
28. G. Bianchini, P. Cancio, F. Minardi, F.S. Pavone, F. Perrone, M. Prevedelli, M. Inguscio, *Appl. Phys. B* **66**, 407 (1998).
29. A. Danielli, P. Rusian, A. Arie, M.H. Chou, and M.M. Fejer, *Opt. Lett.* **25**, 905 (2000) and references therein.
30. C.-H. Shin and M. Ohtsu, *Opt. Lett.* **15**, 1455 (1990).
31. H.R. Telle and H. Li, *Electr. Lett.* **26**, 858 (1990).
32. R.W. Fox, L. Hollberg, and A.S. Zibrov, *Experimental Methods in the Physical Sciences* **29C**, 77, Academic Press (1997).

CHAPTER 4

LASER FREQUENCY STABILIZATION TO SPECTRAL HOLES

The availability of ultra-narrow SHB resonances down to 15 Hz in rare earth doped crystals, the relative immunity of spectral holes to environmental disturbances such as vibrations, and the portability and compactness of a stable laser system using SHB references with a closed cycle cryo-cooler are important features that should enable application in a variety of fields beyond those normally associated with spectral hole burning. Stabilization of mode locked lasers [1] to spectral holes also should be practical and will have applications in signal processing situations and in other contexts that require short pulses, frequency combs, or optical clocks. The SHB frequency references are well suited to applications where multiple frequencies are required and where the programmability of SHB materials allows programmable frequency differences up to the multi-GHz range or, if disordered solids are used, to the THz range. With the development of suitable photon-gated (or two-photon) SHB materials, the production of long term secondary frequency standards based on SHB may become practical. [31]

The importance of stabilization in real time optical signal processing in SHB materials is underscored by the observation that early moderate-speed demonstrations have been limited by laser frequency jitter that led to a loss in signal fidelity. [2,3,4,5,6,7] These problems can occur at several levels: a) uncontrolled

phase variations between programming pulses when repeated pulse sequences are used for writing or refreshing spectral interference gratings, b) the more extreme case where the jitter exceeds the Fourier width of the exciting pulses so that the processed pulses fail to overlap spectrally with the programming pulses, and c) the case where the jitter exceeds the Fourier width of the exciting pulses so that the exciting pulses fail to overlap. These problems can be overcome by the use of a second piece of the same signal processing material as an SHB frequency reference providing automatic frequency and phase compatibility between the signal processing material and the stabilized laser source over the time scale of interest.

[12] The limits on device performance are set then by material parameters rather than by instability of the laser. [12,14] The relative vibrational immunity of the spectral holes provides an important simplification in system design and performance for either spectroscopy or SHB devices [8,9]. This advantage is even greater when both the frequency reference and spectroscopic sample or SHB device are mounted on the same sample holder. This has been demonstrated here for $\text{Er}^{3+}:\text{Y}_2\text{SiO}_5$. Lasers stabilized to spectral holes are already playing an important role in proof-of-principle demonstrations of a variety of SHB devices [5]; the latest of which, a high-bandwidth correlator, demonstrated in $\text{Er}^{3+}:\text{Y}_2\text{SiO}_5$ at 4.2 K. [10]

Laser frequency stabilization to persistent spectral holes [11] and regenerative spectral holes [12] burned in the absorption lines of Tm^{3+} -doped insulating crystals at 798 nm and 793 nm provided excellent stability. In spectral hole burning materials covering the 1.5 μm wavelength region explored to date, regenerative (transient)

holes, such as those found in $\text{Er}^{3+}:\text{Y}_2\text{SiO}_5$ and $\text{Er}^{3+}:\text{KTP}$, have proven to be orders of magnitude narrower in frequency than persistent holes, such as in $\text{Er}^{3+}:\text{D}^{\cdot}:\text{CaF}_2$, the only material known to date exhibiting persistent spectral hole burning at 1.5 μm . Er^{3+} -doped SHB crystals exhibiting regenerative SHB ($\text{Er}^{3+}:\text{Y}_2\text{SiO}_5$, $\text{Er}^{3+}:\text{KTP}$) and persistent SHB ($\text{Er}^{3+}:\text{D}^{\cdot}:\text{CaF}_2$) have been used here to extend laser stabilization to the important 1.5 μm telecommunications band where Er^{3+} -doped crystals [13,14,29] have the frequency selectivity required for optical storage, real-time address header decoding for all-optical packet routing, [6,7] and all-optical correlation. [3,4,5]

Our demonstrations were carried out with crystals cooled to liquid helium temperatures, but higher temperature operation with 1 kHz frequency stability at 4.2 K has been demonstrated using $\text{Er}^{3+}:\text{Y}_2\text{SiO}_5$ and projection of operation up to 20 K can be made for the deuterated CaF_2 [11,32]. Alternatively, using a narrow inhomogeneous absorption line as a frequency reference, such as the ~ 150 MHz wide line found in isotopically pure $\text{Er}^{3+}:\text{LiYF}_4$ or a part per million diluted $\text{Er}^{3+}:\text{Y}_2\text{SiO}_5$ already allowed operation at 15 K.

Laser frequency stabilization to regenerative spectral holes in $\text{Er}^{3+}:\text{Y}_2\text{SiO}_5$

The stabilized diode laser - $\text{Er}^{3+}:\text{Y}_2\text{SiO}_5$ system described here exploits the regenerative SHB technique. [12] A transient spectral hole is continuously regenerated by the stabilized laser and provides a frequency reference at an arbitrarily chosen location in the inhomogeneous $\text{Er}^{3+}:\text{Y}_2\text{SiO}_5$ absorption profile.

The stability of the laser will then be determined by the dynamical properties of the SHB material together with the design of the locking system.

To substantially improve the long-term frequency stability, we have extended the locking technique by using a combination of the error signal contributions from the spectral hole and the inhomogeneous line. The reduction of longer-term drift to 7 kHz / min over several minutes obtained with the extended technique represents a substantial improvement over the 600 kHz / min reported for Tm:YAG.[12] In the old and new cases, anticipated refinements to the feedback system and frequency modulators may be expected to provide further substantial improvement over both the long and short term stability reported here, which is already 10^3 times better over important integration time scales than that for commercial lasers. As shown in Ref. 12, this provides new capabilities to probe dynamics in the neighborhood of the active rare earth ions in SHB materials and to reveal small scale level structures and dynamics out to the tens of milliseconds scale or even longer.

Methods and Apparatus

The SHB crystal chosen as a frequency reference was $\text{Er}^{3+}:\text{Y}_2\text{SiO}_5$ with an Er^{3+} concentration of 0.005 atomic percent. This material exhibits transient spectral hole burning on the ${}^4I_{15/2}(1) \rightarrow {}^4I_{13/2}(1)$ transitions at 1536.14 nm (site 1) and 1538.57 nm (site 2) by population storage in the excited state of the optically active ion. [13] The homogeneous linewidth for this crystal was determined from the

optical dephasing time T_2 obtained from two-pulse photon echo experiments at 1.6 K and $B = 0.2$ T, and the measured value $\Gamma_h \sim 5$ kHz is consistent with previously published results. [13] The homogeneous linewidth at 0.5 T is about half that at 0.2 T. In principle, the minimum line width of a shallow spectral hole burned by a narrow-band laser is $2\Gamma_h$ due to convolution of burning and reading cycles; deeper holes can be expected to become broader, since there is less saturation of material absorption in the wings of a hole than at the center.

The frequency locking experiments reported here were performed using the strongest absorption transition from the lowest Zeeman-split level for site 1 in moderate magnetic fields of $B = 0.2$ to 0.5 T; the 0.2 T magnetic field value was chosen to simulate field strengths that have been obtained using compact 1 cm diameter Nd-Fe-B permanent magnets. [4,7] The inhomogeneous linewidth $\Gamma_{inh} = 500$ MHz = 0.017 cm⁻¹ is illustrated in Fig. 4.1, where a single spectral hole has also been burned into the line.

Two frequency reference crystals were cut from the same crystal boule (batch # 7-167) to give an inhomogeneously broadened absorption of $\sim 50\%$ at line center. Crystal dimensions were 5 mm (and 4 mm) along D_1 , 6 mm (and 5 mm) along D_2 and 1 mm (and 1.2 mm) along b . Each crystal was oriented with its D_1 -axis parallel to the magnetic field, the lasers' k -vectors parallel to the b -axis, and the lasers polarized with E along D_2 . Both crystals were immersed in superfluid helium at 1.6 K in a single Oxford Instruments SpectroMag cryostat with a superconducting magnet that provided for adjustment of the magnetic field. The laser beams were

spatially separated, and the crystals were masked so that each crystal was exposed to only one beam. The spectral holes were created with irradiances of $100 \mu\text{W}/\text{cm}^2$ using $\sim 3 \text{ mm}$ beam diameters. Beam irradiance was controlled using a $\lambda/2$ -plate and a prism polarizer.

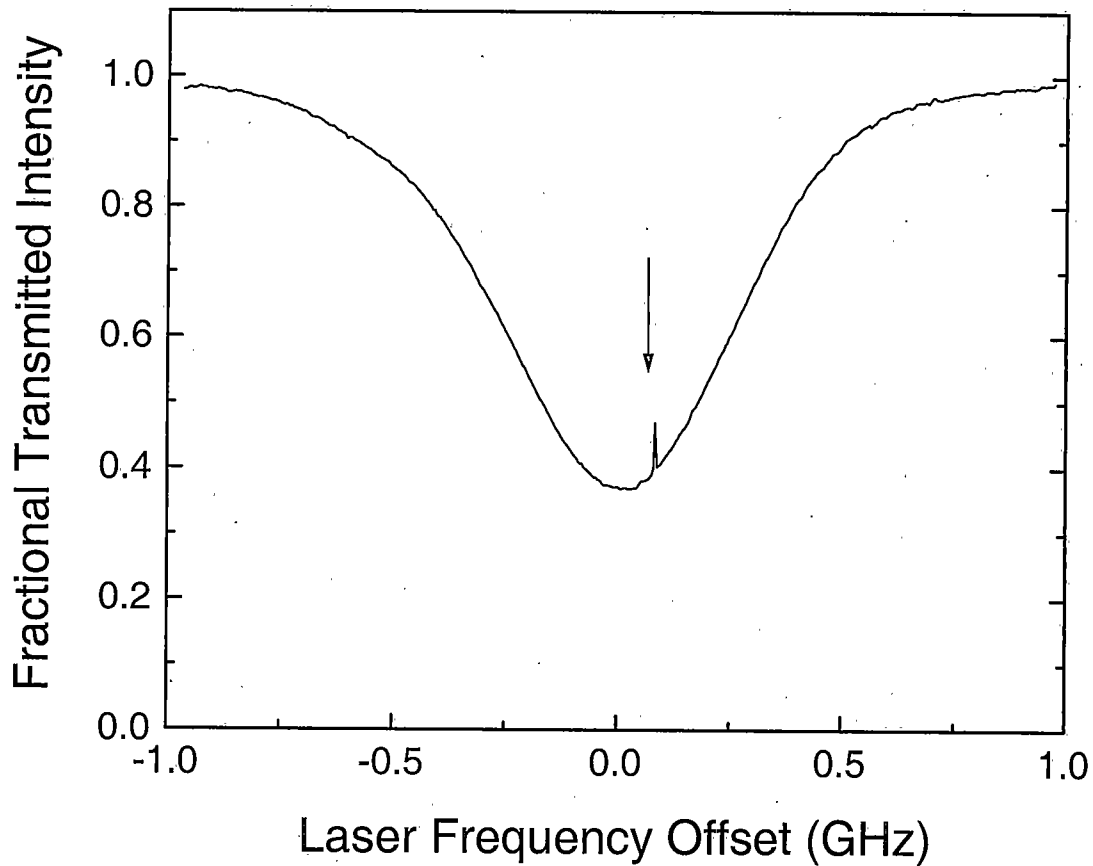


Figure 4.1 Transmission spectrum of $0.005\% \text{Er}^{3+}:\text{Y}_2\text{SiO}_5$ scanned by a diode laser showing the entire inhomogeneously broadened absorption profile at zero applied field ($B = 0 \text{ T}$). The arrow indicates a spectral hole burned by a second laser.

The experimental apparatus shown in Fig. 4.2 was similar to that described in Ref. 11 and Ref. 12. Two external cavity diode lasers in the Littman-Metcalf configuration [15], as described in Chapter 3, were used for locking the laser frequency to the spectral hole with the Pound-Drever-Hall technique. [16] The error signal was derived from the spectral hole transmission using frequency modulation (FM) spectroscopy as described in Chapter 3, [17] with the two lasers modulated by New Focus 4002 broadband external electro-optic modulators (EOM) driven at 27 MHz and 30 MHz, respectively. These frequencies greatly exceeded the spectral hole widths but were far less than the inhomogeneous absorption linewidth $\Gamma_{inh} = 500$ MHz. The primary laser side bands had a modulation index $M = 0.4$, and secondary side bands were small but observable. The sharp resonance of the spectral hole in the inhomogeneous absorption line creates a corresponding dispersion in the refractive index. Figure 4.3(a) displays the transmission spectrum through a single spectral hole in the inhomogeneously broadened absorption profile for a phase-modulated laser (including side bands), and Fig. 4.3(b) plots the demodulated FM-spectroscopy error signals obtained simultaneously for three values of relative phase, that could be continuously adjusted using a custom built phase shifter (see appendix) between the local oscillator and the EOM. In the stabilization system, each locking laser burns a hole in its reference crystal, primarily at the carrier frequency but also at the frequencies of the FM-sidebands.

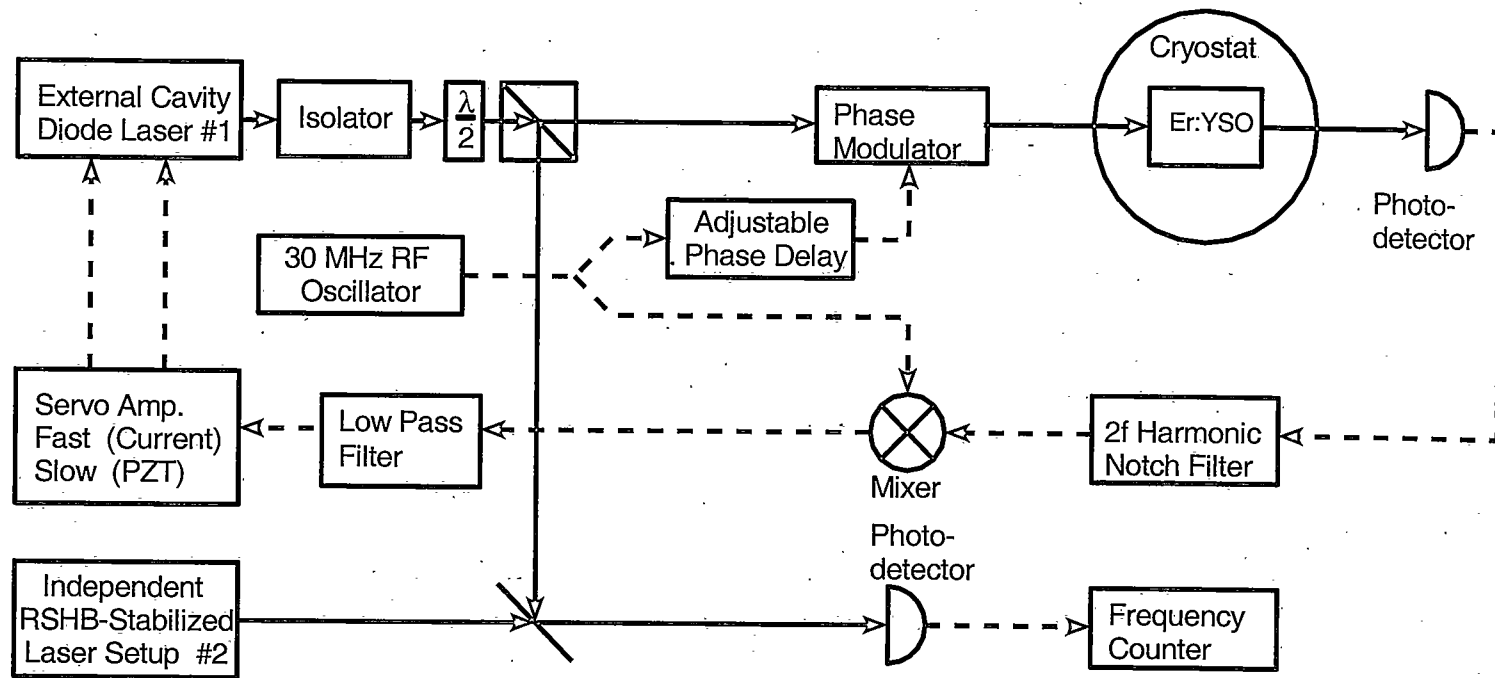


Figure 4.2 Experimental apparatus for laser frequency locking to spectral holes and beat frequency measurement of laser stability by combining the beam from the laser shown and that from an independent second laser system.

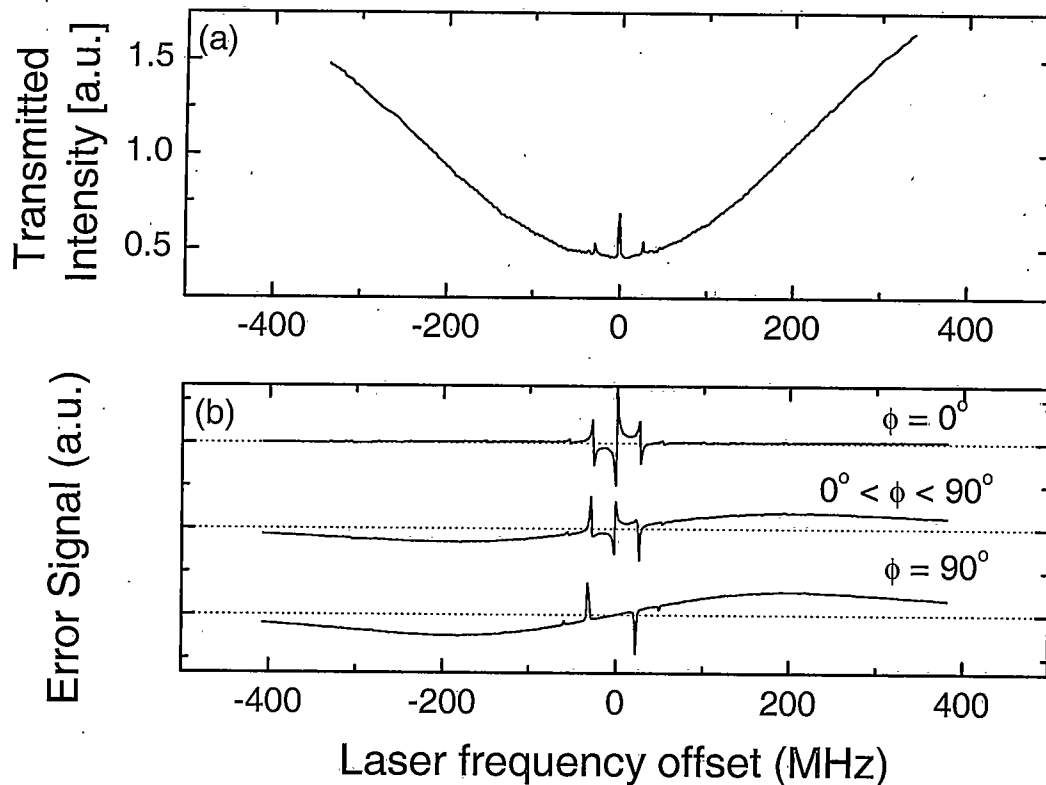


Figure 4.3 (a) Transmission spectrum, as probed by a phase-modulated laser with sidebands, of a single spectral hole burned in the inhomogeneously broadened absorption profile by an unmodulated second laser, in an applied field of $B = 0.2$ T. (b) Error signals derived from the spectral hole and the inhomogeneous line using different phase delay settings. The spectral hole is not limited to line center as chosen for illustration in this particular figure but can also occupy other positions in the inhomogeneous line.

The FM-error signal was processed by a servo loop that provided both fast corrections to the injection current of the laser diode and reduced bandwidth signals to the piezoelectric control of the laser's external feedback prism plate. Control of the prism plate angle keeps the current servo within its operating limits. A detailed description of the servo electronics and locking apparatus constructed by the author

is given in the appendices. Due to laboratory constraints, the two lasers were on one table, and the reference crystals, magnet dewar, and locking beam detectors were on a separate table. Neither table was pneumatically floated, so the results reported here demonstrate the immunity of this locking technique to vibrations. By contrast, most other frequency references require extreme vibration isolation measures to reach this short-term stability.

Evaluation of the frequency stability of a single laser at sub-MHz resolution is difficult if one lacks a frequency standard at the appropriate wavelength for comparison. For that reason, two independent lasers were constructed and locked to two separate SHB crystal references. The frequency stability was determined by beating unmodulated portions of the two stabilized laser beams on a New Focus 1811 photodiode detector, recording the beat frequency measured by a Stanford Research SRS 620 frequency counter, and carrying out subsequent statistical analysis of the time dependence of the beats using a computer. Allan deviations for integration times up to 50 ms were directly measured with the frequency counter, whereas for longer integration times the Allan deviation was calculated from the recorded heterodyne beat frequency data, which was recorded at 50 ms time intervals. All data acquisition programs were written in Labview.

Results and Discussion

The stability over broad time scales is characterized by the Allan deviation [18] of the heterodyne beat frequency as introduced in Chapter 3. Performance of the free

running lasers is shown in Fig. 4.4(a), while that of the lasers locked to regenerative spectral holes using the method of Ref. 12 is shown in Fig. 4.4(b). Short term stabilization giving a 500 Hz Allan deviation for a 2 ms integration time was achieved with the conventional adjustment of the phase sensitive error signal, that is, with the detector signal and local oscillator in phase at the mixer as illustrated by the $\phi = 0^\circ$ signal of Fig 4.3(a). Under these conditions, the dominant contribution to the error signal comes from the spectral hole. Comparison of the curves in Fig. 4.4(a) and Fig. 4.4(b) shows that slow frequency drift (integration times longer than 100 ms) of the stabilized lasers in these early experiments approached that of the unstabilized laser. Much of this drift is attributable to slowly-varying DC voltage offsets in the feedback servo loop arising from residual amplitude modulation at the optical phase modulators and temperature drift in the feedback electronics [12] and modulators. The servo offsets cause the laser to lock off-center to the spectral hole and consequently cause the regenerated spectral hole to drift continuously until the drift in the voltage offset undergoes a change of sign. Further development of the feedback servo system should substantially reduce these slowly varying offsets and thus reduce this long-term drift.

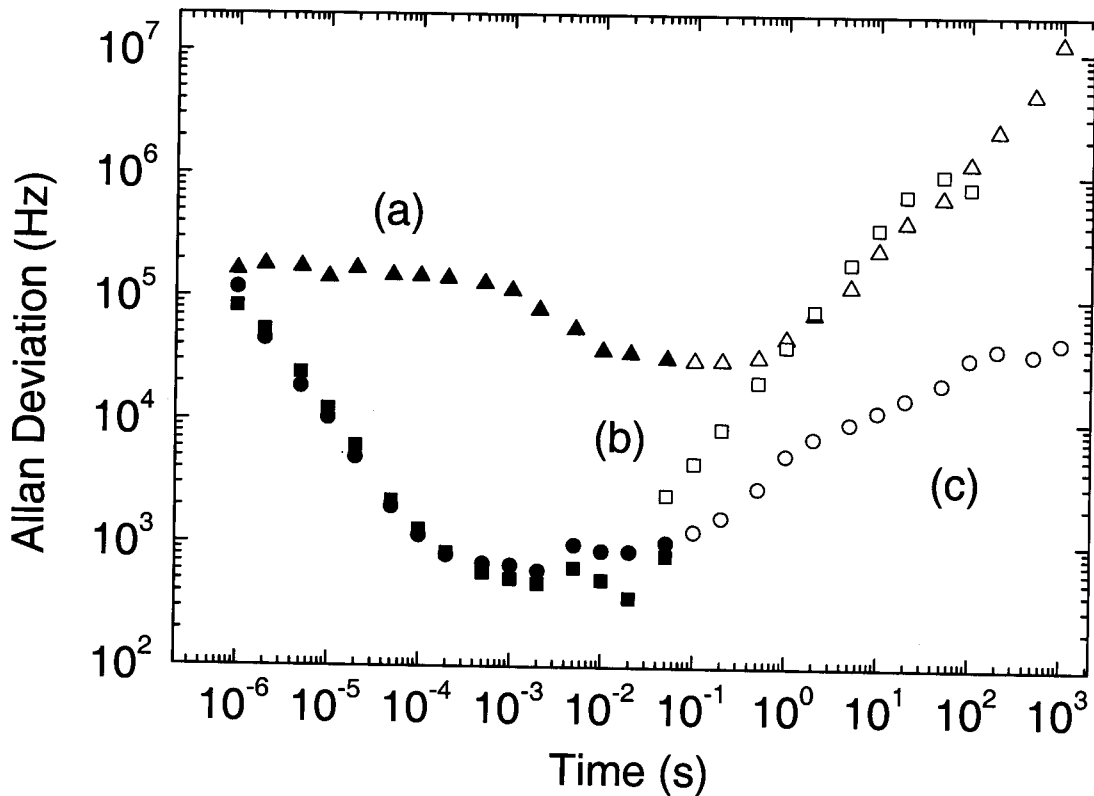


Figure 4.4 Allan deviation values for the beat between two lasers: (a) lasers free-running (triangles), (b) locked to spectral holes in different crystals using straight quadrature detection of the error signal at applied field $B = 0.5$ T (squares), and (c) locked to spectral holes using the strategy of intermediate phase detection of the combined error signal from the spectral hole and inhomogeneous line at applied field $B = 0.2$ T (circles). Filled symbols, 300-sample Allan deviations measured directly by a frequency counter; open symbols, values computed directly from beat frequency data [cf. Fig. 4.5].

Incorporating the Absorption Line as a Fixed Reference

A new locking strategy was devised, however, to reduce drift even with the existing servo system by simultaneously exploiting the high resolution short term frequency reference of the spectral hole and the long term stability of the

significantly broader inhomogeneous absorption line. Figure 4.3(b) illustrates the variation of the error signal as the relative phase between the detector signal and the local oscillator is varied through 90 degrees at the mixer, with the multiple sharp features due to the narrow spectral hole superimposed on the broad background of the inhomogeneous line. The relative position of these two contributions on the frequency axis depends on the arbitrarily chosen position of the spectral hole. Crystal transmission is increased at the frequency of the spectral hole, so the transmission property of the hole and inhomogeneous absorption line have opposite signs. Their pure absorptive and dispersive FM contributions also have opposite signs in simple limiting cases. The shape of the FM signals, however, also depends on the relationship between the modulation frequency ν_m and the width of the relevant spectral feature. There is broad latitude for making this choice, since the hole width $\sim 2\Gamma_h$ can be from 10^5 to 10^8 times narrower than the inhomogeneous line width Γ_{inh} . In the present case, the line widths of the hole contribution and inhomogeneous line contribution lie at opposite extremes relative to the modulation frequency: $\Gamma_h \ll \nu_m \ll \Gamma_{inh}$. The two contributions to the error signal at line center are then strongly phase dependent and are maximized for different quadratures – the dispersive case for the spectral hole and absorptive case for the inhomogeneous profile. These phases are represented as 0° and 90° respectively in Fig. 4.5(b) and correspond to the S2 and S1 phases of Ref. 17. For a phase angle of $\phi = 0^\circ$ the inhomogeneous line signal is negligible and the locking signal is derived primarily from the spectral hole and for a phase angle of $\phi = 90^\circ$ the signal from the

inhomogeneous line is maximized, but the contribution from the spectral hole has vanished at the line center of the hole. By choosing an intermediate phase $0^\circ < \phi < 90^\circ$, both contributions to the error signal contribute to locking stability; a steeply sloped signal from the spectral hole drives the short term stability while at the same time a signal of lower slope from the inhomogeneous line opposes long term drift.

With this procedure, the introduction of a static DC offset in the servo loop leads to an equilibrium lock point where a balance occurs between the sloping contribution from the inhomogeneous line and the DC offset. While not a perfect solution, this is preferable to the original situation where a DC offset caused the locking to be displaced toward one side of the hole and consequently caused a steady drift in hole position and laser frequency as regenerative hole burning took place asymmetrically. Drift in hole position and hence in laser frequency can still occur with the present strategy if the DC offset is slowly varying, but the impacts on stability are reduced. This tendency to settle into an equilibrium position instead of continuing to drift not only improves the long-term frequency stability but also provides a means to choose an arbitrary frequency within the inhomogeneous absorption profile as the stabilization frequency. To adjust the locking frequency, either the DC offset level or the local oscillator phase (and hence the contribution of the inhomogeneous line to the error signal slope) may be adjusted. The system initially drifts towards and then settles at the equilibrium frequency, where the offset cancels the FM signal. This behavior was verified by computer simulation and by direct observation using a

probe laser to monitor the position of the spectral hole and the locked laser within the inhomogeneous line.

The impact of this new hybrid locking strategy on frequency stability is shown in the Allan deviation plot of Fig. 4.4(c). There is no degradation of the short-term stability, and the long-term stability is improved dramatically for integration times of 100 ms to greater than 1000 s, with the improvement exceeding two orders of magnitude at the longer times. Evolution of the heterodyne beat frequency over a period of 30 minutes (1800 s) is shown in Fig. 4.5(a) when both lasers were free running and in Fig. 4.5(b) when both lasers were locked using the new strategy. For integration times of 1 s and longer, the drift has been reduced to about 7 kHz/min over several minutes. For small integration times (solid circles, triangles, and squares of Fig. 4.4), the frequency counter directly measured the Allan deviation values; for long integration times (open circles, triangles, and squares of Fig. 4.4), the Allan deviation was computed from the beat frequency data of Fig. 4.5, acquired at 50 ms intervals. The inherent sub-MHz free-running stability of the lasers is already sufficient for many spectroscopic applications, but an improvement over the free running case of about two orders of magnitude has been accomplished for time scales of 100 μ s - 10 ms and for times longer than one minute. Minimum Allan variances of 200 Hz have been recorded, although the 500 Hz value in Fig. 4.4 is typical for performance at this stage of system development.

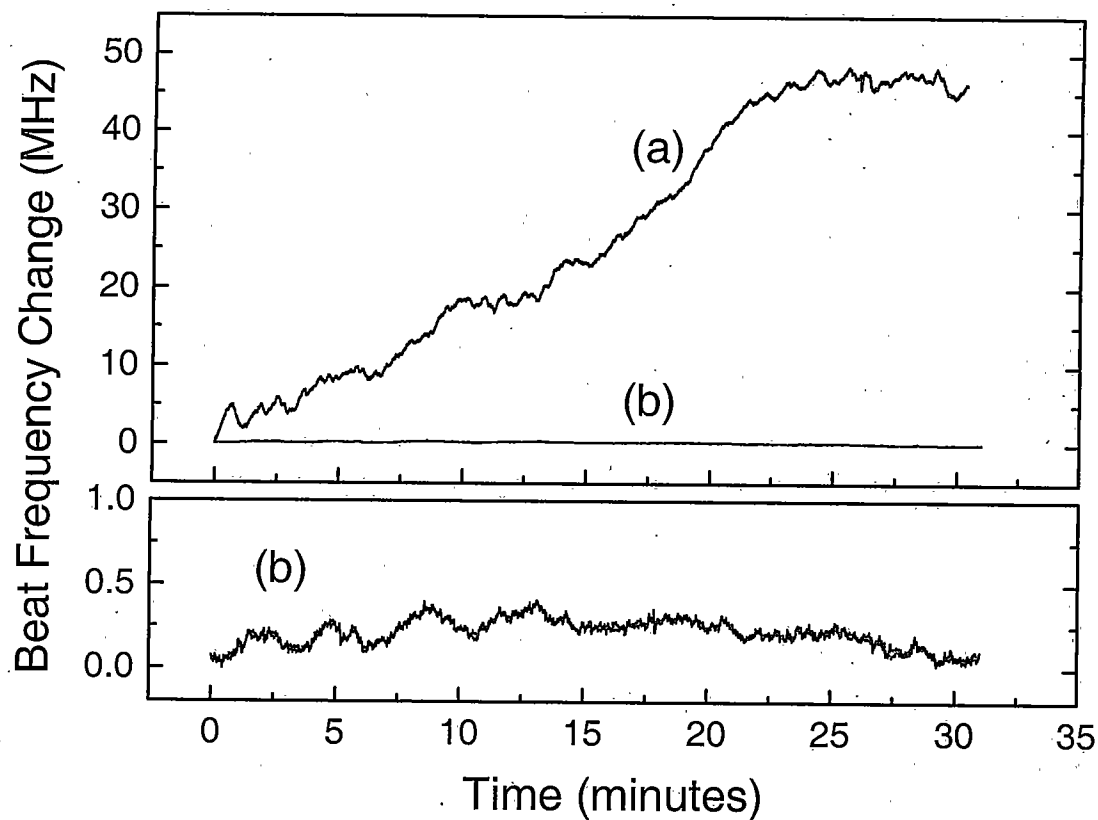


Figure 4.5 Change in heterodyne beat signal between (a) free-running and (b) independently locked lasers to separate spectral holes and inhomogeneous lines in different crystals at field $B = 0.2$ T, the lowest trace is an expanded view.

For somewhat stronger long-term resistance to drift the modulation frequency could be increased to provide a larger inhomogeneous line contribution to the slope at the desired locking frequency; this increases the amplitude of the contribution from the inhomogeneous line with little effect on the contribution from the spectral hole.

The $\text{Er}^{3+}:\text{Y}_2\text{SiO}_5$ homogeneous resonance width in a magnetic field of 0.2 to 0.5 T is narrower [14] than that from the preceding work [12] on $\text{Tm}^{3+}:\text{YAG}$, so it might be expected to provide lower short-term root Allan variance values than $\text{Tm}^{3+}:\text{YAG}$ using the same technique and apparatus. In this case, however, the $4f^{11}$ electron configuration of the Er^{3+} ion leads to strong Er^{3+} magnetic moments, whereas the Tm^{3+} ion with configuration $4f^{10}$ has an electronic singlet ground state with 'quenched' angular momentum and no first order magnetic moment. Electron spin flips of nearby Er^{3+} -ions in the ground state as well as nuclear spin flip-flops by Y^{3+} nuclei lead to fluctuations in the local fields and thus to measurable spectral diffusion [14,19] of the Er^{3+} -ion population that making up the spectral hole frequency reference. The 0.2 to 0.5 T applied magnetic field reduces electron spin flips by reducing thermal population of the upper component of the Er^{3+} Kramers doublet ground state, but it does not eliminate them completely. It also suppresses the far weaker spectral diffusion due to Y^{3+} (or Er^{3+}) nuclear spin flip-flops. Evolution of the spectral hole width by spectral diffusion limits the currently achieved frequency stability of the hole on time scales longer than 2 ms and hence of the locked laser. A detailed study of spectral diffusion in $\text{Er}^{3+}:\text{Y}_2\text{SiO}_5$ is presented in Chapter 5.

Further sources that limit stability are residual amplitude modulation [20] produced by the electro-optic phase modulator and thermally induced drift in the locking circuitry and modulator, all of which introduce variable offsets to the error-signal, causing the laser to lock slightly off the center of the spectral hole. In the

previous implementation [12], this produced unrestrained long-term frequency drift of the spectral hole. With the new method reported here, it results instead in smaller changes to the equilibrium lock point in the inhomogeneous line profile. As noted above, further improvements from passively and actively stabilizing the temperature of the feedback electronics are expected to improve system performance.

Improved Photon Echo Stability for Applications

Time-domain spectroscopy and a wide range of proposed SHB optical devices [3,4,5,6,7,8] are based on the photon echo and stimulated photon echo, the capabilities of these techniques can be improved with the level of frequency stabilization reported here. For optimal exploitation of the stimulated photon echo, laser frequency stability to better than the spectral width of the broadest excitation pulse, or in the limiting case to better than a homogeneous linewidth, is required for the storage time of the material, which is defined by the decay time of a transient spectral hole for the transition being probed. With lasers stabilized to spectral holes, this requirement is naturally and automatically met.

Here we demonstrate this improvement by measuring stimulated photon echoes on the ${}^4I_{15/2}(1) \rightarrow {}^4I_{13/2}(1)$ site (1) transition of $\text{Er}^{3+}:\text{Y}_2\text{SiO}_5$ using a stabilized 1536 nm laser, an Er-doped fiber amplifier, and the echo apparatus to be described in Chapter 5 and in Ref. 12. Approximately 5 mW of unmodulated continuous-wave laser power was available for producing echo excitation pulses after continuous

wave amplification of the laser by the Er-doped fiber amplifier, which was located outside the servo loop for laser stabilization. A portion of the un-amplified laser output was used to frequency-lock the laser to a regenerative transient spectral hole in the same transition as described above. Echo excitation pulses were produced using two acousto-optic modulators in series to improve the on/off contrast ratio and to cancel any net shift in the laser frequency, since the $\text{Er}^{3+}:\text{Y}_2\text{SiO}_5$ spectral lines are narrow. The resulting photon echo signal was gated from the transmitted beam by a third acousto-optic modulator to discriminate against the exciting pulses. The echo was detected with a fast New Focus 1811 InGaAs-photodiode. To generate stimulated photon echoes, three $2 \mu\text{s}$ excitation pulses were incident on the crystal, with the delay t_{12} between the first and second pulses fixed at $19 \mu\text{s}$. The strength of the stimulated echo was measured as a function of the delay t_{23} between the second and third pulses.

With the laser frequency locked to a transient spectral hole, stimulated photon echoes could be measured consistently for t_{23} delay times of several hundreds of microseconds, giving the data in Fig. 4.6(b). The limiting factor for measuring echoes with longer t_{23} delay times was the detector signal-to-noise ratio, rather than laser frequency jitter, even though additional jitter may have been introduced by the Er-doped fiber amplifier. After $800 \mu\text{s}$ total delay time the stimulated echo signal was buried in the noise. In contrast, when the stimulated echo decay was measured with the laser free running, the reproducibility of the stimulated echo became unreliable after only $200 \mu\text{s}$, as shown in Fig. 4.6(a).

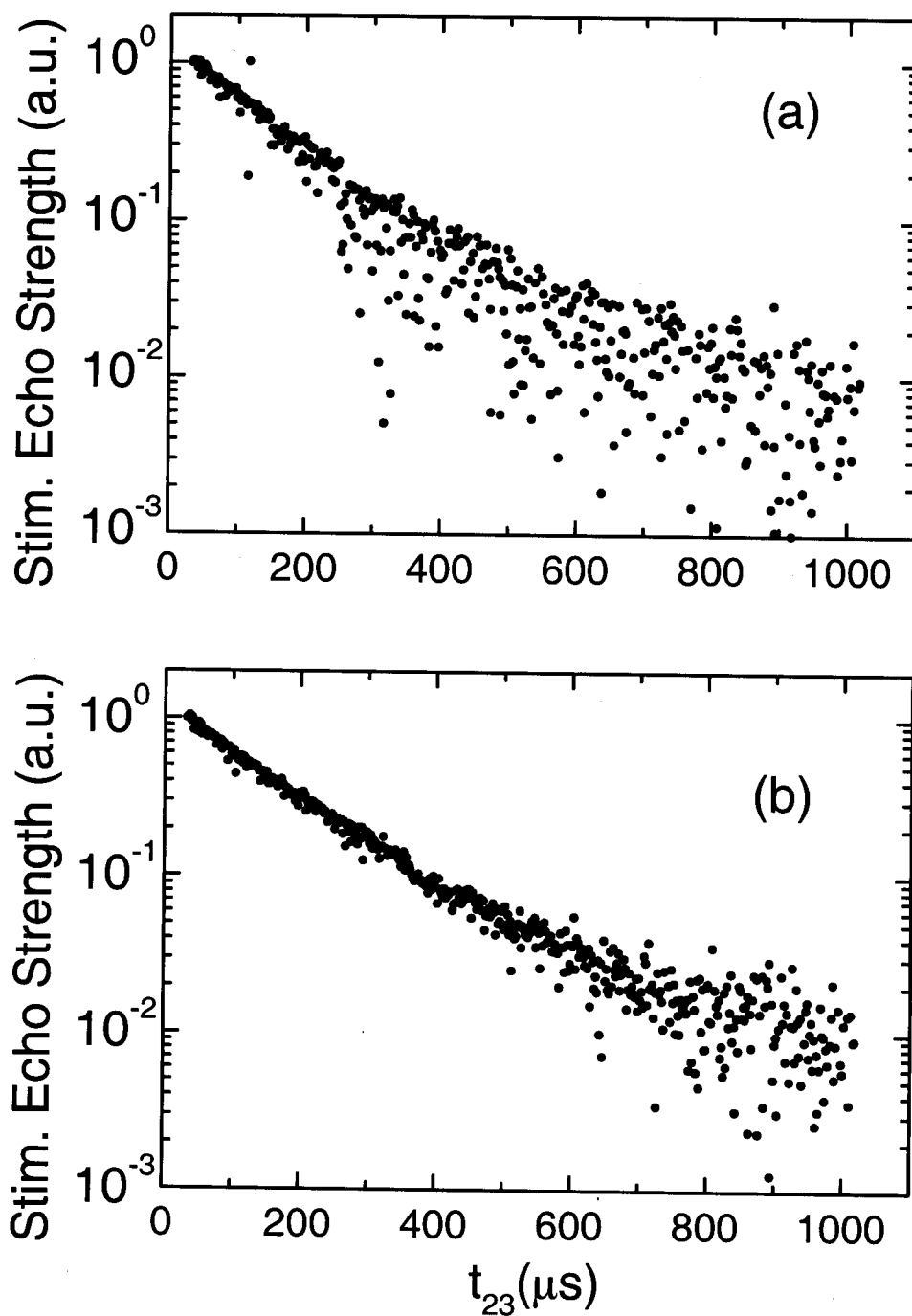


Figure 4.6 Stimulated photon echo decay on the ${}^4I_{15/2}(1) \rightarrow {}^4I_{13/2}(1)$ transition in $\text{Er}^{3+}:\text{Y}_2\text{SiO}_5$. Each point represents a single shot. (a) Measured with a free running laser. (b) Measured with a laser stabilized to a spectral hole and inhomogeneous line at field $B = 0.2$ T.

All the data points of Fig. 4.6 were single-shot acquisitions of the stimulated photon echo without thresholding to reject low-intensity echoes. Figure 4.6(a) demonstrates that frequency jitter was the cause of the echo signal amplitude fluctuations when a free-running laser was used, since occasionally an optimum echo was produced when the laser frequency of the third pulse happened to match that of the first two. An envelope of "good" echoes can be seen, but most points fall well below this. Clearly, averaging the data in Fig. 4.6(a) over multiple shots would lead to a much different and erroneous echo decay rate.

Frequency response of a regenerative spectral hole

Regenerative SHB materials provide a fundamentally different type of frequency reference from Fabry-Perot cavities or isolated atomic references, because the incident laser probe field can modify the spectral hole reference. This is a fundamental difference between ungated SHB frequency references and static traditional frequency references such as the familiar Fabry-Perot cavity or atomic references.

The interplay of the dynamics of materials and the stabilization process has been investigated numerically and experimentally, and these results have been used to optimize the system performance. [21,22] The spectral hole width and hole lifetime are important parameters for the use of spectral hole burning as a means for laser frequency stabilization. The hole width dictates the short-term performance of the system, whereas over longer time scales the hole lifetime is important. When the

hole lifetime is increased for a specific hole width, the memory time of the spectral hole is increased – it remains a valid frequency reference over longer periods.

Regenerative spectral holes are expected to exhibit a different frequency response over the low frequency range up to the spectral hole width compared to static frequency references, such as a Fabry-Perot cavity. This is because regenerative spectral holes will lose their memory for times longer than the hole lifetime leading to a roll off in gain relative to the cavity, which has a flat frequency response.

Methods and Apparatus

Experimentally the frequency response was measured in a two beam experiment by probing a regenerative spectral hole that was burned with a laser stabilized to a spectral hole in the same transition in a different location of the same crystal (Fig. 4.7). To generate a probe beam, part of the stabilized laser beam was split off with a $\lambda/2$ -waveplate and polarizing beam splitter after the EOM, which was operated at 109.5 MHz.

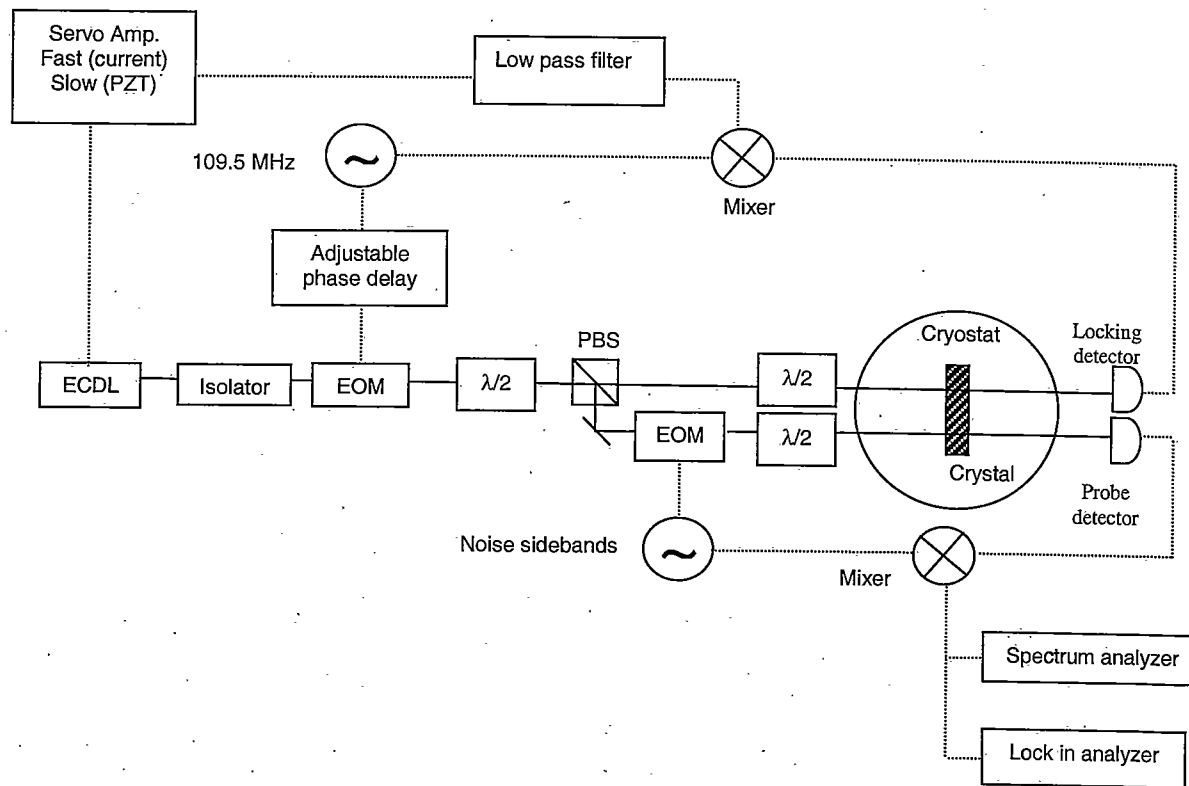


Figure 4.7 Experimental setup used to measure the frequency response of a regenerative spectral hole in $0.001\% \text{Er}^{3+}:\text{Y}_2\text{SiO}_5$.

Both beams were adjusted to have the same spatial profile and optical power of $50 \mu\text{W}$ therefore generating identical error signals by FM spectroscopy. The first beam was used to lock to a regenerative spectral hole. The second beam was used as a probe beam and modulated with a second EOM putting on noise sidebands with a modulation index of $\pi/42$ radians; the optical power in the noise sidebands was estimated at 220 nW per sideband. This second phase modulation was varied in frequency to linearly probe the error signal response over the range of 100 Hz to 1.6 MHz . Both beams went through the same $0.001 \text{ at. percent Er}^{3+}:\text{Y}_2\text{SiO}_5$ crystal (batch #1-544) spatially separated with a beam spot size radius of 1.07 mm otherwise experiencing identical conditions. The crystal was oriented with its b -axis (2 mm) parallel to the lasers' k -vector, and its D_1 -axis (12 mm) parallel to the external magnetic field of $B = 0.3 \text{ T}$. The laser light polarization was adjusted in both beams using a $\lambda / 2$ wave plate to be parallel to the crystals 15 mm long D_2 direction. The crystal was immersed in a liquid Helium bath operated at a temperature of $T = 1.7 \text{ K}$. Generation of the noise EOM drive frequency and capture of the signal at this frequency was accomplished by using two different techniques depending on the frequency range being examined. This was required by the limited frequency ranges of the different instruments. In the range $\text{DC}-300 \text{ kHz}$, the EOM was driven by the Stanford Research Systems DS 345 function generator (24 dBm output into 50Ω , 10 V_{pp} amplitude) and the signal monitored using an EG & G Princeton Applied Research lock-in analyzer Model 5204. In the range $10 \text{ kHz} - 1.6 \text{ MHz}$, the Hewlett Packard spectrum analyzer/-tracking generator E4411 B (0 dBm output) drove the

EOM with amplification provided by a Minicircuits ZHL-6A amplifier. This also yielded a $10 V_{pp}$ amplitude signal at the EOM. The same spectrum analyzer monitored the error signal. Sweeping the phase modulated noise sidebands over the spectral range of interest allowed measurement of the phase-modulation spectrum of the error signal. The frequency response of the error signal was obtained after scaling the phase modulation spectrum by a factor of $2\pi/f$. Since the phase modulation signal goes to zero at DC, the signal to noise ratio imposes a lower limit on the measurable error signal response. The low frequency response of the hole can be inferred beyond this limit by taking the ratio of the spectral noise density measured relative to the regenerative spectral hole and that measured relative to a static reference, in this case, a 150 MHz FWHM inhomogeneous line in isotopically purified $Er^{3+}:LiYF_4$. This assumes that the same noise is present in both measurements. This measurement is the source of the experimental data in Fig. 4.8 at frequencies below 300 Hz. The narrow features in the low frequency error signal response are artifacts of this technique. The feature at ~ 700 kHz can be attributed to a piezo-electric resonance of the EOM.

Discussion

By employing the time domain model, which describes the material in terms of the optical Bloch equations (developed by Dr. G. J. Pryde and C. W. Thiel and to be described in detail elsewhere [22, 23]), it was possible to obtain the frequency dependent response of the error signal, shown as open circles in Fig. 4.8. The

calculated AC-response of a Fabry-Perot cavity [24,25,26] is given by a dashed curve for comparison; it has the shape of a low-pass filter. The cavity transmission band of half width at half maximum (HWHM) ~ 16 kHz for this calculation was chosen to have the same width as that of the spectral hole. Over the range of the measurement, the model and experiment agree, and they are both in coincidence with the response of the Fabry-Perot cavity.

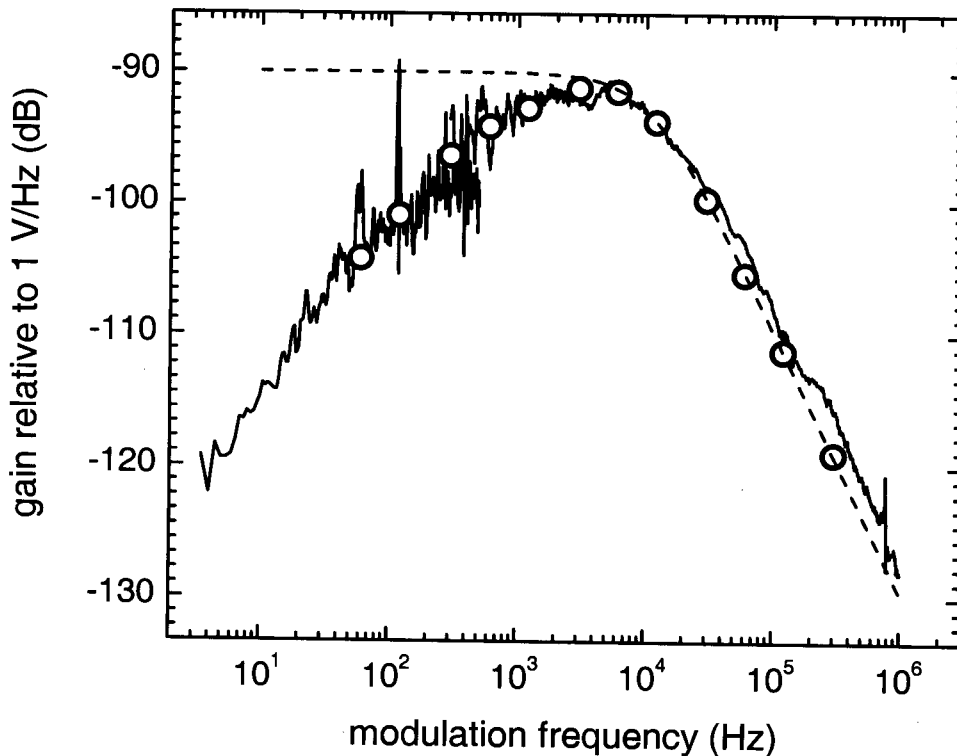


Figure 4.8 Frequency response of the error signal generated from a regenerative spectral hole frequency reference in 0.001 % $\text{Er}^{3+}:\text{Y}_2\text{SiO}_5$; experimental measurement (solid line) and using the model (open circles), compared with the calculated response of a Fabry-Perot cavity (dotted line) of the same linewidth.

It is clear that the high frequency roll off is close to 20 dB / decade, which is ideal for servo design since the accumulated phase shift from the reference is limited to 90°. At lower frequencies, the predicted roll-off of the gain is observed; consistent with the idea that the system is losing its memory as a frequency reference because of the limited hole lifetime. In principle, servo gain can partially compensate the low frequency roll-off [27], but not low-frequency noise on the reference itself. Passive reduction of this noise becomes essential for good long-term performance of regenerative spectral hole burning references with short hole lifetimes. Of course, linear drift can be removed after the fact, as with lasers stabilized to traditional references [28]. A new technique has been devised that incorporates the inhomogeneous absorption line itself as a fixed reference, dramatically improving the long-term stability. However, this technique is only applicable to materials with narrow ≤ 1 GHz wide inhomogeneous absorption lines.

Laser frequency stabilization to regenerative spectral holes in Er^{3+} :KTP

Potassium titanyl phosphate, KTiOPO_4 (KTP), is an important nonlinear electro-optic material primarily used as a frequency doubling crystal and for optical waveguides. Here we report the achievement of 200 Hz laser stabilization utilizing Er^{3+} :KTP with an Er^{3+} concentration of 0.004 at. percent as a spectral hole burning frequency reference.

Methods and Apparatus

The $\text{Er}^{3+}:\text{KTP}$ crystal was kindly provided by Roger C. C. Ward of the Clarendon Laboratory, University of Oxford, England. It was oriented with its a-axis parallel to an external magnetic field and its b-axis parallel to the laser \mathbf{k} -vector. The lowest energy ${}^4\text{I}_{15/2} \rightarrow {}^4\text{I}_{13/2}$ Er^{3+} transition has been observed to exhibit six distinct sites near 1537 nm. [29] The site with the strongest absorption, located at 1536.87 nm (6506.69 cm^{-1}), exhibits transient spectral hole burning by population storage in the excited state of the optically active Er^{3+} ion; laser stabilization experiments were performed using the absorption transition between the lowest Zeeman split levels. Fig. 4.9(a) shows the transmission through the ~ 2 GHz (FWHM) wide inhomogeneously broadened line for a magnetic field of $B = 0.25$ T and temperature $T = 1.9$ K. The origin of the shoulder appearing at higher frequency is most likely due to absorption from a spectrally similar site, as indicated by fluorescence decay experiments. A narrow spectral hole, indicated by an arrow, has been prepared by a second laser and can be placed anywhere within the inhomogeneously broadened line. The homogeneous linewidth has been characterized using two pulse photon echoes measured as a function of delay time between the two excitation pulses. The measured dephasing time corresponds to a homogenous linewidth of 2 - 3 kHz for small magnetic fields below $B = 0.4$ T.

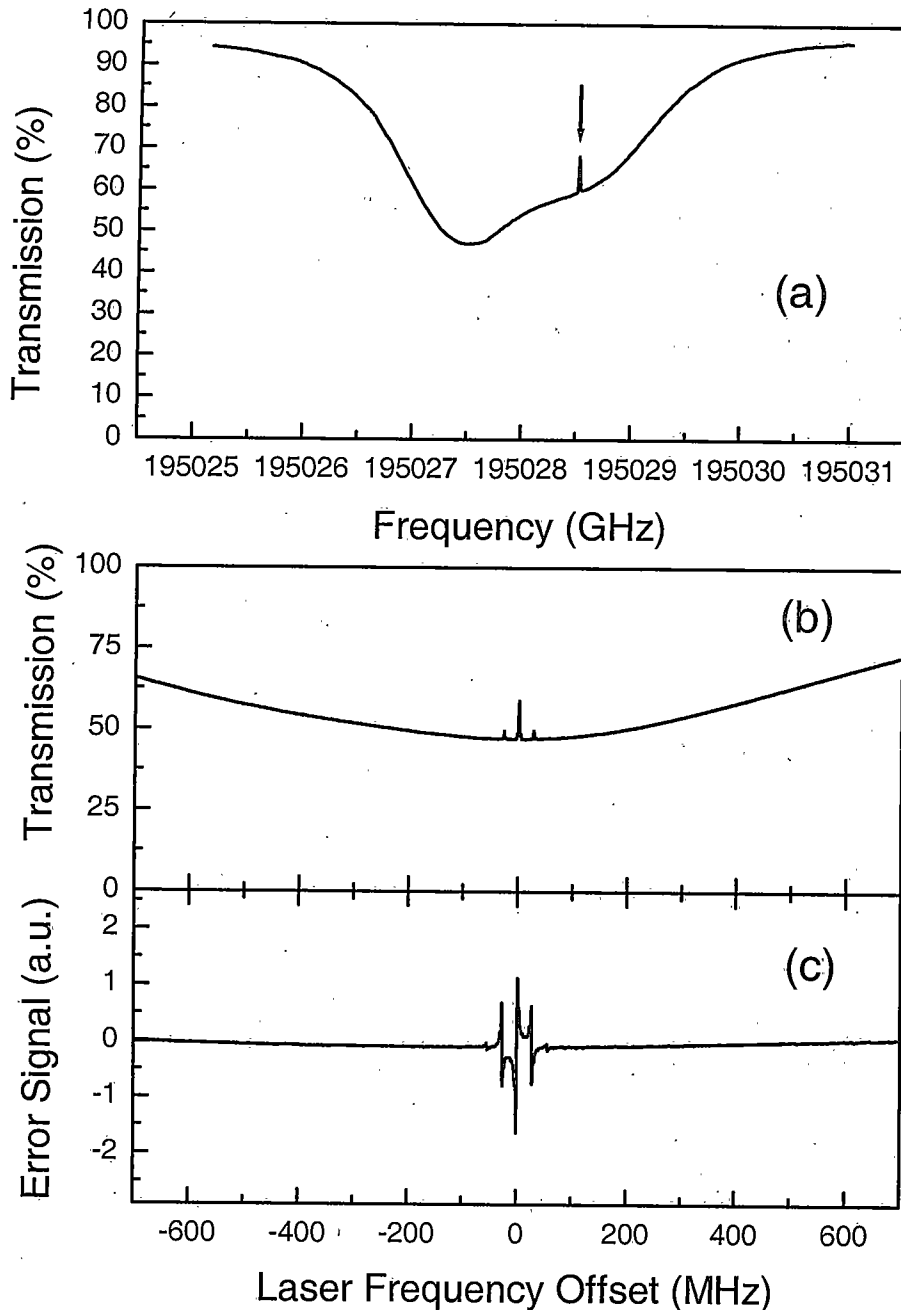


Figure 4.9 (a) Transmission spectrum of 0.004 % $\text{Er}^{3+}:\text{KTP}$ at 1537 nm showing the entire inhomogeneously broadened ${}^4\text{I}_{15/2} \rightarrow {}^4\text{I}_{13/2}$ optical absorption scanned by a diode probe laser. The arrow indicates a spectral hole, which has been burned by a second laser. (b) Transmission of a phase-modulated probe laser through a single spectral hole created by a second laser, using an applied magnetic field of $B=0.25\text{T}$. (c) Demodulated FM-error signal derived from the spectral hole in (b).

The experimental setup and techniques are similar to the previous demonstration using $\text{Er}^{3+}:\text{Y}_2\text{SiO}_5$. The lasers were modulated with modulation index $M \sim 0.4$ at 27 MHz and 30 MHz, respectively, values greatly exceeding the spectral hole width. Fig. 4.9(b) shows the transmission through a spectral hole burned by a second laser and Fig. 4.9(c) the corresponding demodulated FM error signal probed with a phase-modulated laser; detector signal and local oscillator are in phase. To obtain a good signal to noise ratio in the detection under low laser locking irradiance, it is beneficial to choose a large frequency reference crystal. Crystal dimensions were 12.87 mm along a , 14.89 mm along c , with a 5.18 mm optical path along b ; both lasers were locked to the same crystal. To avoid spatial overlap or interaction of the two independently locked laser beams, a mask with separated 4 mm apertures was placed over the crystal. A small magnetic field of $B \sim 0.25$ T has been conveniently applied by sandwiching the sample holder between two permanent Nd-Fe-B magnet disks of diameter 5 cm greatly simplifying the experimental apparatus. The mounted crystal was immersed in liquid helium at $T = 1.9$ K. The entire two-laser optical setup, including the cryostat, fit on a 3' by 4' optical breadboard, which was placed on vibration damping foam on a commercially available pneumatically floated optical table. An acoustical isolation enclosure box [30] made of medium density fiberboard lined with $\frac{3}{4}$ " thick polyester embossed sound control mat covered the experiment to provide passive acoustical isolation from ambient acoustic noise.

The laser irradiance of $\sim 100 \mu\text{W}/\text{cm}^2$ at the crystal was split from the laser beam using a $\lambda/2$ -plate / prism-polarizer combination, leaving most of the laser output

power to be used for experiments requiring a stabilized source or to saturate an Erbium doped fiber amplifier for higher power applications. Using higher irradiance at the locking crystal leads to a deeper spectral hole, which in turn becomes broader due to stronger material absorption in the wings of the hole than at the hole center. During active stabilization, each laser burns a spatially and spectrally separated transient spectral hole into the inhomogeneously broadened absorption profile. Error signal feedback to each laser leads to a continuous regeneration of the transient spectral hole until a balance between spontaneous hole relaxation and hole burning occurs.

The relative frequency stability of the two stabilized lasers was characterized by the statistical Allan deviation [18] of the optical beat frequency since no absolute frequency reference was available.

Results and Discussion

The Allan deviation for (a) the free running lasers and (b) actively stabilized lasers is shown in Fig. 4.10. With the laser locked to transient spectral holes in Er^{3+} :KTP an improvement in the Allan deviation over the free running lasers to 250 Hz has been achieved for integration times between 1 ms and 100 ms, demonstrating the potential of Er^{3+} :KTP at the current stage of system development. During quiet periods, Allan deviations of 200 Hz at 10 ms integration time have been measured. The structure of the Allan deviation curve is reproducible.

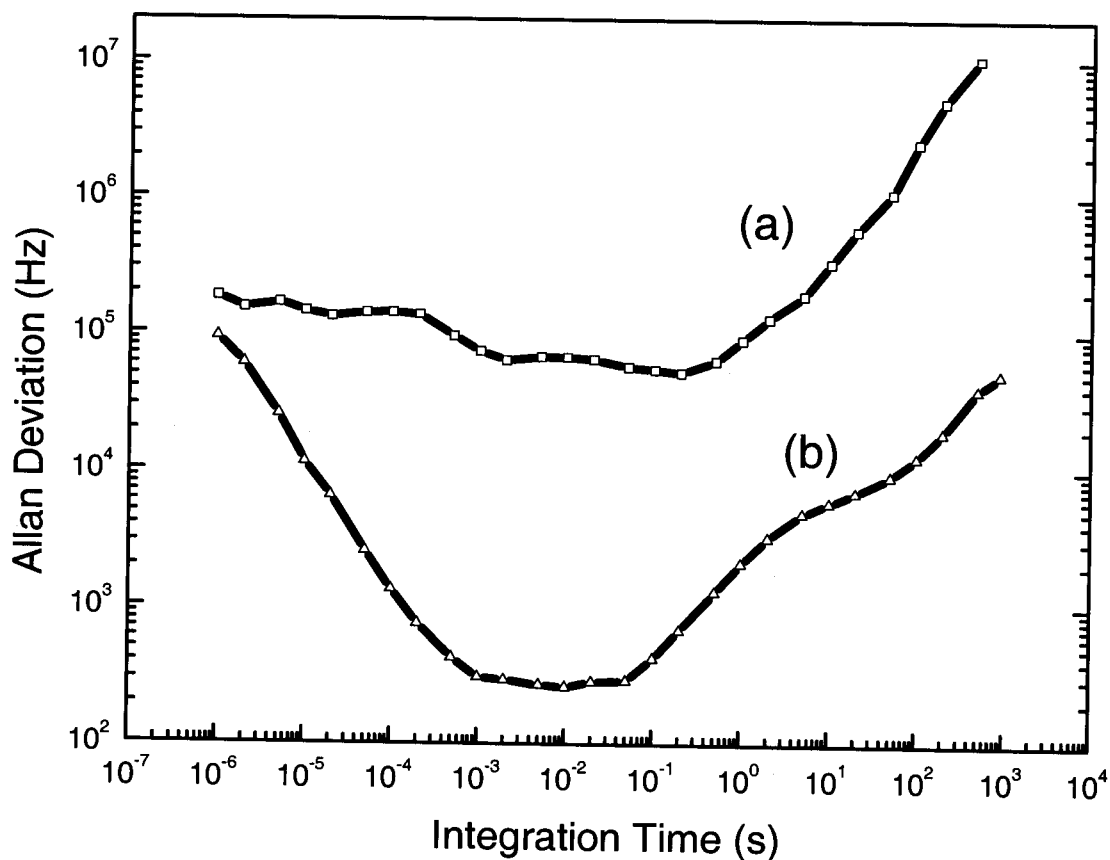


Figure 4.10 Allan deviation for the heterodyne beat frequency between two lasers: (a) lasers free-running, (b) independently locked to transient spectral holes in the ${}^4I_{15/2} \rightarrow {}^4I_{13/2}$ transition in $\text{Er}^{3+}:\text{KTP}$ at 1537 nm.

Long-term drift of the laser, evidenced by an upturn of the Allan deviation at longer integration times, has been greatly reduced by choosing an intermediate phase setting at the mixer between detector signal and local oscillator. This technique combines the excellent short-term stability of the spectral hole with the good long-term stability of the inhomogeneous line as described above; long-term drift of the beat frequency between the two lasers has been suppressed to ~ 10 kHz per minute. The demonstrated short-term stability is showing a clear improvement to the

previously reported results using transient spectral holes in $\text{Er}^{3+}:\text{Y}_2\text{SiO}_5$ and is the best result achieved in Er^{3+} -doped compounds. As in the case of $\text{Er}^{3+}:\text{Y}_2\text{SiO}_5$, spectral diffusion plays a major role in the achieved performance.[13,19] Even though the transient spectral hole provides a narrow \sim kHz reference, the narrow hole width could not be fully exploited over longer periods because of the T_1 -limited hole lifetime. In addition, the strong Er^{3+} ion magnetic moments in the ground state are perturbed by local field fluctuations due to electron spin flip-flops between nearby Er^{3+} ions in the ground state. These perturbations lead to a broadening of the homogeneous linewidth over time. The small magnetic field of $B = 0.25$ T applied slows this spectral diffusion process by thermally depopulating the upper Zeeman component of the Er^{3+} -ion ground state but does not eliminate it completely.

Technical limitations are similar to the ones described above for $\text{Er}^{3+}:\text{Y}_2\text{SiO}_5$. Environmental disturbances due to vibration and acoustical noise sources have been partially addressed by floating the optical table and covering the experiment by the acoustical enclosure described in the section: Methods and Apparatus; improvements to the servo system and laser diode drivers have been made as well. Performance without these modifications is indicated by the minimum 500 Hz Allan deviation observed for $\text{Er}^{3+}:\text{Y}_2\text{SiO}_5$ in Fig. 4.4. [19]

Conclusions

The concept of laser frequency stabilization using regenerative transient spectral hole burning has been extended to the technologically important 1.5 μm wavelength region. Stable laser sources based on this method improve both spectroscopic capability and the performance of SHB devices such as all-optical network routers and address header decoders. Moreover, by stabilizing the laser source to the same SHB material that is already employed in the SHB device, system complexity is significantly reduced. A hybrid method to control long-term frequency drift has been demonstrated, using an intermediate phase delay in the phase sensitive detection of the frequency locking error signal that exploits contributions from the narrow spectral hole and from the inhomogeneous absorption profile. This stabilization method is particularly well suited for spectroscopy and for optical data processing devices based on time-domain spectral hole burning. Substantial improvement in stimulated photon-echo reproducibility was demonstrated, showing the impact of this technique on spectroscopy of rare earth materials.

As materials having gated persistent spectral holes with very long lifetimes are developed, [31] the locking techniques reported here for regenerative SHB can be applied to produce sources with long term stability and perhaps provide highly portable secondary frequency standards.

Laser frequency stabilization to persistent spectral holes in $\text{Er}^{3+}:\text{D}:\text{CaF}_2$

Here we report stabilization of external cavity diode lasers to persistent spectral holes at 1523 nm in $\text{Er}^{3+}:\text{D}:\text{CaF}_2$ which we believe is the first demonstration of a programmable frequency reference in the important 1.5 μm telecommunication band based on persistent spectral holes. The results presented here extend the excellent performance of spectral hole stabilized lasers to integration times of tens to hundreds of seconds as indicated by a 5.7 kHz Allan deviation over 1600 s integration time, opening up new regimes for spectroscopy and interferometry applications. Persistent spectral holes in $\text{Er}^{3+}:\text{D}:\text{CaF}_2$ are qualitatively different from persistent spectral holes found in other materials due to their extremely long lifetime; no measurable degradation of the persistent holes in $\text{Er}^{3+}:\text{D}:\text{CaF}_2$ has been detected over 48 hours in the absence of continuous laser radiation, which suggests that the lifetime could be indefinitely long. A reference frequency programmed as a persistent spectral hole in $\text{Er}^{3+}:\text{D}:\text{CaF}_2$ could potentially be used as a long-term secondary frequency standard in a scheme where a flywheel oscillator infrequently probes the persistent spectral hole to maintain its long-term stability.

Methods and Apparatus

$\text{Er}^{3+}:\text{D}:\text{CaF}_2$, to our knowledge, is the only material known to exhibit persistent spectral hole burning [32] in the spectral region at 1.5 μm . The crystals used in these

experiments have a 0.05 atomic percent Er^{3+} concentration and were prepared by Glynn D. Jones at the University of Canterbury, Christchurch, New Zealand. The introduction of deuterium (D^-) ions into Er^{3+} doped CaF_2 crystals leads to a substitution for F^- ions on interstitial or lattice sites in the vicinity of the Er^{3+} centers, giving rise to additional absorption lines. Among these, the R center, one of the strongest multiple D^- -ion centers, has been shown to exhibit persistent hole burning on the ${}^4\text{I}_{15/2} \rightarrow {}^4\text{I}_{13/2}$ Er^{3+} transition located at 1523 nm and is used here for this laser frequency stabilization demonstration. [32] The spectral hole burning mechanism is known to involve excited D^- ion migration into nearby interstitial sites [33]. Spectral holes of ~ 40 MHz (FWHM) have been measured to be fully persistent for at least forty-eight hours. That together with the high activation energy of the hole burning process implies that the hole lifetime could be indefinitely long if the sample is held at liquid helium temperature. Thermal cycling of the material leads to a full recovery of the original hole shape depending on the temperature reached and time held; shallow holes burned at 1.7 K were largely recovered after thermal cycling up to 70 K for 10 minutes. These properties make $\text{Er}^{3+}:\text{D}^-:\text{CaF}_2$ an interesting candidate for a secondary programmable transportable frequency reference since the absorption profile can be modified in a controlled way. For instance laser beat frequencies or information can be recorded in the crystal with arbitrary frequency separations in the form of persistent spectral holes burned anywhere within the absorption profile and read out at a later time or location as long as the sample temperature and pressure is maintained. Fig. 4.11 (a) shows a transmission spectrum

of $\text{Er}^{3+}:\text{D}:\text{CaF}_2$ and illustrates a number of spectral holes that have been stored into the inhomogeneous absorption line of the R center. The use of this material as a frequency reference is feasible up to a temperature of 30 K where the hole width reaches 320 MHz (FWHM). Commercial closed-cycle cryocoolers can readily cool below 10 K, supporting the practical operation of materials like $\text{Er}^{3+}:\text{D}:\text{CaF}_2$ without cryogenic fluids.

It should also be pointed out that the R-site hole burning mechanism is a property of the host, rather than being dopant-specific, providing greater wavelength versatility by replacing the Er^{3+} ions with other suitable rare earth ions, such as Tm^{3+} , Pr^{3+} [33].

Laser frequency stabilization was implemented as described above. The lasers were externally modulated with electro-optic phase modulators. Custom-built resonant tanks were constructed by the author (see Appendix A), which allowed tailoring the modulation frequency and modulation index to the specific material parameters. The primary sidebands chosen had a modulation index of $M = 0.4$, and the modulation frequencies of 93 MHz and 109.5 MHz for the two lasers were chosen to lie outside the ~ 40 MHz FWHM of the spectral holes used as frequency references. Fig. 4.11(b) shows a transmission spectrum through a single spectral hole burned into the R absorption line and the corresponding demodulated FM error signal (Fig. 4.11(c)).

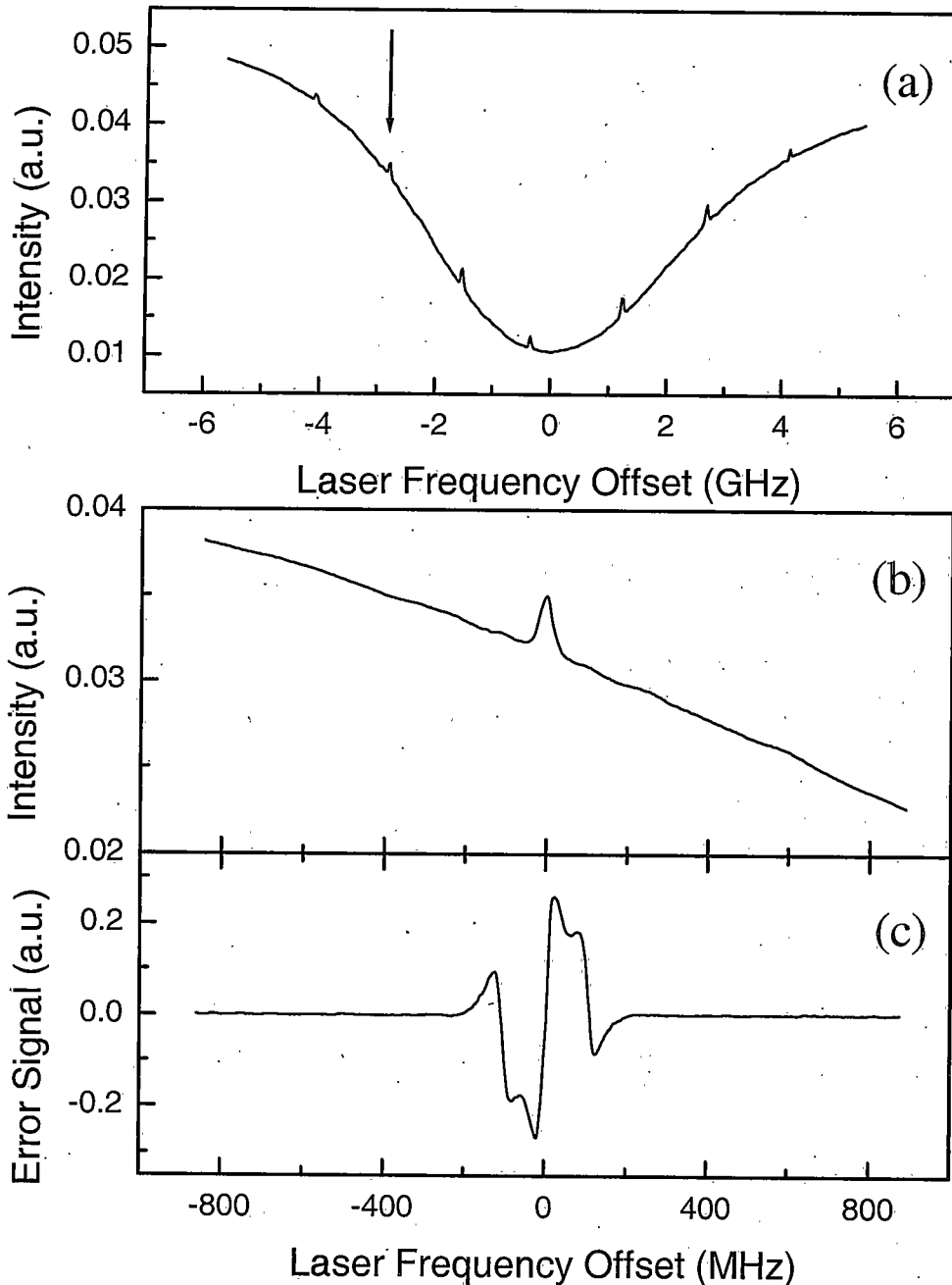


Figure 4.11 (a) Transmission spectrum of $\text{Er}^{3+}:\text{D}:\text{CaF}_2$ at 1523 nm. A number of spectral holes have been burned into the inhomogeneously broadened $^4\text{I}_{15/2} \rightarrow ^4\text{I}_{13/2}$ optical absorption for demonstrating the programmability of the material. Spectral hole burning is not limited to the center of the line. The arrow indicates a spectral hole, which is enlarged in (b). (c) Demodulated FM-error signal derived from the spectral hole in (b).

To demonstrate high performance under simple conditions, the entire setup was implemented on a 3' by 4' tabletop breadboard placed on an unfloated optical table without any acoustical isolation.

The two lasers were independently stabilized to spectral holes in separate reference crystals; each crystal was masked to avoid any coupling by stray light from the other beam and was immersed in a single liquid Helium Oxford Optistat bath cryostat held at $T = 1.9$ K.

Since width and depth of the programmed persistent spectral hole determine the slope of the error signal for active laser frequency stabilization, careful preparation of the initial persistent spectral hole is important. An increase in hole width as a function of burn time was observed due to hole burning centers having only a partial frequency overlap of their homogeneous linewidth with the laser, which leads to a lower effective transition probability and therefore hole burning on a longer time scale. [34] Also, the hole depth increases and eventually saturates as a function of burn time due to the finite number of centers at the laser frequency; as the persistent spectral hole burns deeper its width increases due to earlier saturation in the center than in the wings of the hole.

A tradeoff between hole depth and hole width has to be made in preparing the initial persistent spectral hole. Good results were achieved in using persistent spectral holes of FWHM ~ 40 MHz, prepared by illuminating the sample for 20 seconds with incident light intensities of $\sim 300 \mu\text{W}/\text{cm}^2$. Since the short-term laser linewidth of the free running laser is much less than the narrowest spectral hole

width in this material no active stabilization was engaged in preparing the initial spectral hole. The laser irradiance was controlled using a polarizing beam splitter/half-waveplate combination.

The persistent spectral hole in each crystal was recorded at a similar frequency to allow the beat frequency between the two lasers to lie well within the 125 MHz bandwidth of the beat signal detector; otherwise the beat frequency can be chosen arbitrarily by the relative frequency between the two spectral holes. Laser irradiance enters into the locking stability in two opposing ways. High irradiance leads to good signal to noise ratios on the locking detectors but modifies the spectral hole shapes through continued hole burning; this degrades the reference by making the holes broader and deeper especially when the locking is inadvertently off center relative to the hole. To alleviate this trade off, large samples (~ 9 mm diameter) were chosen, allowing the use of a 4.8 mm beam diameter to preserve the signal to noise ratio needed for the servo feedback loop and to minimize continuous modification of the spectral hole. For active stabilization, the laser illumination was reduced by one order of magnitude to $\sim 30 \mu\text{W}/\text{cm}^2$ to minimize hole burning during locking. The laser frequency stability was characterized as described before.

Results and Discussion

Results for the achieved laser frequency stability are shown in Fig 4.12, with the Allan deviation for the beat between (a) the free running lasers contrasted (b) with that for the spectral hole stabilized lasers. The free running lasers show frequency

stability comparable or even better than similar commercially available systems and are already sufficient for many applications in spectroscopy. With the laser locked to ~ 40 MHz (FWHM) wide persistent spectral holes, an improvement in the Allan deviation over the free running lasers of at least one order of magnitude has been achieved for integration times longer than 2 ms; for integration times longer than 300 s the improvement reaches more than three orders of magnitude.

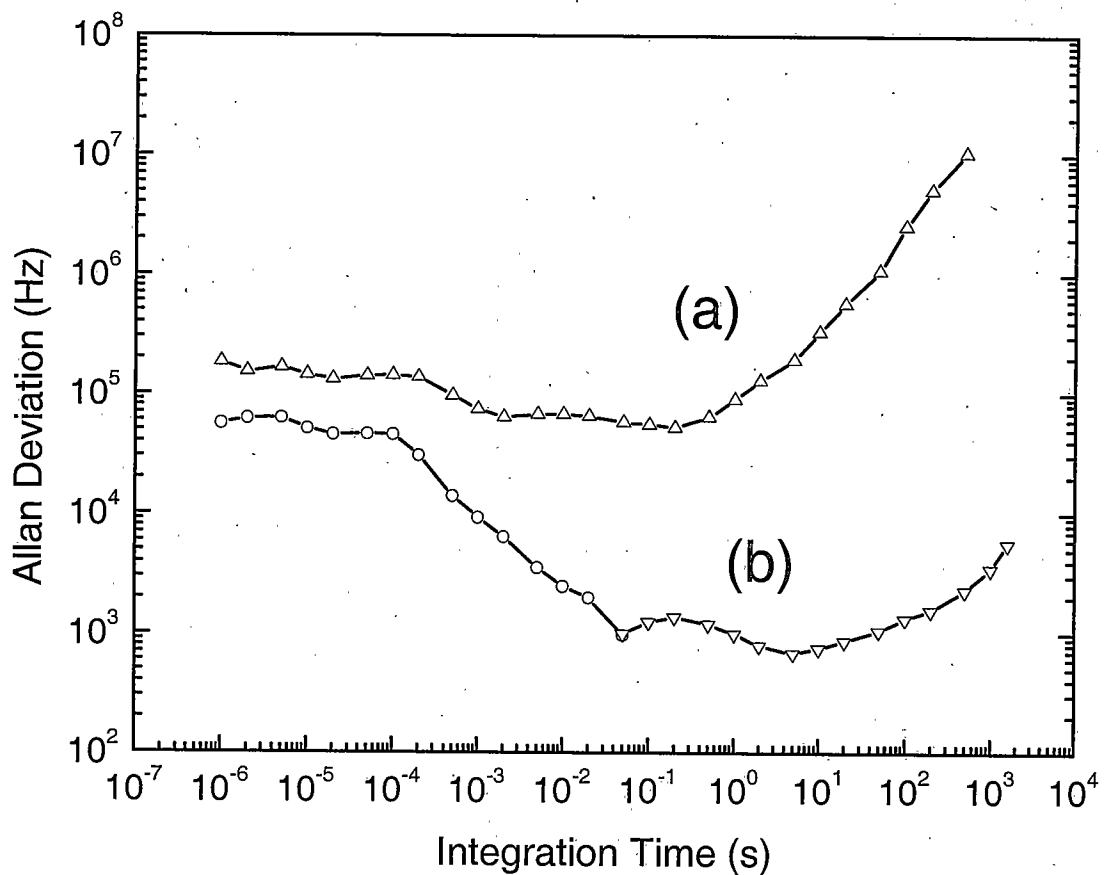


Figure 4.12. Allan deviation for the heterodyne beat frequency between two lasers: (a) lasers free-running, (b) independently locked to persistent spectral holes in the ${}^4I_{15/2} \rightarrow {}^4I_{13/2}$ transition in $\text{Er}^{3+}:\text{D}:\text{CaF}_2$ at 1523 nm

Sub-kilohertz Allan deviations down to 680 Hz have readily been reproduced over a wide range of integration times without requiring vibration isolation of the laser or the crystal frequency reference. This demonstrates laser frequency stabilization to a persistent spectral hole to better than 6 parts in 10^5 of the ~ 40 MHz hole width or better than 3 parts in 10^{12} of the optical frequency. The measured Allan deviation curve is reproducible.

Characterization and optimization of spectral hole burning references by experiment and simulation [21,22] show that the Allan deviation over short integration times is determined by the width of the spectral hole leading to a high signal to noise ratio and consequently good short-term stability, whereas stabilization over long integration times is determined by the lifetime of the spectral hole. The $\text{Er}^{3+}:\text{D}:\text{CaF}_2$ material used for this demonstration is not ideal, since the width of the spectral holes (~ 40 MHz) is much wider than found in many other rare earth doped material systems and is therefore limiting the short-term stability. The long lifetime of the persistent $\text{Er}^{3+}:\text{D}:\text{CaF}_2$ spectral holes leads, however, to a good long-term stability demonstrated in Fig. 4.13, where a subset of the beat frequency change over 10 minutes between the (a) free running and (b) actively stabilized lasers is shown. Laser frequency drift has been reduced to less than 1 kHz per minute. The achieved stability demonstrates the relative immunity of the spectral hole frequency reference to environmental disturbances like vibrations and acoustical noise.

It should be noted that the initial spectral hole becomes broader and burns deeper over time during continued laser locking illumination. This results in a reduced

precision of the frequency reference over long stabilization times. To overcome this problem a hybrid locking technique could be considered where the short-term stability is given by a flywheel oscillator, stabilized to a regenerated transient spectral hole or Fabry-Perot, and long term drift is controlled by comparing its frequency to the frequency of the programmed spectral hole.

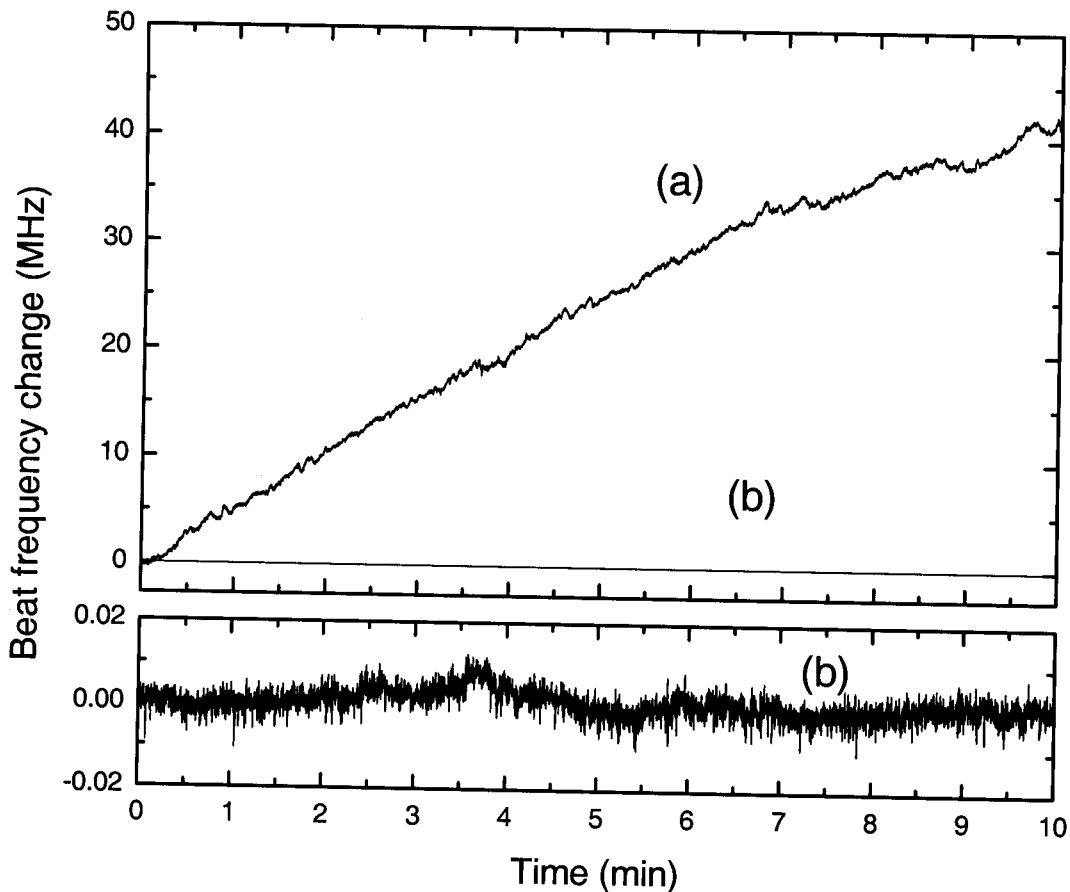


Figure 4.13 Subset of the change in heterodyne beat frequency between (a) free running and (b) independently locked lasers to persistent spectral holes in separate crystals over a period of 10 minutes; the lowest trace is an expanded view.

Technical limitations in our demonstrated laser frequency stability are similar to the ones described in the case of $\text{Er}^{3+}:\text{Y}_2\text{SiO}_5$ locking. Already significant improvements over longer time scales have been made since locking to persistent spectral holes in a similar material, $\text{Tm}^{3+}:\text{D}^{-1}:\text{CaF}_2$. [11] has been reported.

Conclusion

In conclusion, we have extended the use and performance of *persistent* spectral holes as programmable laser frequency references to the important 1.5 μm optical communication window, achieving sub-kilohertz laser frequency stability over broad time scales. A compact laser frequency stabilization that utilizes rather inexpensive, low maintenance external cavity diode lasers has been demonstrated. The system is not limited to low optical power applications, since Erbium doped fiber amplifiers or injection locked high power laser diodes can be used to boost the output power. Other sources like DFB-lasers can be stabilized using this technique.

Suitable spectral hole burning materials for laser frequency stabilization and spectral hole burning based optical processing are under constant development spanning a wide wavelength range, facilitating the stabilization of other sources and proving the versatility of the technique. Materials combining very narrow few-hundred-Hertz-wide holes [35] with long lifetimes of several weeks and minimal spectral diffusion will provide good stability over a wide range of integration times.

Permanent hole burning references with gated spectral holes under development will provide portable compact secondary frequency standards.

REFERENCES

1. R. J. Jones, J.-C. Diehls, J. Jasapara, and W. Rudolf, *Opt. Comm.* **175**, 409 (2000); S. A. Diddams, D. J. Jones, J. Ye, S. T. Cundiff, J. L. Hall, J. K. Ranka, R. S. Windeler, R. Holzwarth, T. Udem, and T. W. Hänsch, *Phys. Rev. Lett.* **84**, 5102 (2000).
2. N. W. Carlson, L. J. Rothberg, A. G. Yodh, W. R. Babbitt, and T. W. Mossberg, *Opt. Lett.* **8**, 483 (1983); M. Zhu, W. R. Babbitt, and C. M. Jefferson, *Opt. Lett.* **20**, 2514 (1995); K. D. Merkel and W. R. Babbitt, *Opt. Lett.* **24**, 172 (1999).
3. T. R. Dyke, M. J. Sellars, G. J. Pryde, N. B. Manson, U. Elman, and S. Kröll, *J. Opt. Sci. Am. B* **16**, 805 (1999); G. J. Pryde, M. J. Sellars, and N. B. Manson, *Phys. Rev. Lett.* **84**, 1152 (2000); M. J. Sellars, G. J. Pryde, N. B. Manson, and E. R. Krausz, *J. Lumin.* **87**, 833 (2000).
4. T. L. Harris, Y. Sun, W. R. Babbitt, R. L. Cone, J. A. Ritcey, and R. W. Equall, *Opt. Lett.* **25**, 85 (2000).
5. K. D. Merkel, R. W. Peters, P. B. Sellin, K. S. Repasky, and W. R. Babbitt, *Opt. Lett.* **25**, 1627 (2000).
6. X. A. Shen and R. Kachru, *Opt. Lett.* **20**, 2508 (1995); T. Wang, H. Lin, and T. W. Mossberg, *Opt. Lett.* **20**, 2541 (1995).
7. T. L. Harris, Y. Sun, R. L. Cone, R. M. Macfarlane, and R. W. Equall, *Opt. Lett.* **23**, 636 (1998).
8. R. G. DeVoe and R. G. Brewer, *Phys. Rev. Lett.* **50**, 1269 (1983); R. M. Macfarlane and R. M. Shelby in *Spectroscopy of Crystals Containing Rare-Earth Ions*, edited by A. A. Kaplyanskii and R. M. Macfarlane (North-Holland,

- Amsterdam, 1987); M. J. Sellars, R. S. Meltzer, P. T. H. Fisk, and N. B. Manson, *J. Opt. Soc. Am. B* **11**, 1468 (1994).
9. T. W. Mossberg, *Opt. Lett.* **7**, 77 (1982); A. Rebane, R. Kaarli, P. Saari, A. Anijalg, and K. Timpmann, *Opt. Commun.* **47**, 173 (1983); M. Mitsunaga, R. Yano, and N. Uesugi, *Opt. Lett.* **16**, 1890 (1991); M. Mitsunaga, N. Uesugi, H. Sasaki, and K. Karaki, *Opt. Lett.* **19**, 752 (1994); H. Lin, T. Wang, and T. W. Mossberg, *Opt. Lett.* **20**, 1658 (1995).
 10. Z. Cole, T. Böttger, R. Krishna Mohan, R. Reibel, W. R. Babbitt, R. L. Cone, and K. D. Merkel to be published. Accepted for presentation at Conference of Lasers and Electro Optics (CLEO), Long Beach, CA, May 2002.
 11. P. B. Sellin, N. M. Strickland, J. L. Carlsten, and R. L. Cone, *Opt. Lett.* **24**, 1038 (1999).
 12. N. M. Strickland, P. B. Sellin, Y. Sun, J. L. Carlsten, and R. L. Cone, *Phys. Rev. B* **62**, 1473 (2000).
 13. R. M. Macfarlane, T. L. Harris, Y. Sun, R. L. Cone, and R. W. Equall, *Opt. Lett.* **22**, 871 (1997).
 14. Y. Sun, R. L. Cone, T. L. Harris, R. M. Macfarlane, and R. W. Equall, *Photon Echo Study of Optical Dephasing in Er³⁺-doped Oxide Crystals at 1.5 μ m*, *Bull. Am. Phys. Soc.* **43**, 526 (1998) and to be published.
 15. K. Liu and M. G. Littman, *Opt. Lett.* **6**, 117 (1981); P. McNichol and H. J. Metcalf, *Appl. Opt.* **24**, 2757 (1985), K. C. Harvey and C. J. Myatt, *Opt. Lett.* **16**, 910 (1991).
 16. R. W. P. Drever, J. L. Hall, F. V. Kowalski, J. Hough, G. M. Ford, A. J. Munley, and H. Ward, *Appl. Phys. B* **31**, 97 (1983); M. Zhu and J. L. Hall, *J. Opt. Sci. Am. B* **10**, 802 (1993).

17. G. C. Bjorklund, M. D. Levenson, W. Lenth, and C. Ortiz, *Appl. Phys. B* **32**, 145 (1983); J. M. Supplee, E. A. Whittaker, and W. Lenth, *Appl. Opt.* **33**, 6294 (1994).
18. D. W. Allan, *IEEE Trans. UFFC-34*, 647 (1987).
19. T. Böttger, Y. Sun, G. J. Pryde, G. Reinemer, and R. L. Cone, *J. Lumin.* **94-95**, 565 (2001).
20. N. C. Wong and J. L. Hall, *J. Opt. Sci. Am. B* **2**, 1527 (1985); F. L. Walls, *IEEE Trans. UFFC-34*, 592 (1987); R. W. Fox, L. D'Evelyn, H. G. Robinson, C. S. Weimer, and L. Hollberg, *Proc. SPIE Conference* **2378**, 58 (1995).
21. G. J. Pryde, T. Böttger, and R. L. Cone, *J. Lumin.* **94-95**, 587 (2001).
22. G. J. Pryde, T. Böttger, and R. L. Cone, *J. Lumin.*, accepted for publication (2002).
23. G. J. Pryde, T. Böttger, C. W. Thiel, and R. L. Cone, and M. J. Sellars, to be published
24. M. Zhu and J. L. Hall, *J. Opt. Soc. Am. B* **10**, 802 (1993).
25. M. J. Sellars, PhD thesis, Australian National University, Brisbane, Australia (1995)
26. O. Mör and A. Arie, *IEEE J. Quant. Elect.* **33**, 532 (1997).
27. J. L. Hall, M. S. Taubman, and Jun Ye, *Handbook of Optics*, 2nd edition, McGraw-Hill, New York 2001, Vol. IV, Chapter 27.

28. B. C. Young, F. C. Cruz, W. M. Itano, and J. C. Bergquist, Phys. Rev. Lett. **82**, 3799 (1999).
29. G. Reinemer, Y. Sun, R. L. Cone, and R. C. C. Ward, submitted to Phys. Rev. B.
30. D. Hils, J. E. Faller, and J. L. Hall, Rev. Sci. Instrum. **57**, 10 (1986)
31. C. W. Thiel, H. Cruguel, H. Wu, Y. Sun, G. J. Lapeyre, R. L. Cone, R. W. Equall, and R. M. Macfarlane, Phys. Rev. B **64**, 085107 (2001), C. W. Thiel, H. Cruguel, H. Wu, Y. Sun, G. J. Lapeyre, R. L. Cone, R. W. Equall, and R. M. Macfarlane, Optics-&Photonics-News **12**, no.12; Dec. 2001; p.64.
32. N. M. Strickland, R. L. Cone, and R. M. Macfarlane "Persistent spectral holeburning in deuterated $\text{CaF}_2:\text{Er}^{3+}$ ", Phys. Rev. B, submitted for publication.
33. R. M. Macfarlane, R. J. Reeves, and G. D. Jones, Opt. Lett. **12**, 660 (1987); R.J. Reeves and R.M. Macfarlane, J. Opt. Soc. Am. B **9**, 763 (1992); N.M Strickland, R. L. Cone, and R. M. Macfarlane, Phys. Rev. B **59**, 14328 (2000).
34. N. M. Strickland, R. L. Cone, and R. M. Macfarlane, Phys. Rev. B **59**, 14328 (1999).
35. R. W. Equall, Y. Sun, R. L. Cone, and R. M. Macfarlane, Phys. Rev. Lett. **72**, 2179 (1994).

CHAPTER 5

SPECTROSCOPY AND DYNAMICS OF $\text{Er}^{3+}:\text{Y}_2\text{SiO}_5$ Introduction and Motivation

The optical material $\text{Er}^{3+}:\text{Y}_2\text{SiO}_5$ has recently received considerable attention for spectral hole burning applications in the important 1.5 μm optical communication band. This material has also been investigated for solid-state laser applications [1] because of its good chemical and thermo-mechanical properties as well as the potential for high rare-earth doping. In 1997, Macfarlane *et al.* [2] measured the first two-pulse photon echoes and observed dephasing times up to 580 μs , triggering a number of important SHB proof-of-principle device demonstrations. These demonstrations were motivated by the desire to develop SHB technologies that would enable all-optical memory, switching, and processing at communication wavelengths [3, 4]. These potential SHB devices would store information encoded in optical pulse sequences by employing stimulated photon echoes. With this approach, the maximum temporal length of a recorded data stream is limited by the material coherence lifetime, T_2 , requiring long coherence lifetimes for some practical device applications. Even with continuous programming and accumulation [5, 10], T_2 remains an important parameter. The importance of T_2 for SHB applications

provides a motivation for fundamental research to fully explore the parameter space that influences the coherence lifetime so that optimized materials may be developed.

The material Y_2SiO_5 is well known as an excellent host for achieving ultraslow optical dephasing at low temperatures. [6] These extremely long T_2 values are expected because the constituent elements in Y_2SiO_5 have small magnetic moments ($-0.137 \mu_N$ for ^{89}Y) or small natural abundance of magnetic isotopes (4.7 % with $-0.554 \mu_N$ for ^{29}Si , 0.04 % with $-1.89 \mu_N$ for ^{17}O). [2] By minimizing the magnetic moments in the host lattice, dephasing due to nuclear and electronic spin fluctuations can be dramatically reduced.

In any Er^{3+} material, the primary sources for homogeneous broadening are magnetic interactions between the large electronic magnetic moments of the erbium ions. Lowering the Er^{3+} concentration can minimize these.

The complex magnetic dipole interactions between both electronic and nuclear spins have been the subject of research over the last six decades in the context of nuclear magnetic resonance (NMR) and electron paramagnetic resonance (EPR) as well as optical experiments. [7, 8, 9]. In the literature, ions, and their corresponding spins, are commonly divided into two groups, where the ions directly being probed in the experiment are referred to as the A-ions, and the remaining ions present in the environment, but not directly probed, are referred to as the B-ions. To achieve long dephasing times, it is necessary to suppress the spin-flip broadening caused by the environment B-ions and the optically active A-ions. Motivated by the need to minimize spin-flip broadening, we have characterized the spin-flip induced spectral

diffusion. The approach taken in this work is to characterize the effects of erbium ion concentration, magnetic field strength and orientation, and temperature on the spectral diffusion to develop a systematic strategy to optimizing the SHB material.

This chapter presents the conventional and nonlinear spectroscopy of $\text{Er}^{3+}:\text{Y}_2\text{SiO}_5$ relevant to SHB applications. Early sections cover the site-selective spectroscopy to determine the crystal field level structure and to identify spectral hole burning transitions at 1.5 μm . Crystal field levels were mapped out for the $^4\text{I}_{15/2}$ ground state and the $^4\text{I}_{13/2}$ excited state. Time-resolved fluorescence spectroscopy was used to measure the excited state lifetime, which determines the maximum achievable coherence times in the material. Full rotational Zeeman experiments were performed in the three separate optical planes of the crystal to determine the ground state and excited state g values for both sites, revealing a preferred direction for applying the external magnetic field.

Coherent nonlinear spectroscopy was used to determine material properties not accessible by conventional methods, such as the coherence lifetime, T_2 , and its spectral domain counterpart, the homogeneous linewidth, Γ_{hom} . Two-pulse photon echoes were measured as a function of magnetic field orientation in the optical extinction planes and supplemented the Zeeman experiments. The time evolution of the homogeneous linewidth due to spectral diffusion was studied with stimulated photon echo spectroscopy as a function of magnetic field, erbium concentration, temperature, and crystal orientation. The spectral diffusion observed in $\text{Er}^{3+}:\text{Y}_2\text{SiO}_5$ can be successfully described in the framework of established theories [18] with the

explicit inclusion of a direct phonon process driving the Er^{3+} spin-flips, as presented in detail in appendix C.

The spectroscopic studies described in this chapter led to significant material optimization for SHB applications while improving our fundamental understanding of these materials. This has enabled (to the best of our knowledge) the measurement of the narrowest optical resonance in a solid with a homogeneous linewidth of $\Gamma_{\text{hom}} = 73$ Hz. Photon echoes are reported at elevated temperatures of up to 5 K, which is particularly important to facilitate operation with mechanical cryo-coolers to eliminate the requirement for liquid Helium. The SHB device potential of $\text{Er}^{3+}:\text{Y}_2\text{SiO}_5$ was demonstrated for a high bandwidth 0.5 GHz correlator at $T = 4.2$ K [10].

The crystals were grown by Scientific Materials Inc. of Bozeman, Montana using the Czochralski method. The Er^{3+} concentrations varied between 0.001 and 2 atomic percent. The crystal Y_2SiO_5 belongs to the space group C_{2h}^6 with eight formula units per monoclinic cell. The Y^{3+} ions occupy two crystallographically inequivalent sites of C_1 symmetry [11] and the Er^{3+} ions substitute for Y^{3+} host ions without charge compensation. All crystals were transparent and appeared colorless. The material $\text{Er}^{3+}:\text{Y}_2\text{SiO}_5$ has 3 mutually perpendicular optical extinction axes, the b -axis equivalent with the $\langle 010 \rangle$ direction, and the D_1 and D_2 axes correspond to optical extinction directions when the sample is viewed along $\langle 010 \rangle$ between crossed polarizers. [1] All crystals were oriented, cut and optically polished perpendicular to the three optical extinction axes.

Conventional spectroscopy

Spectroscopy on $\text{Er}^{3+}:\text{Y}_2\text{SiO}_5$ has been previously reported by Li *et al.* [1] on highly doped (up to 10 at. percent Er^{3+} concentration) powder and single crystal samples for temperatures between $T = 10$ K and 300 K in the context of solid-state laser material development. Absorption and emission measurements yielded 16 crystal field components of the ${}^4\text{I}_{15/2}$ ground state for the two crystallographical sites and 14 components of the ${}^4\text{I}_{13/2}$ excited state. Crystallographic site identifications reported by Li *et al.* are uncertain. Their assignments were made according to line strength and assuming that both sites have similar energy level structure slightly shifted with respect to each other without the use of site-selective spectroscopy.

For that reason, broadband absorption experiments and site-selective fluorescence experiments were used to resolve this issue. Absorption measurements located the excited-state crystal field levels, and site-selective fluorescence confidently assigned the excited and ground state level structure to each crystallographic Er^{3+} site. A number of the previous assignments have been superseded by our more detailed and precise measurements.

Methods and Apparatus

Figure 5.1 shows the experimental setup used for absorption and site-selective fluorescence measurements.

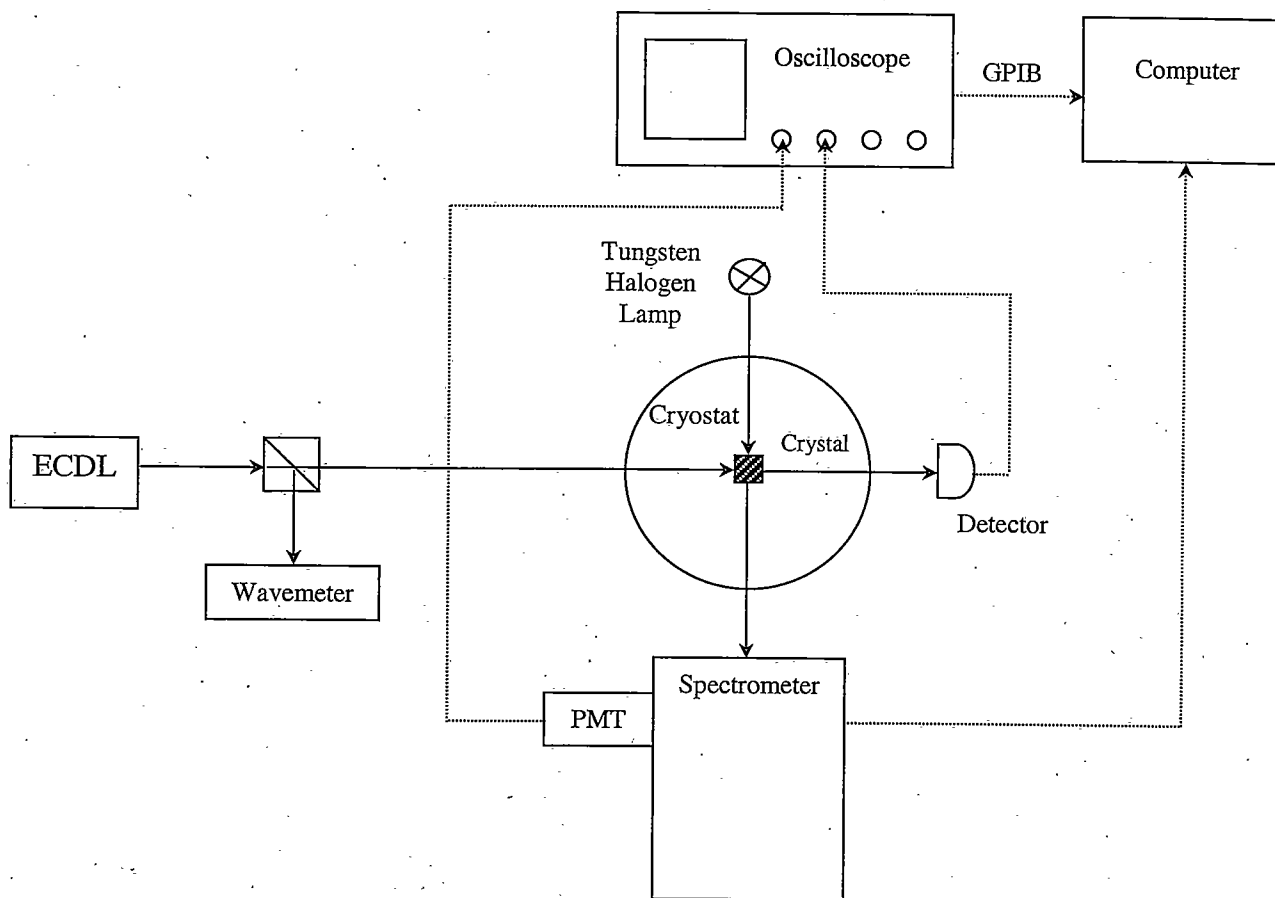


Figure 5.1 Experimental setup for broadband absorption and site-selective fluorescence.

For absorption, a 2 % $\text{Er}^{3+}:\text{Y}_2\text{SiO}_5$ crystal (batch # 0-84) was immersed in a liquid Helium bath held at $T = 1.95 \text{ K}$ using an Oxford Instruments SpectroMag cryostat with four windows providing optical access. The chosen Erbium concentration proved ideal to avoid over-absorption. Sharp absorption lines were detected. The crystal was aligned with its b -axis (2 mm) parallel to the light k -vector. Other crystal dimensions were 3 mm along D_1 and 4 mm along D_2 . For absorption measurements, an $f = 150 \text{ mm}$ lens (not shown) focused an image of a 55 W tungsten filament inside the crystal. A color filter (not shown) was placed in the beam path between the filament and cryostat with band-pass between 950 nm and 2900 nm to eliminate visible light that could be transmitted at second order by the spectrometer. A Glan-Thompson polarizer (not shown) selected the light polarization. An $f = 150 \text{ mm}$ lens (not shown) collimated the light transmitted through the crystal. The light was then focused with an $f = 200 \text{ mm}$ lens (not shown) on the entrance slit of a SPEX model 1000 M spectrometer. The spectrometer grating had 600 lines / mm blazed at $1.5 \mu\text{m}$, giving 1.6 nm / mm dispersion at the exit slit. Entrance and exit slit width were $20 \mu\text{m}$, giving a bandpass of 0.32 \AA or 0.14 cm^{-1} . The exit slit of the spectrometer was imaged onto either a liquid Nitrogen cooled Hamamatsu NIR photomultiplier tube (PMT) Model R 5509-72 or a liquid Nitrogen cooled Advanced Detector Corporation Germanium detector Model 403 L (not shown). The detector signal was further amplified using the vertical plug-in of an analog Tektronix 7904 oscilloscope, digitized by a 12-bit National Instruments Model AT-MIO-16F-5 analog to digital converter (not shown) and recorded with a

data acquisition computer that also controlled the spectrometer grating position. Signal averaging was accomplished by reading the analog to digital converter for a fixed number of times, typically 1000, at each setting of the spectrometer.

Interference fringes caused by the Germanium detector window as well as a rich absorption spectrum of water lines partially obscured the recorded absorption spectra. Water molecules in the beam path absorbed light in the spectral region of interest resulting in sharp absorption lines superimposed on the Er^{3+} absorption lines. The water lines conveniently allowed calibrating the measured absorption spectrum using the water line atlas. [12] The interference fringe background was reduced using a wedge-shaped YAG window in place of the original and was removed using a software routine. [13] Final calibrations of the spectra were verified using the narrowband ECDL as a marker in the spectrum whose wavelength was determined with the Burleigh WA 1500 wavemeter to very high precision.

Operating at $T = 1.95$ K ensured that only the lowest crystal field level Z_1 of the ${}^4\text{I}_{15/2}$ J-multiplet was initially populated. Absorption measurements mapped the crystal field levels of the ${}^4\text{I}_{13/2}$ J-multiplet. The observed absorption spectra contain two interspersed sets of absorption lines from both Er^{3+} sites, with each site experiencing slightly different crystal field splittings in the Y_2SiO_5 host.

In order to unambiguously assign the observed absorption lines to a specific crystallographic site, and to site-selectively map out the energy levels of the ${}^4\text{I}_{15/2}$ J-multiplet, site-selective fluorescence experiments were performed. In these experiments, a narrowband laser was used to individually excite each absorption

line. The fluorescence from the ${}^4I_{13/2}$ to the ${}^4I_{15/2}$ level carries a distinct signature depending on whether it was excited from an absorption line belonging to site 1 or site 2. Two distinct fluorescence spectra were observed when individually pumping all absorption lines with the narrowband ECDL, and this allowed each crystal field level of the ${}^4I_{15/2}$ ground state and ${}^4I_{13/2}$ to be assigned to site 1 or site 2. For these experiments, a 0.001 % $\text{Er}^{3+}:\text{Y}_2\text{SiO}_5$ crystal (batch # 1-544-Top) was aligned with its D_1 axis parallel to the laser k vector. The fluorescence was collected from the b - D_2 plane at an angle of 90° with respect to the laser beam. Crystal dimensions were 3 mm, 5 mm, and 4 mm along b , D_1 , and D_2 . Monitoring the ECDL wavelength with a Burleigh WA 1500 wavemeter ensured site-selective pumping. Laser absorption of the individual ${}^4I_{13/2}$ levels was also verified by scanning the ECDL over the respective absorption line and detecting the transmitted intensity with a New Focus Model 1811 InGaAs PIN-photodiode. The fluorescence spectra were obtained by scanning the spectrometer and recording the detector signal with the data acquisition computer.

Results and Discussion

Figure 5.2 shows a polarized $E // D_2$ absorption spectrum at $T = 1.95$ K for the 2 % $\text{Er}^{3+}:\text{Y}_2\text{SiO}_5$ crystal. Water lines and interference fringes have been removed from the spectrum for clarity. The spectrum contains very sharp well-separated absorption lines; 13 out of the possible 14 lines of the ${}^4I_{13/2}$ J-multiplet were observed. Line centers were determined by fitting the absorption lines.

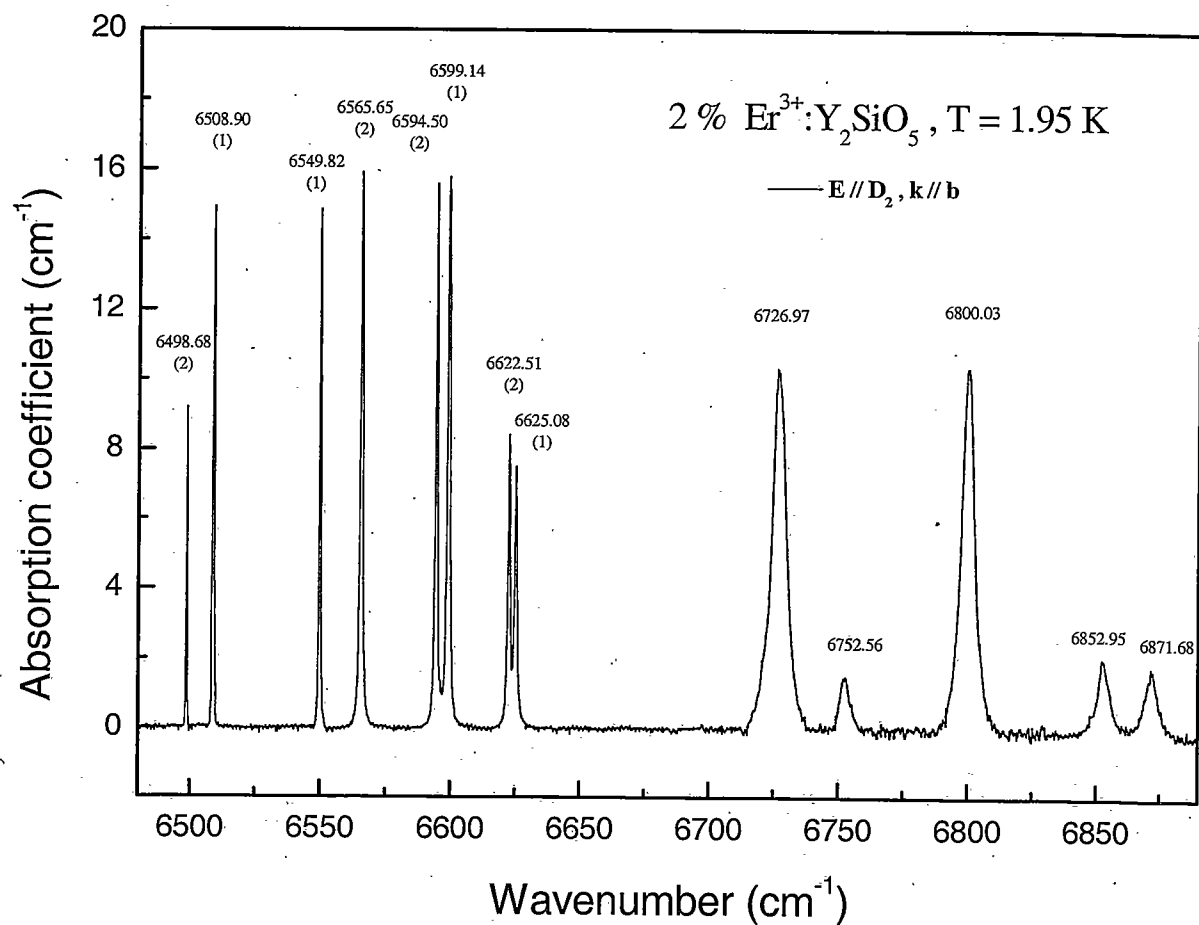


Figure 5.2 Polarized $E // D_2$ lamp absorption spectrum of $2\% \text{Er}^{3+}:\text{Y}_2\text{SiO}_5$ at $T = 1.95 \text{ K}$. Water lines and interference fringes have been removed for better visibility. Absorption line centers are given in wavenumbers and numbers in parenthesis show the crystallographic site assignments from site-selective fluorescence experiments (see text). Laser site-selective excitation was not possible above 6700 cm^{-1} .

Energies in wavenumbers are indicated above each line and site assignments are given in parentheses. The levels above 6700 cm^{-1} could not be selectively assigned due to limits of the site-selective fluorescence experiment, described below.

Figure 5.3(a) shows the fluorescence spectra excited from the ${}^4\text{I}_{13/2}:\text{Y}_1$ level of site 1 at a temperature of $T = 10\text{ K}$. Figure 5.3(b) shows that all of the eight possible lines for each site were clearly identified. Fluorescence line centers were obtained from a Gaussian fitting routine and are labeled in the graph. Due to the limited tuning range of the ECDL, it was not possible to pump levels above ${}^4\text{I}_{13/2}:\text{Y}_4$, so levels above 6700 cm^{-1} could not be assigned to a site using this method.

The crystal field level structure of $\text{Er}^{3+}:\text{Y}_2\text{SiO}_5$ determined from absorption and site-selective fluorescence experiments is shown in Fig. 5.4. The level structure obtained by Li *et al.* [1] is given for comparison. The ground state ${}^4\text{I}_{15/2}$ crystal field levels have been labeled $Z_1\text{-}Z_8$ and the ${}^4\text{I}_{13/2}$ excited state crystal field levels with $\text{Y}_1\text{-}\text{Y}_4$; higher lying Y_n assignments are undetermined. The large discrepancies of the levels Li *et al.* determined in their simpler experiment are evident. Differences can be ascribed to the superior spectral resolution, experimental conditions, calibration techniques, and sample quality used in our experiments. Spectral lines in absorption and fluorescence are sharp, well-separated and clearly resolved, while site-selective fluorescence experiments allowed unambiguous site assignment. Table 2 summarizes the crystal field level structure of the $\text{Er}^{3+}:\text{Y}_2\text{SiO}_5$ ${}^4\text{I}_{15/2}$ and ${}^4\text{I}_{13/2}$ manifolds obtained in this work.

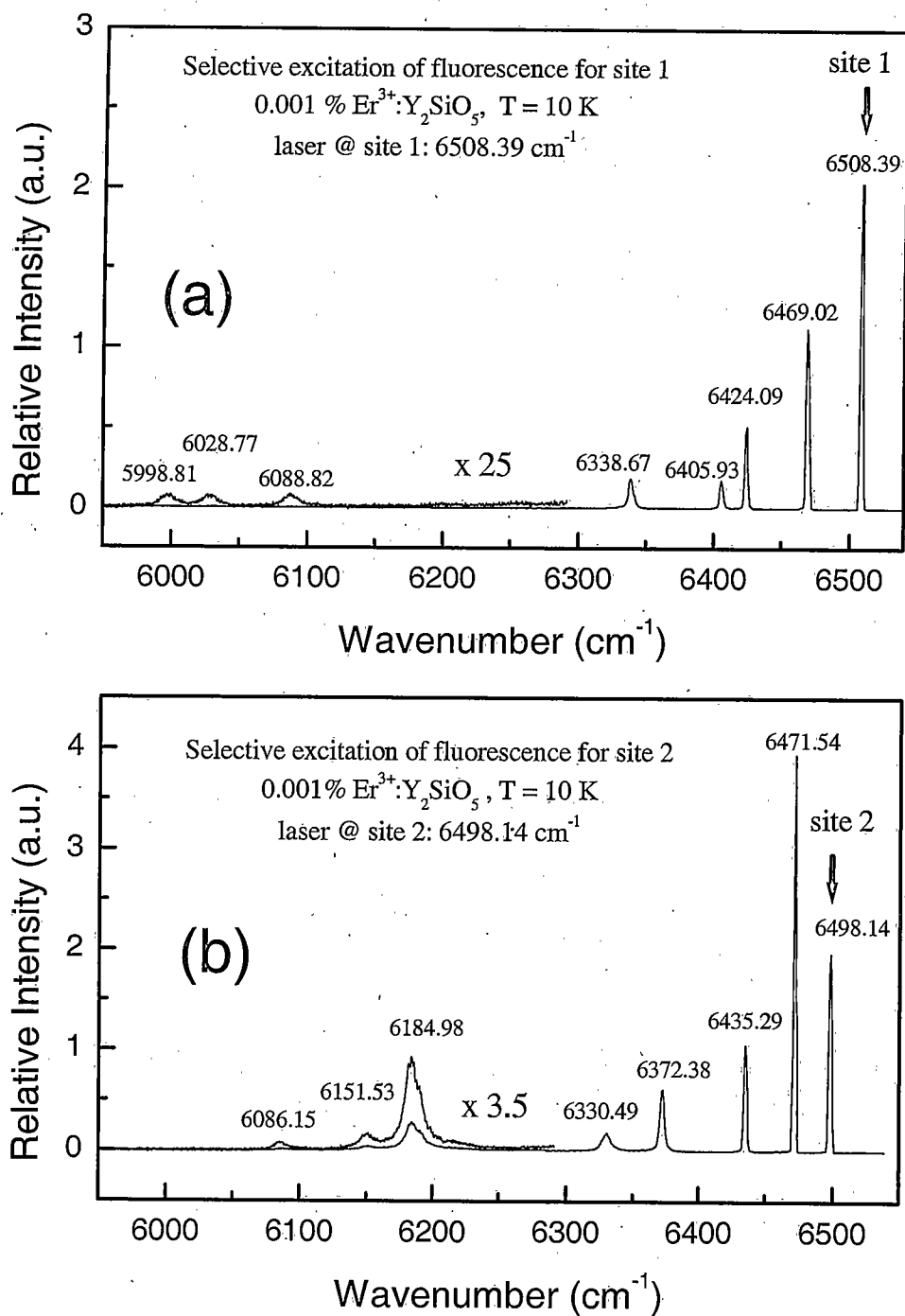


Figure 5.3 Site selective fluorescence spectra of 0.001 % $\text{Er}^{3+}:\text{Y}_2\text{SiO}_5$ at $T = 10 \text{ K}$; linecenters are given in wavenumbers. (a) Laser excitation from site 1 ${}^4\text{I}_{13/2}:\text{Y}_1$, (b) Laser excitation from site 2 ${}^4\text{I}_{13/2}:\text{Y}_1$.

Er³⁺:Y₂SiO₅ energy levels

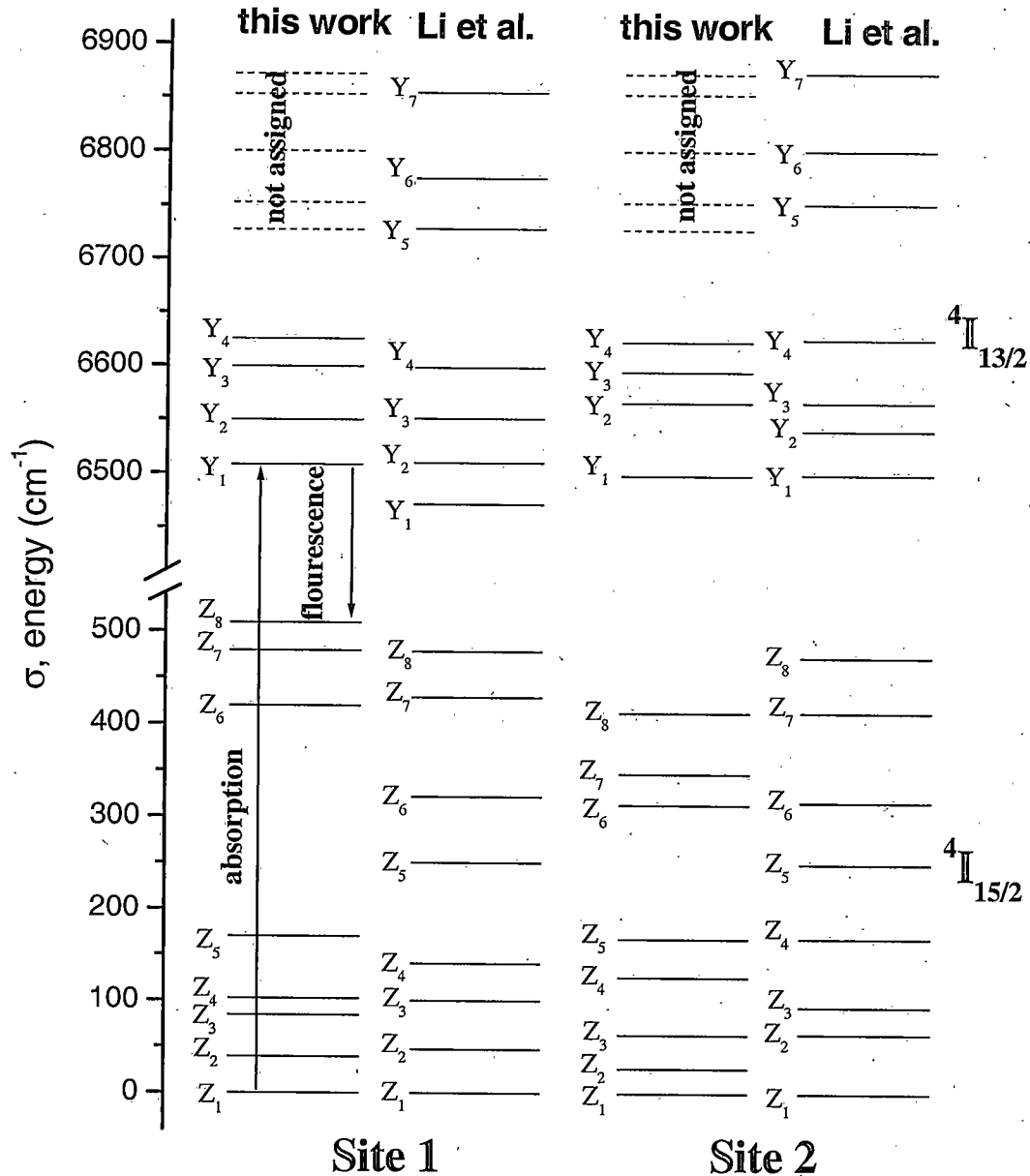


Figure 5.4 Crystal field levels of ⁴I_{15/2} and ⁴I_{13/2} multiplets of Er³⁺:Y₂SiO₅ as determined from absorption and site selective fluorescence excitation for site 1 and site 2. The right columns show values from Li *et al.* for comparison.

Table 2 Crystal field levels of $\text{Er}^{3+}:\text{Y}_2\text{SiO}_5$ as determined from absorption and site selective fluorescence experiments.

	Label	Site 1	Site 2	unassigned
${}^4\text{I}_{13/2}$ energies (cm^{-1})				6871.68
				6852.95
				6800.03
				6752.56
				6726.97
	Y_4	6625.08	6622.51	
	Y_3	6599.14	6594.50	
	Y_2	6549.82	6565.65	
	Y_1	6508.39	6498.14	
${}^4\text{I}_{15/2}$ energies (cm^{-1})	Z_8	509.58	411.99	
	Z_7	479.62	346.61	
	Z_6	419.57	313.16	
	Z_5	169.72	167.65	
	Z_4	102.46	125.76	
	Z_3	84.3	62.85	
	Z_2	39.37	26.6	
	Z_1	0	0	

Lifetime Measurements

This section describes investigations of the fluorescence dynamics of the metastable ${}^4\text{I}_{13/2}:\text{Y}_1$ excited state for Er^{3+} in both crystallographic sites. Knowledge of the excited state lifetime, T_1 , is important since it establishes an upper bound for the coherence lifetime, T_2 , given by $T_2 \leq 2T_1$. In the experiment, a laser pulse was used to pump the ${}^4\text{I}_{15/2}:\text{Z}_1$ to ${}^4\text{I}_{13/2}:\text{Y}_2$ transition of a single site. Rapid nonradiative relaxation from Y_2 to Y_1 within the ${}^4\text{I}_{13/2}$ J-multiplet of that site results in fluorescence occurring from ${}^4\text{I}_{13/2}:\text{Y}_1$ to ${}^4\text{I}_{15/2}:\text{Z}_1\text{-Z}_8$. This fluorescence intensity was

recorded as a function of time with the PMT and spectrometer that was tuned to individual ground state levels. The ${}^4I_{15/2}: Z_1$ to ${}^4I_{13/2}: Y_2$ transition was pumped to allow the laser and fluorescence signal to be spectrally separated.

Methods and Apparatus

Figure 5.5 shows a schematic of the experimental setup used to investigate the fluorescence lifetime of the metastable ${}^4I_{13/2}$ state. The same $\text{Er}^{3+}:\text{Y}_2\text{SiO}_5$ crystal and orientation was used as described earlier for fluorescence experiments. The low 0.001 % Er^{3+} concentration minimized radiative energy trapping effects that can artificially lengthen fluorescence decay times.

The ECDL light source provided 1.8 mW of single-frequency light that saturated the output of an ILX Model FOA-8100 Er fiber amplifier (EDFA) at 35 mW. A Crystal Technology Model 3165-1 acousto optic modulator (AOM) gated 1 ms duration pulses at 10 Hz repetition rate from the amplified laser beam to excite fluorescence. A $\lambda/2$ -plate (not shown) in front of the cryostat defined the orientation of the linear polarization. A PTS-500 RF synthesizer (RF-source) amplified by a 40 dB Minicircuits ZHL-5W-1 amplifier drove the AOM at 165 MHz. Laser pulses were obtained by switching the RF-power to the AOM with a Watkins-Johnson S1 RF-switch controlled by a Hewlett Packard model 8013B pulse generator at the RF switching threshold. The required pulse sequence was provided by the HP pulse generator, triggered by a Stanford Research model DG 535 delay generator.

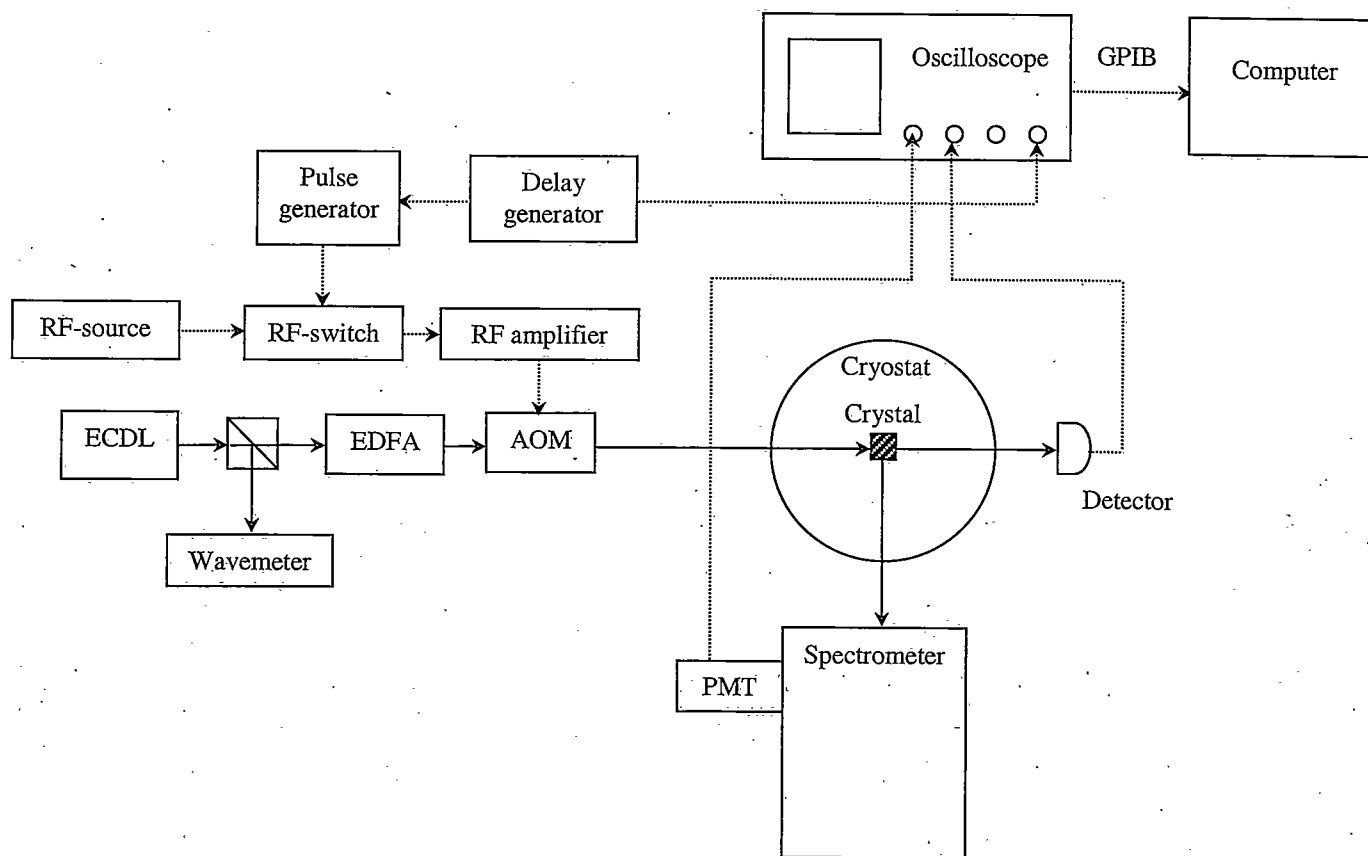


Figure 5.5 Experimental setup to measure the ${}^4\text{I}_{13/2}$ fluorescence lifetime for $\text{Er}^{3+}:\text{Y}_2\text{SiO}_5$.

Fluorescence from the crystal was collected at 90° to the laser beam geometry and focused onto the spectrometer entrance slit with the spectrometer tuned to the respective ${}^4I_{15/2}:Z_n$ transition. The spectrally resolved light leaving the spectrometer exit slit was detected by the PMT in a time-resolved fashion. The signal from the PMT was captured on a Tektronix TDS 520 D digitizing oscilloscope triggered by the DG 535 delay generator. A Burleigh WA 1500 wavemeter continuously monitored the laser wavelength. The transmitted intensity through the crystal was monitored with a New Focus 1811 InGaAs photo detector to verify absorption lines for pulsed excitation. For this purpose, the ECDL was scanned and the AOM operated in continuous wave mode.

Results and Discussion

Figure 5.6(a) shows the measured ${}^4I_{13/2}:Y_1 \rightarrow {}^4I_{15/2}:Z_1$ fluorescence decay for site 1 and Figure 5.6(b) for site 2, both at a temperature of $T = 10$ K. The observed fluorescence decays were exponential over several decades and exponential least squares fits to the data are shown as solid lines. A fluorescence lifetime of $T_1 = (11.44 \pm 0.01)$ ms was obtained for site 1, whereas $T_1 = (9.20 \pm 0.01)$ ms was obtained for site 2 from the exponential fit. Exciting the Z_1 - Y_2 inhomogeneous line on the low energy side yielded a 0.2 ms shorter lifetime. A decrease of 0.5 ms in lifetime was observed by increasing the sample temperature to $T = 40$ K.

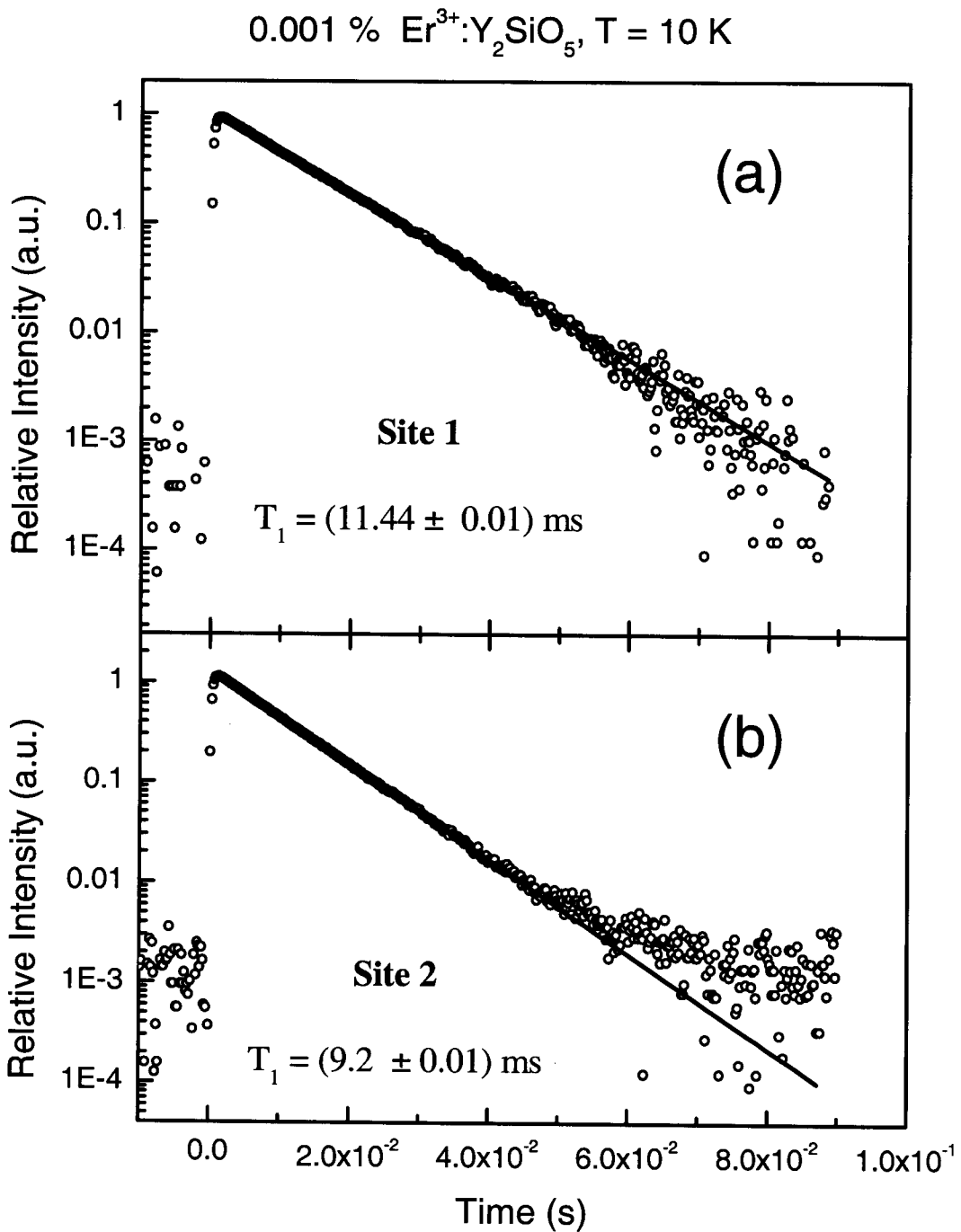


Figure 5.6 Fluorescence lifetime decay for 0.001% $\text{Er}^{3+}:\text{Y}_2\text{SiO}_5$ ${}^4I_{13/2}(Y_1) \rightarrow {}^4I_{15/2}(Z_1)$ transition at $T = 10 \text{ K}$; (a) site 1, (b) site 2. Straight lines correspond to exponential least square fits to the data.

The lifetimes were unaffected by varying the spatial location of excitation (edge versus center).

In contrast, pronounced variations in the fluorescence lifetimes of a 10 % $\text{Er}^{3+}:\text{Y}_2\text{SiO}_5$ crystal were observed by Li *et al.*[1], but without distinguishing between crystallographic sites. Li *et al.* observed a very strong geometrical effect by moving a slit in front of the crystal along the excitation direction and found a linear increase of the lifetimes from 10 ms to 17 ms with increasing excitation path length. Measuring the fluorescence temperature dependent lifetime in 1% $\text{Er}^{3+}:\text{Y}_2\text{SiO}_5$, they obtained variations between 13 ms at $T = 12$ K and 8 ms at $T = 300$ K. Li *et al.* attributed these variations to a radiative energy trapping process, during which the emitted photon is reabsorbed (trapped) and then reemitted, slowing down the overall observed fluorescence. Increasing the crystal temperature reduces the absorption coefficient, and therefore reduces the probability of trapping but it also changes the population of the individual levels in the $^4\text{I}_{13/2}$ -multiplet. Increasing the excitation path length increases the number of ions participating in the reabsorption process, which enhances the probability of trapping. The large spread in Li *et al.* results does not allow a direct comparison to our measurements.

The ultra-low Erbium concentration of 0.001% used in our experiments minimized effects associated with trapping as the small variation in fluorescence lifetime with temperature and excitation energy suggest. Hence, the values of 11.4 ms for site 1 and 9.4 ms for site 2 provide an accurate result and establish an upper bound for the fluorescence lifetime of the $^4\text{I}_{15/2}:\text{Y}_1$ level in $\text{Er}^{3+}:\text{Y}_2\text{SiO}_5$.

Stimulated photon echo T-decay experiments discussed in the nonlinear spectroscopy section set a lower limit for the fluorescence lifetime by measuring a T_1 of 9.8 ms for site 1.

Zeeman experiments

Practical operation of $\text{Er}^{3+}:\text{Y}_2\text{SiO}_5$ in SHB devices demands the application of an external magnetic field in order to obtain long dephasing times. A magnetic field lifts the Kramers degeneracy by splitting each doubly-degenerate crystal field level. The level splitting, characterized by the g value, is a key variable influencing the microscopic dynamics in $\text{Er}^{3+}:\text{Y}_2\text{SiO}_5$. Maximizing the level splitting relative to the thermal energy, kT , can “freeze out” the thermal population in the upper Zeeman level and thus reduce dephasing due to electron spin fluctuations of neighboring Er^{3+} ions. Zeeman spectroscopy is used to determine the relevant ground and excited state g values that influence the optical dephasing. Controlling the level splitting is an important part of the material optimization strategy.

Implementing such a strategy was made difficult by the extraordinary complexity encountered in $\text{Er}^{3+}:\text{Y}_2\text{SiO}_5$, which has two distinct crystallographic sites that both exhibit low C_1 site symmetry. This complexity results from the anisotropic level splitting of individual Kramers doublets and magnetic inequivalence for each crystallographic site. Hence, Zeeman experiments were carried out as a function of magnetic field orientation to find a direction that simultaneously maximizes g for all

levels important for optical dephasing. The results of these measurements led to the identification of a preferred magnetic field orientation that minimized dephasing, and thus optimized $\text{Er}^{3+}:\text{Y}_2\text{SiO}_5$ for practical SHB-device applications.

As we discussed in the previous section, the crystal field partially lifts the $2J+1$ degeneracy of the free ion, yielding up to $J+1/2$ crystal field levels. Because of Kramers degeneracy, all crystal field levels determined in the previous section are doubly degenerate and have first order magnetic moments. The ${}^4\text{I}_{15/2}$ ground J-multiplet consists of 8 Kramer's doublets and the ${}^4\text{I}_{13/2}$ excited state J-multiplet consists of 7 Kramer's doublets. Application of an external magnetic field lifts the remaining degeneracy, and each crystal field level splits into two Zeeman sub-levels. Figure 5.7 schematically shows the Zeeman splitting for the ground (g) ${}^4\text{I}_{15/2}$: Z_1 and excited state (e) ${}^4\text{I}_{13/2}$: Y_1 levels, where g and e label the ground and excited state and + and - the upper and lower Zeeman components. The letters a, b, c, and d indicate the four different optical transitions that are possible between the levels. The g-factors for the ground g_g and excited state g_e can be found from the transition energies using

$$g_e = \frac{(E_a - E_b) + (E_c - E_d)}{2\mu_B B} \quad (5.1)$$

and

$$g_g = \frac{(E_a - E_c) + (E_b - E_d)}{2\mu_B B} \quad (5.2)$$

Transition energies, σ , usually given in wavenumbers, can then be obtained from

$$\sigma_{a,d} = \sigma_0 \pm \frac{\mu_B}{2}(g_g + g_{exc})B \quad (5.3)$$

$$\sigma_{b,c} = \sigma_0 \pm \frac{\mu_B}{2}(g_g - g_{exc})B, \quad (5.4)$$

where g is the particular g value for the site of interest, σ_0 is the zero field transition energy between the ${}^4I_{15/2}:Z_1 \rightarrow {}^4I_{13/2}:Y_1$ crystal field levels, μ_B is the Bohr magneton and B is the magnetic field strength.

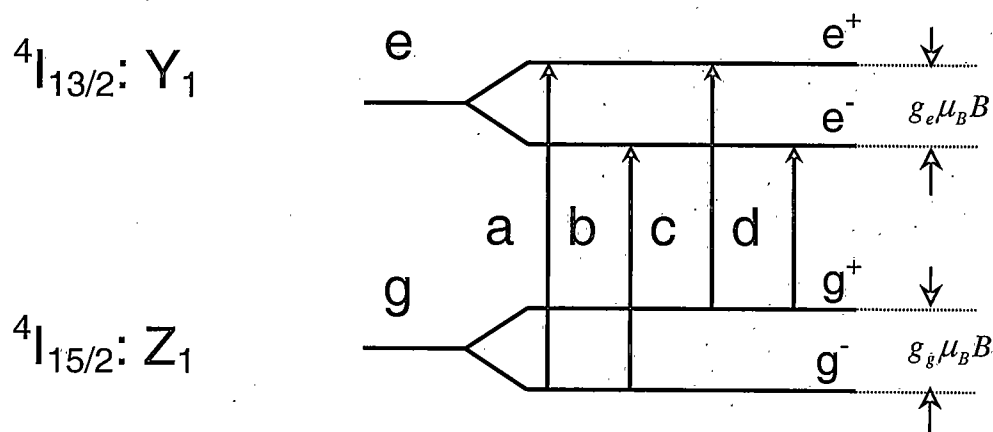


Figure 5.7 Transition labelling scheme for Zeeman laser absorption experiments.

Application of a magnetic field splits each Kramer's doublet differently, characterized by an anisotropic g-tensor unique to each doublet. For small magnetic fields, the splitting scales linearly with the applied magnetic field strength. This can be described by an effective spin Hamiltonian of the form

$$H_Z = \mu_B (\vec{S} \cdot \tilde{g} \cdot \vec{B}), \quad (5.5)$$

with \vec{S} as the effective spin ($S = \pm 1/2$), and \tilde{g} the g-tensor determined by the particular levels and crystal site symmetry. The g-tensor is a symmetric tensor of rank 2 that has six independent components in general. [14] In the principal axis representation, the components correspond to the lengths of the three major axes and the three angles that determine the orientation of the axes with respect to the crystallographic site. For high symmetry sites, crystal symmetry dictates the orientation of the g-tensor and the number of independent components can be dramatically reduced. The $\text{Er}^{3+}:\text{Y}_2\text{SiO}_5$ system, however, is of C_1 crystal site symmetry and no simplification is possible. Each crystal field level has distinct values of g_x , g_y and g_z that have to be specified by 3 angles relative to the local axes of the crystallographic site. The Zeeman Hamiltonian of equation (5.5), rewritten in components of these principal g-tensor values and components of the external magnetic field, becomes

$$H_Z = \mu_B (g_x S_x B_x + g_y S_y B_y + g_z S_z B_z). \quad (5.6)$$

It is customary to write the projections of the applied magnetic field \mathbf{B} on the principal g-tensor axes. In the case of the two crystallographic sites of $\text{Er}^{3+}\text{Y}_2\text{SiO}_5$, none of the principal g-tensor axes lies within a crystallographic plane or optical polarization extinction plane; such as D_1 - D_2 , b - D_1 and b - D_2 of the crystal. Hence, a magnetic field constrained to lie in one of these planes selects the projection of the principal g-tensor axes onto this plane. Figure 5.8 illustrates the projections for the case of the magnetic field \mathbf{B} lying in the b - D_1 plane with g_x and g_y the principal axes of the ellipse.

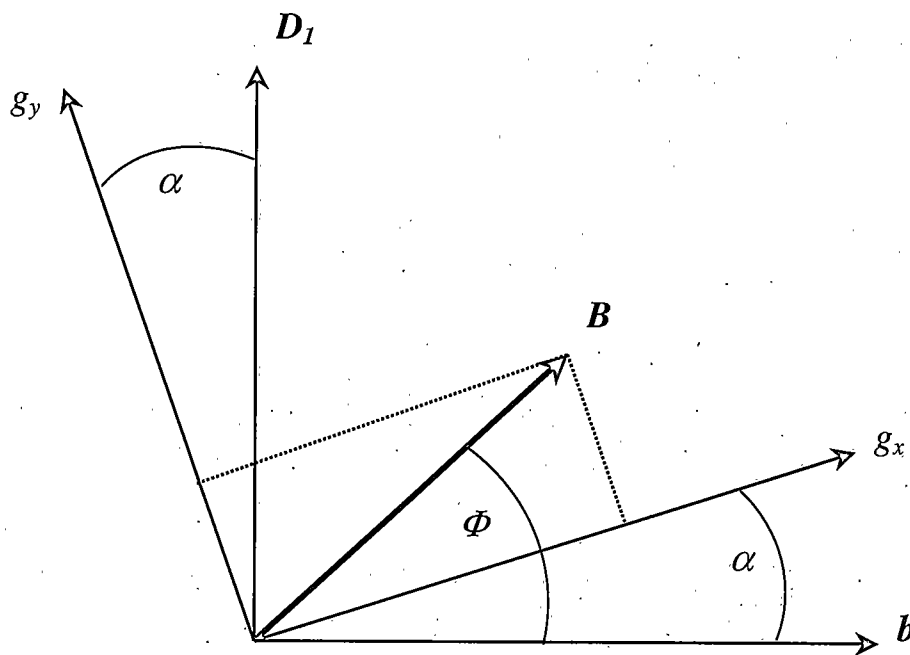


Figure 5.8 Projections of the magnetic field \mathbf{B} onto the primary \tilde{g} -tensor axes for the case of \mathbf{B} lying in the b - D_1 plane. The angle Φ references the magnetic field \mathbf{B} to the b -axis and the angle α references the g_x -axis to the b -axis.

The angle Φ references the magnetic field B orientation to the b -axis, and is measured in the experiment. The angle α references the g_x -axis to the b -axis and is unknown. The projection of B onto g_x and g_y follows from trigonometry as

$$g = \sqrt{g_x^2 \cos^2(\Phi - \alpha) + g_y^2 \sin^2(\Phi - \alpha)} \quad (5.7)$$

and allows writing g in terms of these projections. From Zeeman experiments, g is obtained as a function of Φ and a three parameter fit to this relation, according to equation (5.7), determines g_x , g_y and α . In order to reveal the full g-tensor, these projections (cuts) must be measured in all 3 optical polarization extinction planes (D_1 - D_2 , b - D_1 and b - D_2) and simultaneously fit to reconstruct unambiguously the g-tensor. The g values were determined according to equation (5.1) and (5.2) by measuring all transition frequencies for transitions a, b, c, d as a function of Φ .

Methods and Apparatus

Very sharp inhomogeneous lines with FWHM of ~ 500 MHz and the continuously tunable ECDL enabled laser absorption experiments with an accuracy approaching electron paramagnetic resonance techniques. Figure 5.9 shows the experimental apparatus for laser Zeeman absorption experiments. The crystal sample was mounted on a rotating sample rod that allowed orientation dependent measurements to be performed by rotating the sample in a constant horizontal magnetic field perpendicular to the laser beam. Figure 5.10 shows a schematic of the experimental configuration.

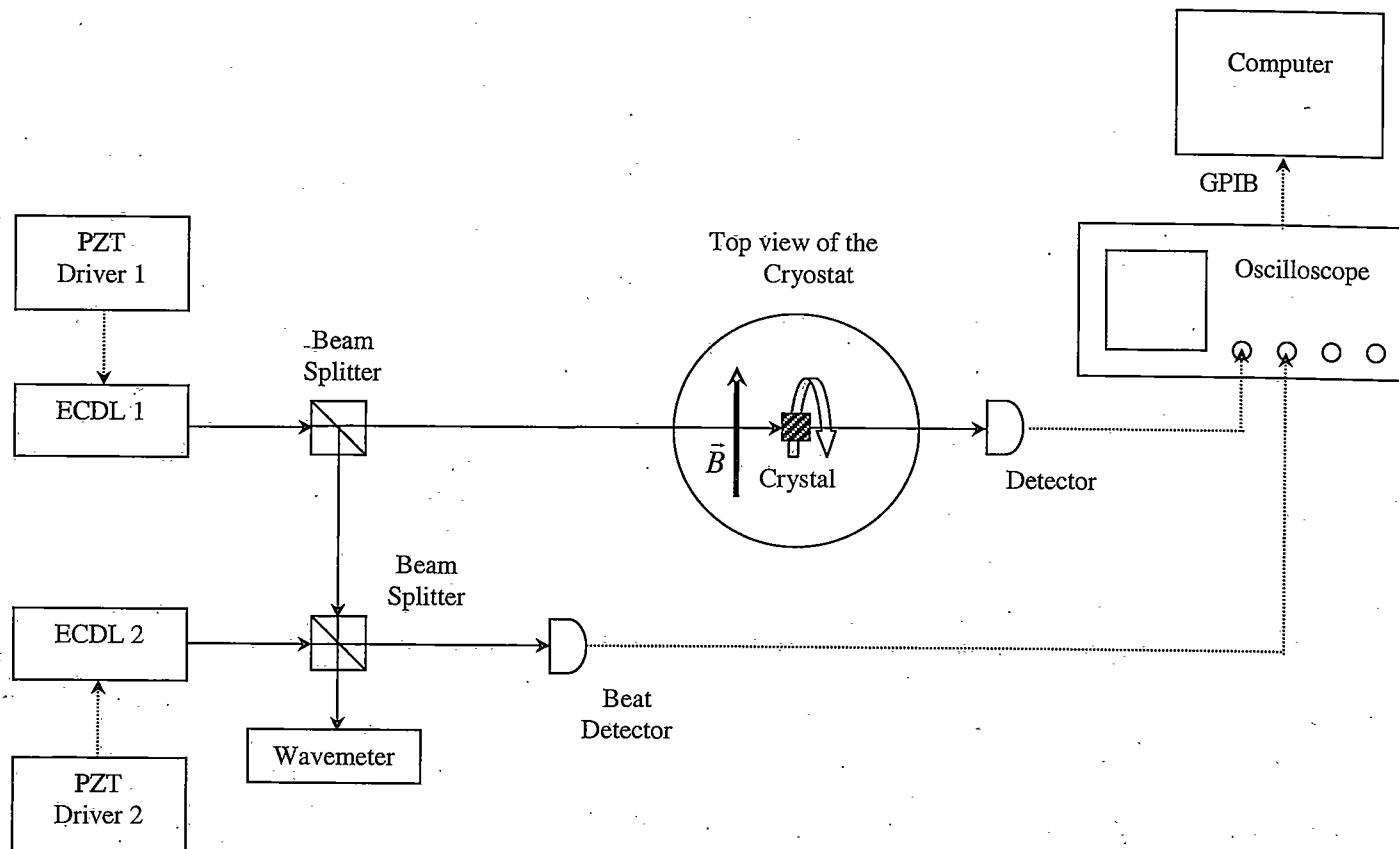


Figure 5.9 Experimental setup for laser Zeeman absorption; ECDL 2 serves to calibrate the optical frequency.

During sample mounting, a He-Ne laser beam perpendicular to the optical crystal plane of interest was reflected off the crystal. Observation of the back-reflected light while the crystal was rotated, was used to make adjustments to the crystals' alignment until incoming and reflected beams would coincide. The sample rod was build by T. L. Harris and N. Williams using a brass geared shaft and sample holder provided by M. J. M. Leask of the Clarendon Laboratory at the University of Oxford, England. The mounted sample could be rotated in the horizontal plane with a reproducibility of about $\pm 0.2^\circ$. Since the crystals were cut and polished along the optical extinction axes, orientation dependent Zeeman laser absorption experiments were carried out with the external magnetic field in the D_1 - D_2 , b - D_1 and b - D_2 planes.

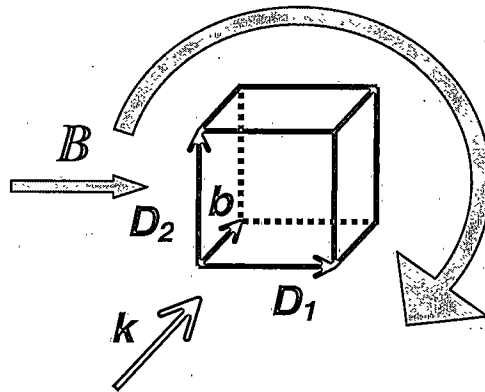


Figure 5.10 Experimental configuration for full rotational Zeeman measurements illustrated for the D_1 - D_2 plane. The lasers k vector is parallel to the b -axis of the crystal and the magnetic field is initially parallel to the D_1 direction lying in the D_1 - D_2 plane. Rather than rotating the magnetic field the crystal is rotated.

The crystal was placed inside an Oxford Instruments SpectroMag cryostat providing magnetic field strengths up to $B = 7$ T. The sample temperature could be varied between $T = 1.5$ K and room temperature using the built-in temperature controls. In order to observe all possible transitions between the Zeeman-split ground and excited states, thermal population in the upper Zeeman component of the ground state (g^+) was desired, which required operation at a minimum of $T = 5$ K. Since several tunable ECDL lasers were available, we had the luxury of using one laser to scan the spectrum and display it on the oscilloscope, while a second laser was manually tuned to each absorption peak and used as a frequency marker that could be very accurately measured by the Burleigh wavemeter. Scanning ECDL 1 over the spectral region of interest allowed the laser absorption spectra to be recorded. The frequency was scanned by tilting the piezo-driven feedback prism plate with a Stanford Research Systems DS 345 function generator (not shown) that provided a $10 V_{pp}$ triangular wave, amplified to $150 V_{pp}$ by a Thor Labs Model MDT 691Piezo Driver. Transmitted light through the crystal was detected with a New Focus 1811 photo detector and displayed in real-time on a Tektronix TDS 520D digital oscilloscope, which was triggered by the DS 345. To calibrate the laser absorption spectra, the scanning ECDL 1 was beat against ECDL 2 on a New Focus 1811 photo detector, and the beat signal between both lasers displayed on the oscilloscope as a separate trace in addition to the laser absorption scan. The narrow feature of the beat signal, limited by the band pass of the 1811 photo detector, served as a marker and was tuned to each absorption line center by manually tuning

ECDL 2. Marker frequencies, and therefore line center frequencies, could be measured with the Burleigh wavemeter to ± 100 MHz by blocking the scanning ECDL 1.

The Zeeman Effect

Figure 5.11 (a) shows typical laser absorption spectra of line a and line b for site 1 in a 0.001 % $\text{Er}^{3+}:\text{Y}_2\text{SiO}_5$ crystal and illustrates the outstanding resolution available. Here, $\mathbf{B} // \mathbf{D}_1$, $\mathbf{k} // \mathbf{b}$, and $T = 10$ K; the magnetic field was varied for each subplot. The subplots have been arranged for better visibility. As the magnetic field was increased, the spectral line splitting increased linearly; the decrease of intensity for the c-line is due to depopulation of the upper Zeeman level $g +$ with increased field. Transition energies (in wavenumbers) are given in Fig. 5.11 (b) for site 1 and Fig. 5.11 (c) for site 2. The straight lines are linear least squares fits to the data between $B = 0$ T and $B = 2$ T, showing good agreement and validating the use of the linear Zeeman Hamiltonian of equation (5.5). For higher magnetic fields, a slight deviation from the linear behavior can be seen due to mixing with other crystal field components.

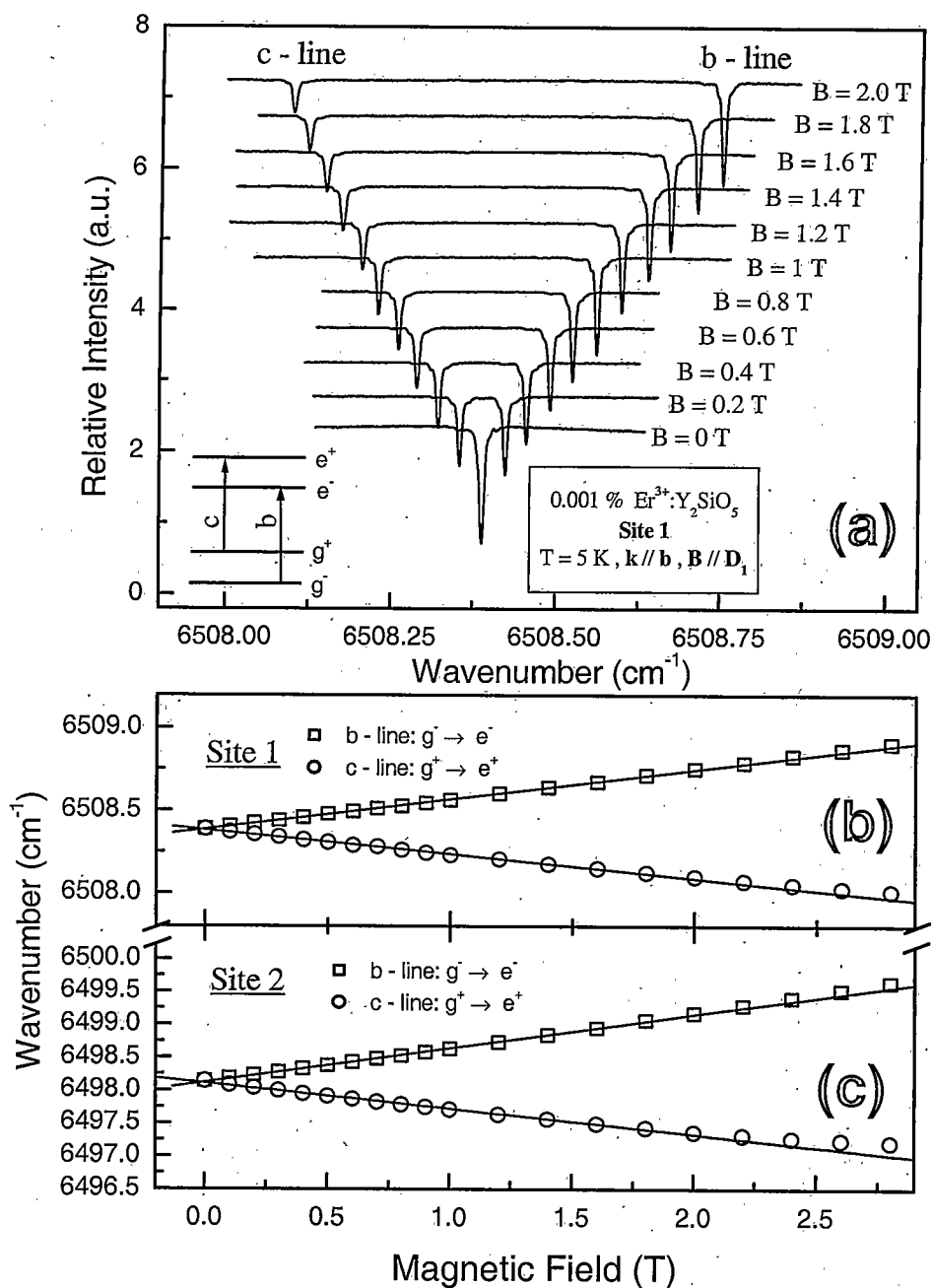


Figure 5.11 Laser absorption Zeeman spectra for 0.001 % $\text{Er}^{3+}:\text{Y}_2\text{SiO}_5$ as a function of magnetic field for $B \parallel D_1$ and $k \parallel b$ at $T = 10 \text{ K}$. (a) Sample Laser absorption scans across site 1 as the magnetic field is varied, subplots have been shifted for better visibility. (b) Zeeman transitions for site 1 with linear fits to the data between $B = 0 \text{ T}$ and $B = 2 \text{ T}$. (c) Zeeman transitions for site 2 with linear fits to the data between $B = 0 \text{ T}$ and $B = 2 \text{ T}$.

Zeeman Experiments as a Function of Field Orientation

Because the Zeeman level splitting is a key variable in achieving slow dephasing, we needed to determine the g values for both crystallographic sites as a function of applied magnetic field direction. The goal was to find a magnetic field direction where the g values of both crystallographic sites are simultaneously maximized in the ground as well as excited state. A splitting, large compared to the thermal energy, kT , reduces thermal populations in the upper Zeeman level and suppresses spectral diffusion by Er^{3+} spin-flips.

As stressed earlier, the situation in $\text{Er}^{3+}:\text{Y}_2\text{SiO}_5$ is complex due to two crystallographic sites with both exhibiting a low C_1 site symmetry. Each crystallographic Er^{3+} site has multiple orientations in the unit cell. When a distinction between individual site orientations is impossible without an applied magnetic field, the crystallographic site orientations are equivalent. However, applying an external magnetic field to the crystal along an arbitrary direction removes the orientational equivalence because the magnetic field makes different angles with the two different sets of local site axes. Even if the field is parallel to a local axis of symmetry for one ion, in general, it will not be parallel for the others and the crystallographic site breaks up into two magnetically inequivalent orientations. Each of these orientations allows observation of four transitions according to Fig. 5.7. Magnetic inequivalency was observed when the magnetic field was oriented in the $b\text{-}D_1$ or $b\text{-}D_2$ plane. Eight lines for each crystallographic site were observed corresponding to transitions within two magnetically inequivalent

orientations. When the magnetic field was applied in the optical D_1 - D_2 plane, both crystallographic sites were magnetically equivalent, leading to 4 transitions for each crystallographic site. Identifying and tracking up to 16 individual transitions as the magnetic field direction (angle Φ) was varied proved to be a challenging experiment.

Results. Figure 5.12 shows a subset of field-orientation dependent Zeeman laser absorption scans for site 2 in a 0.005% $\text{Er}^{3+}:\text{Y}_2\text{SiO}_5$ crystal at 5 K. The laser k -vector was along D_1 and the $B = 0.5$ T magnetic field direction was varied in the b - D_2 plane between subplots. The subplots were shifted vertically for better visibility. The abscissa angle, Φ , referenced the B -field direction to the crystal b -axis. Note that for angles of 0° and 90° , the B field was along b and D_2 , respectively, and the orientations became magnetically equivalent. Measuring the line intensities as a function of temperature clarified the identification of individual transitions because of change in thermal population. Subscripts 1 and 2 label transitions for the two magnetically inequivalent orientations of site 2. Cataloging all transition frequencies as a function of angle, Φ , between the magnetic field direction and the crystal b -axis yielded the full rotational Zeeman pattern of Fig. 5.13 (b) for both orientations 1 and 2 of site 2. The g -factors of ground and excited states were determined using relations (5.1) and (5.2) and are shown in Fig. 5.13 (a). The label g_{1g} denotes the g value for the ground state of orientation 1 and g_{2e} labels the g value for the excited state of orientation 2, etc. Solid lines are least squares fits to the data using relation 5.7 and show good agreement.

Figures 5.13 through 5.18 summarize the results obtained for all three optical polarization extinction planes with excellent fits for the respective g factors. Small deviations between data and fit were attributed to a slight misalignment of the crystal with respect to the magnetic field direction and the axis of rotation. A slight deviation between the crystals' optical axes and the actual crystal facets during fabrication can also account for small discrepancies. As mentioned earlier misalignments were minimized during sample mounting by reflecting a He-Ne laser beam off the optical crystal plane of interest. Observation of the back-reflected light while the crystal was rotated, was used to make adjustments to the crystals' alignment until incoming and reflected beams would coincide. Table 3 catalogues the fitting parameters, providing full knowledge of the energy level structure for arbitrary B field direction in all three optical planes using equations (5.1) through (5.4).

0.005 % $\text{Er}^{3+}:\text{Y}_2\text{SiO}_5$, site 2, $\mathbf{k} \parallel \mathbf{D}_1$, $B = 0.5 \text{ T}$, $T = 5 \text{ K}$

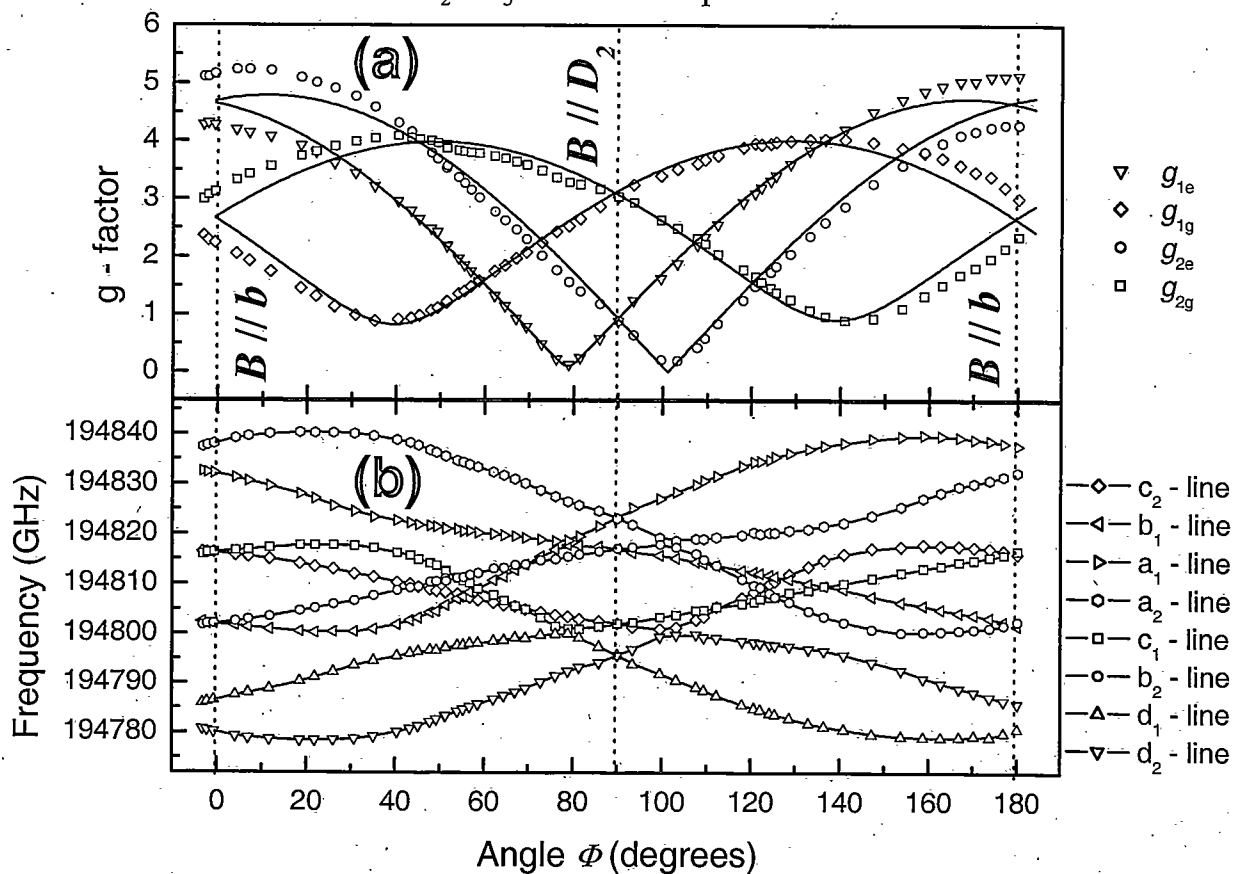


Figure 5.13 (a) Orientational-dependent g values of magnetically inequivalent orientations of site 2 in the $b\text{-}D_2$ plane determined from data of (b), g_{g1} denotes the g value for the ground state of orientation 1, g_{e2} the g value for the excited state of orientation 2 etc. Solid lines are fits to the data; deviations are due to a misalignment of the sample (see text). (b) Transition frequencies for all possible orientations of site 2 in the $b\text{-}D_2$ plane.

0.005 % Er³⁺:Y₂SiO₅, site 1, $k \parallel D_1$, $B = 0.5$ T, $T = 5$ K

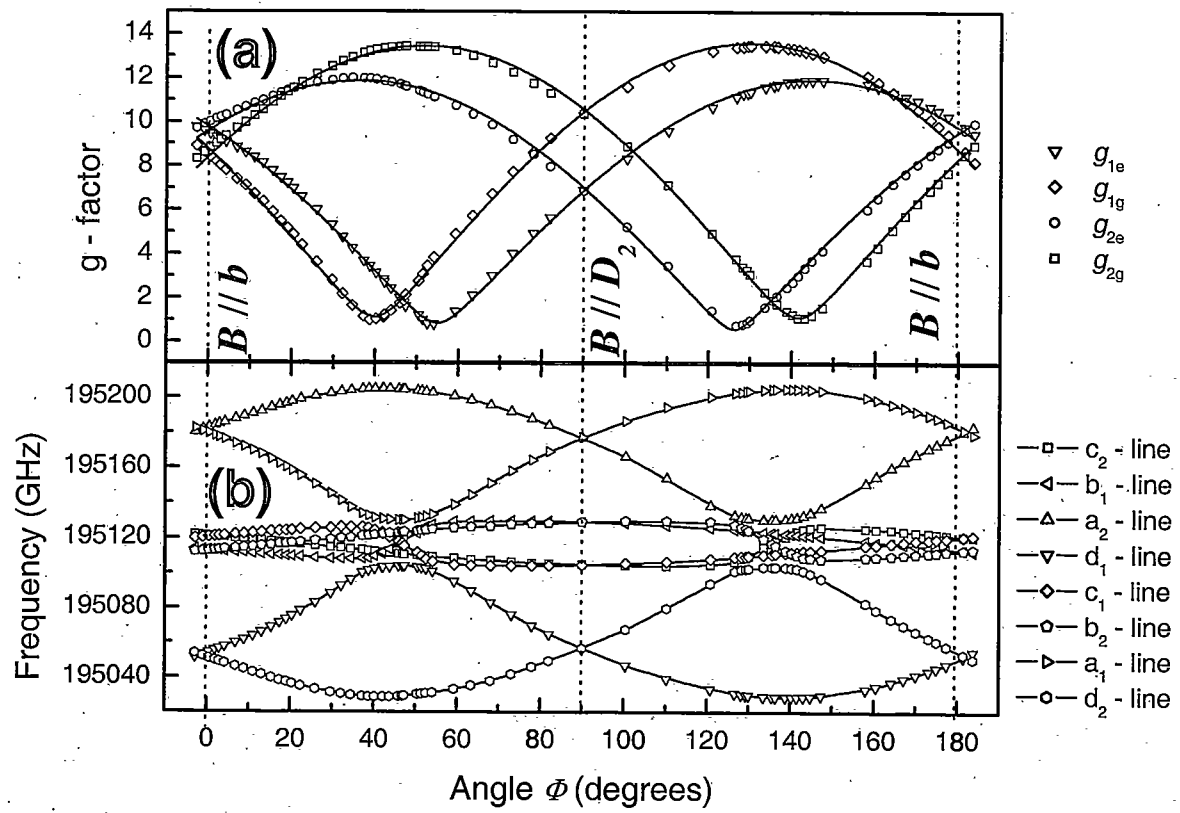


Figure 5.14 (a) Orientational-dependent g values of magnetically inequivalent orientations of site 1 in the b - D_2 plane determined from data of (b), g_{1g} denotes the g value for the ground state of orientation 1, g_{2e} the g value for the excited state of orientation 2, etc.; solid lines are fits to the data. (b) Transition frequencies for all possible orientations of site 1 in the b - D_2 plane.

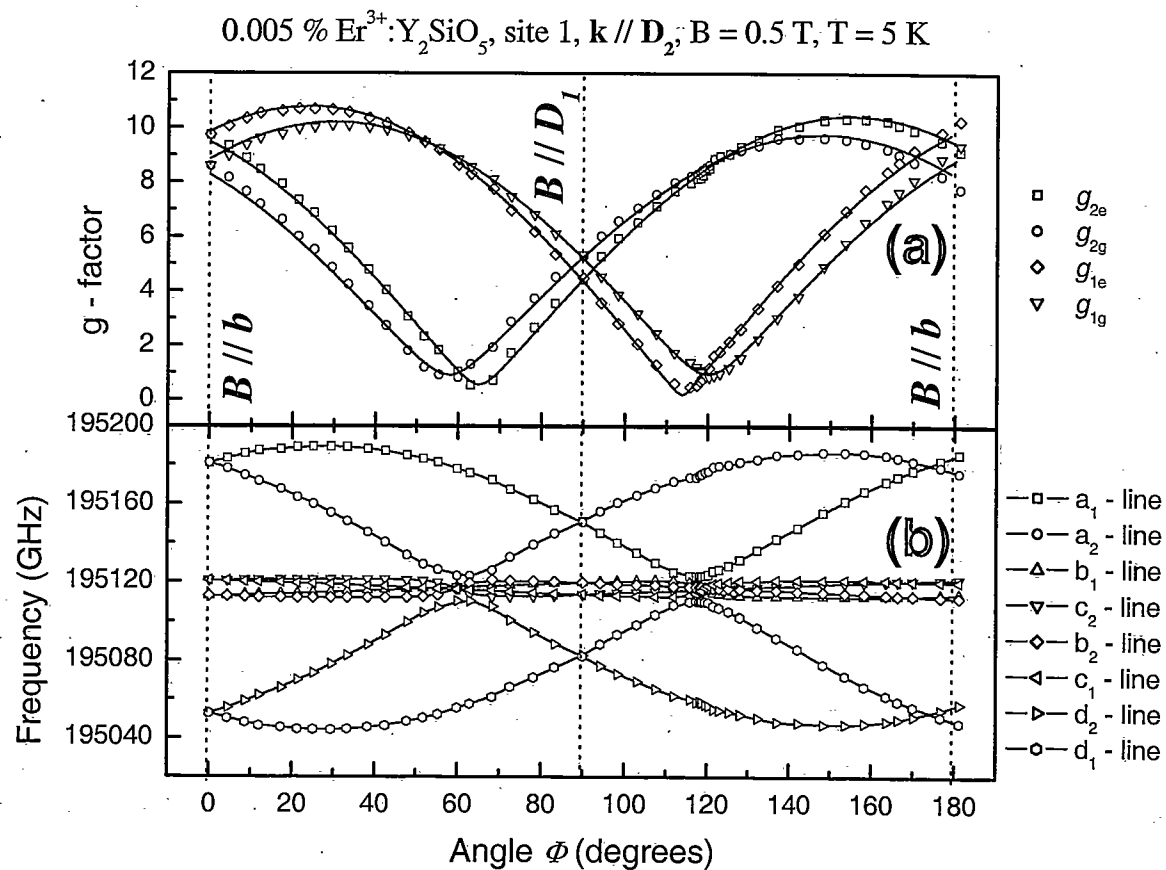


Figure 5.15 (a) Orientational-dependent g values of magnetically inequivalent orientations of site 1 in the $\mathbf{b}\text{-}\mathbf{D}_1$ plane determined from data of (b), g_{1g} denotes the g value for the ground state of orientation 1, g_{2e} the g value for the excited state of orientation 2, etc.; solid lines are fits to the data. (b) Transition frequencies for all possible orientations of site 1 in the $\mathbf{b}\text{-}\mathbf{D}_1$ plane.

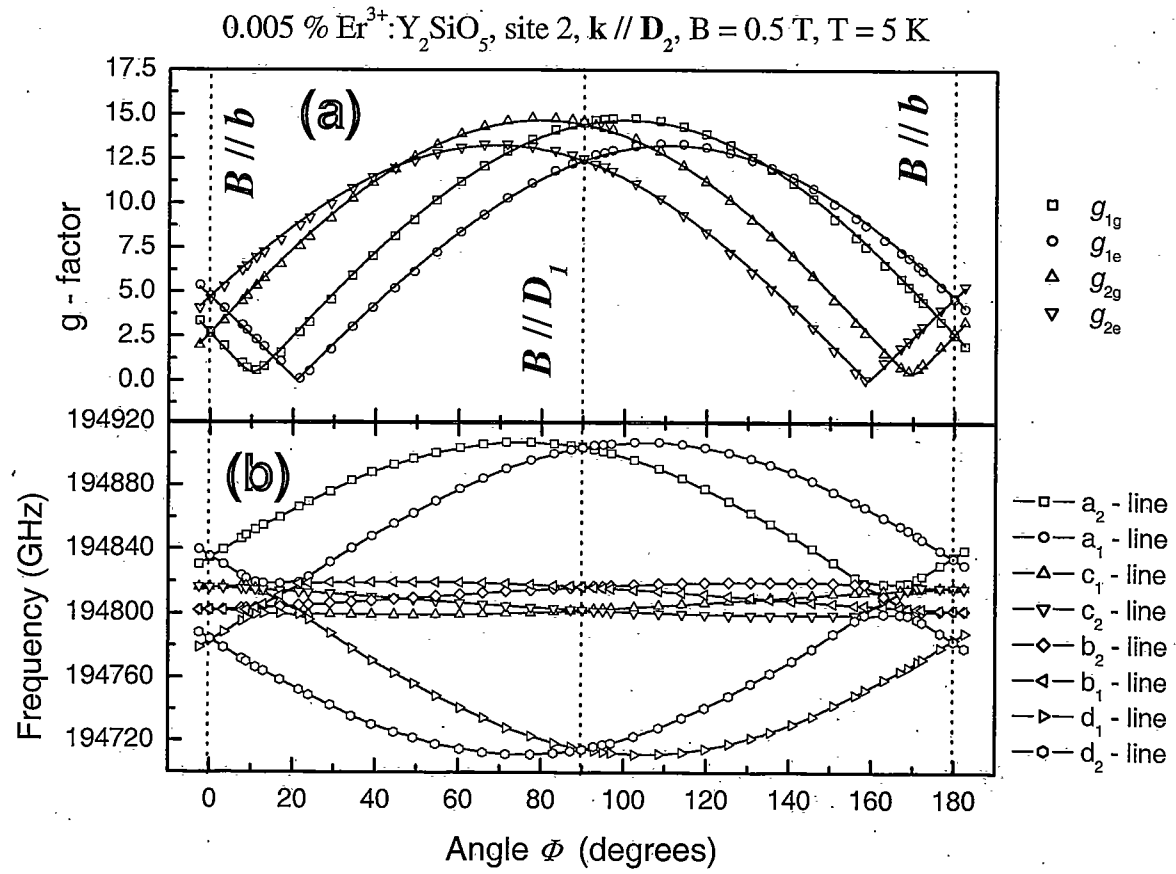


Figure 5.16 (a) Orientational-dependent g values of magnetically inequivalent orientations of site 2 in the b - D_1 plane determined from data of (b), g_{1g} denotes the g value for the ground state of orientation 1, g_{2e} the g value for the excited state of orientation 2 etc.; solid lines are fits to the data. (b) Transition frequencies for all possible orientations of site 2 in the b - D_1 plane.

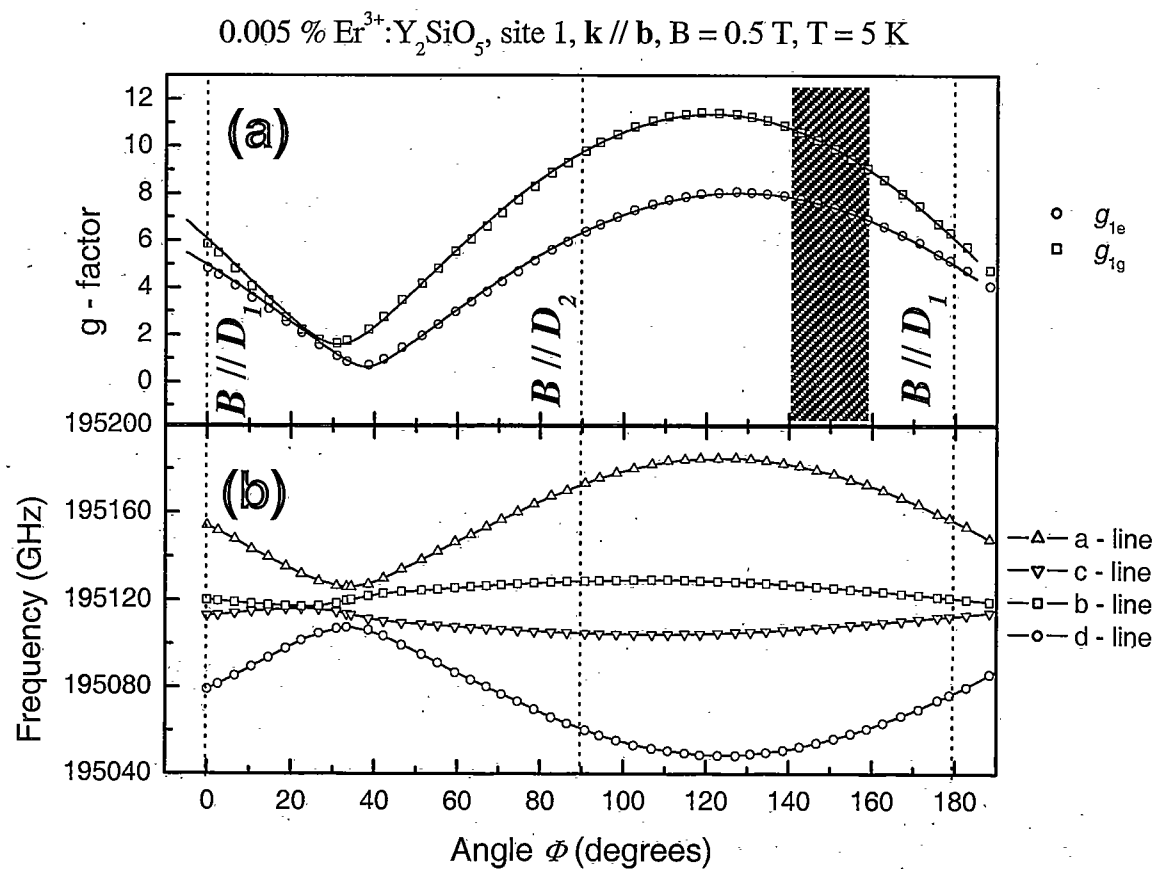


Figure 5.17 (a) Orientational-dependent g values of site 1 in the D_1 - D_2 plane determined from data of (b), g_{1e} denotes the g value for the ground state of site 1, g_{1g} the g value for the excited state of site 1; solid lines are fits to the data. (b) Transition frequencies for all possible transitions of site 1 in the D_1 - D_2 plane. The textured area between 140° and 160° in (a) depicts the optimal magnetic field direction if the influence of site 2 ions is taken into account.

0.005 % $\text{Er}^{3+}:\text{Y}_2\text{SiO}_5$, site 2, $\mathbf{k} \parallel \mathbf{b}$, $B = 0.5 \text{ T}$, $T = 5 \text{ K}$

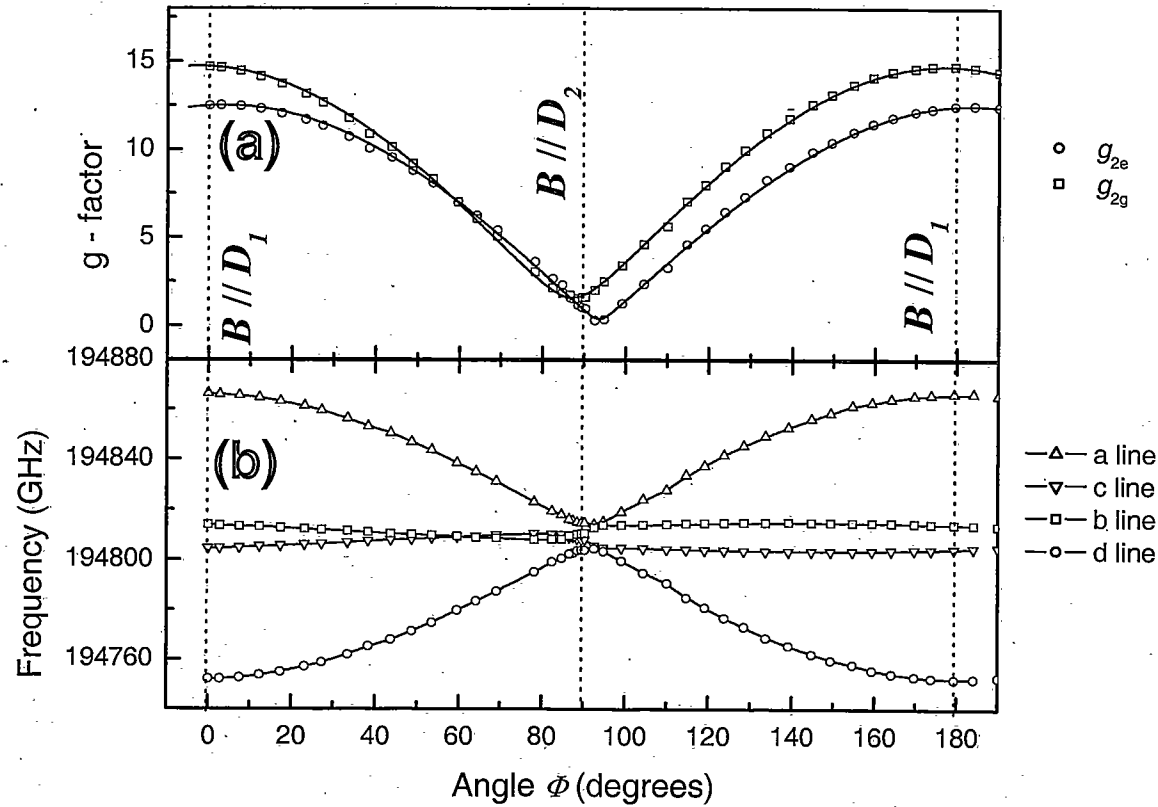


Figure 5.18 (a) Orientational-dependent g values of site 2 in the D_1 - D_2 plane determined from data of (b), g_{2g} denotes the g value for the ground state of site 2, g_{2e} the g value for the excited state site 2 ; solid lines are fits to the data. (b) Transition frequencies for all possible transitions of site 2 in the D_1 - D_2 plane.

Table 3 Fitted g-tensor values for ground and excited state of site 1 and 2 with respective orientations 1 and 2 in the three optical planes. The angle α relates the g_x axis to the D_1 direction in the D_1 - D_2 plane and the b -axis for the other two planes.

D_1 - D_2 plane		Site 1	Site 2
Excited state	g_x	8.02087±0.01679	12.50702±0.02792
	g_y	0.63631±0.04346	0.37974±0.08772
	α	127.91085±0.12078	3.69466±0.13137
Ground state	g_x	11.36172±0.02133	14.72756±0.02762
	g_y	1.58247±0.03991	1.58987±0.04473
	α	121.22867±0.11391	177.14338±0.12814

b - D_1 plane		Site 1, orientation 1	Site 1, orientation 2
Excited state	g_x	10.77633±0.02695	0.5617±0.10311
	g_y	0.18749±0.14968	10.44485±0.02783
	α	23.77973±0.13288	64.96061±0.16932
Ground state	g_x	10.20545±0.03386	9.76289±0.03396
	g_y	0.95419±0.04925	0.91461±0.09283
	α	30.12807±0.20677	147.70026±0.2373

b - D_1 plane		Site 2, orientation 1	Site 2, orientation 2
Excited state	g_x	13.24994±0.02409	13.25454±0.02479
	g_y	0	0
	α	110.89307±0.09246	69.11306±0.09457
Ground state	g_x	14.66311±0.0287	14.66543±0.02902
	g_y	0.45709±0.08159	0.45755±0.08194
	α	100.3587±0.10145	79.651±0.10175

b - D_2 plane		Site 1, orientation 1	Site 1, orientation 2
Excited state	g_x	11.92098±0.02848	11.85994±0.02978
	g_y	0.84016±0.07614	0.58302±0.10822
	α	144.98347±0.15381	36.12247±0.19583
Ground state	g_x	13.57912±0.03406	13.43397±0.03006
	g_y	1.12107±0.06126	1.13615±0.06416
	α	129.86064±0.13694	51.63984±0.15022

b - D_2 plane		Site 2, orientation 1	Site 2, orientation 2
Excited state	g_x	4.73102±0.03652	0
	g_y	0.10618±0.15422	4.78587±0.04752
	α	168.62619±0.4303	101.12957±0.57926
Ground state	g_x	4.01533±0.04217	0.91328±0.08725
	g_y	0.82658±0.0692	3.9852±0.04421
	α	129.51862±0.67863	139.0495±0.82981

Discussion. The goal of these experiments was to find a magnetic field direction that minimizes optical dephasing and suppresses spin-flips of environment ions that lead to spectral diffusion. Primary mechanisms to consider for spectral diffusion are electronic spin flip-flop transitions and the direct phonon process driving spin-flip transitions. In addition, nuclear spin flip-flops and higher order phonon processes contribute to spectral diffusion. Figure 5.19 illustrates the spin-flip broadening mechanism caused by mutual Er^{3+} - Er^{3+} spin flip-flops. Erbium environment ions in the ground state surround an optical Er^{3+} -ion center. An Er^{3+} - Er^{3+} spin flip-flop occurs, if an environment ion, initially in the upper Zeeman level of the ground state, undergoes a spin-flip transition that, via magnetic dipole-dipole interaction, simultaneously drives a spin-flop transition of another nearby environment ion. The spin flip-flop process alters the local magnetic field at the optically activated center causing an energy level shift, depicted by dotted lines in Fig. 5.19, and consequently leads to dephasing. Because the mutual spin flip-flop interaction has a magnetic dipole-dipole character, it decreases with the inverse 6th power of the distance between neighboring Er^{3+} ions.

Optical Er³⁺- ion center

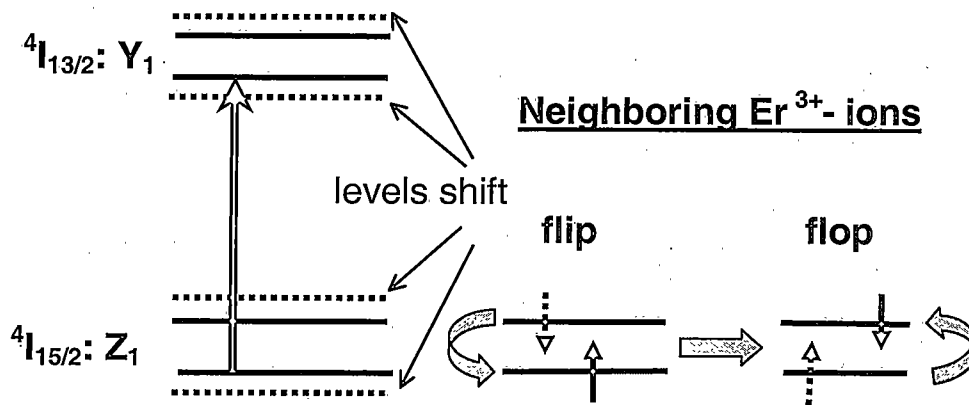


Figure 5.19 Schematic of the spin flip broadening mechanism in Er³⁺:Y₂SiO₅. An optically activated Er³⁺-ion center is shown with an optical transition between the $4I_{15/2}:Z_1 \rightarrow 4I_{13/2}:Y_1$ crystal field levels. The optical Er³⁺-ion center is surrounded by neighboring Er³⁺ environment ions in the ground state. Mutual spin flip-flop transitions and even more severe single spin-flip transitions of environment ions will cause a shift of the crystal field levels at the location of the Er³⁺-ion optical center resulting in dephasing of the optical center ion.

To investigate the likelihood of the mutual spin flip-flop interaction, it is worthwhile to estimate the average Er³⁺-Er³⁺ ion distance, the corresponding magnetic dipole field strength, and the resulting frequency shift experienced at the optical center when a neighboring ion flips. The magnetic field magnitude in spherical coordinates from a magnetic dipole is given by [15]

$$\vec{B} = \frac{\mu m}{4\pi r^3} [2 \cos \Theta \hat{r} + \sin \Theta \hat{\Theta}], \quad (5.8)$$

with the magnetic dipole moment, m , the permeability of the material, μ , and the distance to the origin, r . The maximum field strength is along \hat{r} when $\Theta = 0$ with a value

$$B_{\max} = \frac{\mu m}{2\pi r^3}. \quad (5.9)$$

The average magnetic field, $|\bar{B}|$, for a fixed distance, r , can be calculated by taking the absolute value and averaging over the angle, Θ , from 0 to $\pi/2$. This calculation involves a complete elliptical integral that is tabulated. The result is

$$|\bar{B}| = 0.771 \times B_{\max}. \quad (5.10)$$

Using $m = \frac{1}{2} g \mu_B$, with the g -value for the Er^{3+} ion in the ground state, g , and the

Bohr magneton, μ_B , equation (5.10) becomes

$$|\bar{B}| = 0.357 \times \frac{g}{r^3} [T \cdot \text{\AA}], \quad (5.11)$$

where r is in units of Angstroms [\AA] and the field, B_{\max} , is in units of Tesla [T].

Assuming $g = 6.1$ (as measured for $B // D_1$), the magnetic field at a distance of $r = 1 \text{ \AA}$ from an Er^{3+} -ion becomes $B = 2.18 \text{ T}$. However, due to the low Er^{3+} concentration used in our crystals, neighboring Er^{3+} ions will be much further apart.

To estimate the average distance between neighboring Erbium ions in a dilute 0.005 atomic percent $\text{Er}^{3+}:\text{Y}_2\text{SiO}_5$ crystal, consider the monoclinic unit cell of Y_2SiO_5 with dimension $a = 10.419 \text{ \AA}$, $b = 6.726 \text{ \AA}$, $c = 12.495 \text{ \AA}$, and $\beta = 102.63^\circ$ [11], where β defines the angle between a and c , giving a unit cell volume of $V = 854.44 \text{ \AA}^3$. The

unit cell contains 16 Y^{3+} ions giving a Y^{3+} ion density of $1.87 \times 10^{22} \text{ cm}^{-3}$. Assuming each Y^{3+} ion occupies the center of a cube with side-length, l , the Y^{3+} ion-ion distance will be given by the dimension, l , of the cube. In general, the average distance can be estimated using

$$l = \left(\frac{V}{N_v c} \right)^{\frac{1}{3}} \quad (5.12)$$

with N_v , the number of sites in the volume, V , and c , the percentage of occupation of these sites. The unit cell contains 16 Y^{3+} ions, so that the average Y^{3+} ion-ion distance will be approximately $l = (854 \text{ \AA}^3 / 16)^{1/3} = 3.77 \text{ \AA}$. For a 0.005 atomic percent $Er^{3+}:Y_2SiO_5$ crystal, the Y^{3+} site is only 0.005 % occupied by Er^{3+} ions. The Er^{3+} ions substitute for Y^{3+} ions with equal site occupation into two crystallographic Er^{3+} sites. Assuming that only ions belonging to the same crystallographic site contribute to dephasing gives $N_v = \frac{16}{2} = 8$. This assumption is justified, as we will see later, for the preferred magnetic field direction and the average distances between neighboring Er^{3+} -ions according to (5.12) will be 129 \AA . Hence using relation (5.11), a neighboring Er^{3+} ion causes a magnetic field of $B = 1.0 \times 10^{-6} T$ at the location of the optical center, and a single environment ion spin-flip in the ground state induces a frequency shift, $\Delta\nu = \mu \cdot \Delta B / h$, at the optical center of $\Delta\nu \cong 43 \text{ kHz}$. Indeed, stimulated photon echo spectroscopy at small magnetic fields in the long waiting time limit, described later, measures homogeneous linewidths of this magnitude. Because neighboring ions are $\sim 129 \text{ \AA}$ apart and the magnetic dipole-

dipole interaction falls off with $1/r^6$, mutual spin flip-flops are not expected to be significant for this concentration. Even for the higher erbium concentrations used in our experiments, such as 0.02 % and 0.1 %, the spin flip-flop process is expected to be weak.

Figure 5.20 shows the “direct” phonon scattering process. The direct process gives rise to single phonon emission or absorption with phonon energies equal to the ground state Zeeman splitting. [16] Absorption of a phonon promotes a spin from the lower Zeeman level into the upper Zeeman level, and spontaneous emission of a phonon causes a spin in the upper level to relax to the lower Zeeman level. Due to the low cryogenic temperatures, the direct phonon process is expected to be the dominant interaction that can cause spin-flips of Er^{3+} environment ions. The two-phonon processes involve higher-energy phonons. Stimulated photon echo spectroscopy, described later in the chapter, supported this argument.

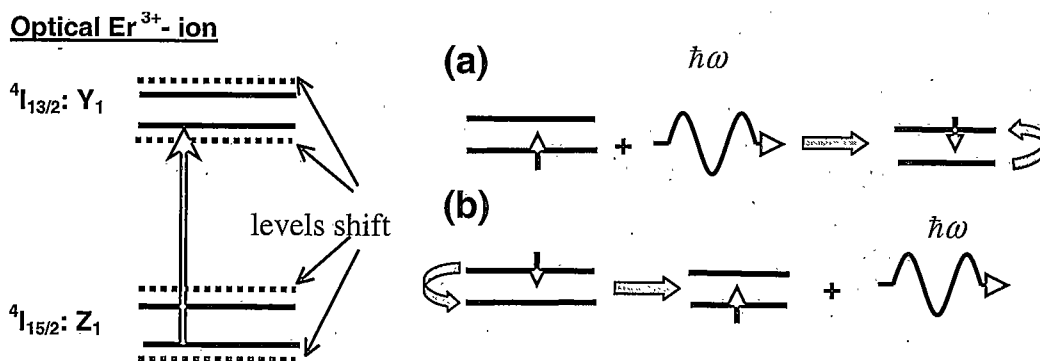


Figure 5.20 Schematic of the direct phonon process in the Zeeman split Er^{3+} ground state. (a) Phonon absorption with energy of the Zeeman splitting raises a spin to the upper Zeeman level. (b) Spontaneous phonon emission relaxes a spin to the lower Zeeman level.

The g values measured describe the magnetic field strength and directional dependence of ground state splitting, ΔE_g , and excited state splitting, ΔE_e . In our optimization strategy to suppress dephasing, we required the energy splittings, ΔE , to be as large as possible with respect to the thermal energy, kT , available to the ions. In addition to maximizing the level splittings, a magnetic field orientation that ensures magnetic equivalence of Er^{3+} ions is important. In general, all Er^{3+} ions play a role in dephasing optically excited Er^{3+} ions. However, for a device application only those ions that are resonant with the laser are useful. In the best case, all ions are in resonance with the laser, which makes them magnetically equivalent. Magnetic equivalence minimizes the overall doping concentration required for optical absorption and increases the overall Er^{3+} - Er^{3+} inter-ion distance, thereby reducing interactions. In addition, a reduced number of site orientations simplifies the anisotropic g value-patterns providing an easier guide for a "good" magnetic field orientation. Of course, in a real material system, these optimization strategies are often mutually incompatible.

Following these optimization strategies, the magnetic field should be applied in the D_1 - D_2 plane of the crystal because both crystallographic sites remain magnetically equivalent upon rotation of the magnetic field in that plane. Site 1 is the preferred site in this plane because it exhibits higher optical absorption (see Fig. 5.2) and longer excited state lifetime (see Fig. 5.6 (a)). From the orientationally dependent g -values of the ground and excited states shown for site 1 in Fig. 5.17 (a), it is clear that maximum splitting occurs for both ground and excited state when the

magnetic field is at an angle $\Phi \sim 120^\circ$ with respect to the D_1 axis. Comparing this region with Fig. 5.18 (a) for ground and excited state g -values of site 2 reveals that its maximum splitting for ground and excited state also occurs simultaneously, but offset from the 120° to $\sim 180^\circ$ (near D_1). Because spin flips due to ions residing in crystallographic site 2 will also influence dephasing of optical center ions of site 1, both directions have to be considered. In Fig. 5.17 (a) a textured area between 140° and 160° marked the region that held the most promise for orienting the magnetic field in the D_1 - D_2 plane. The ground state g value of site 1 was large and varies in this region with angle Φ between 7.85 and 6.8, whereas the excited state g value was even larger, varying between 10.73 and 8.9. In addition, the ground state g value of site 2 was large, having values between 9.1 and 11.45 and thus indicates a "frozen-out" population of the upper Zeeman component. The excited state g -values of site 2 should not have an influence because optical excitation occurred at the energy of site 1.

In conclusion, the energy level structure for both crystallographic sites was completely mapped out as a function of external magnetic field orientation in three optical extinction planes of the crystal. These experiments identified a magnetic field orientation that maximizes the overall energy splittings for all Er^{3+} sites. The most promising configuration orients the magnetic field, B , at an angle, Φ , between 140° and 160° degrees to the crystal D_1 -axis in the D_1 - D_2 plane.

Nonlinear Spectroscopy

To confirm Er^{3+} spin-flip broadening as the dominant mechanism for spectral diffusion and to validate the suggested magnetic field orientation for SHB device applications, further characterization of the material was pursued. Coherent nonlinear spectroscopy gave access to material parameters hidden to conventional methods because of limited spectral resolution. Two-pulse photon echo spectroscopy was used to determine the homogeneous linewidth, while the evolution of the spectral hole width due to spectral diffusion was studied with stimulated photon echo spectroscopy. Spectral diffusion in $\text{Er}^{3+}:\text{Y}_2\text{SiO}_5$ was characterized and controlled by exploiting the parameters of magnetic field strength, erbium concentration, and operational temperature. In addition, experimental results on spectral diffusion provided insight into the microscopic spin dynamics and improved our fundamental understanding of the material. Experimental results were successfully described with a theoretical model for the effect of spin flips on the linewidth that explicitly included the direct phonon process. [18] The theoretical framework is presented in appendix C.

Methods and Apparatus

Figure 5.21 displays a schematic of the experimental apparatus used to measure two-pulse photon echo decays and stimulated echo decays with a laser that was, for some experiments, stabilized to a spectral hole burning frequency reference.

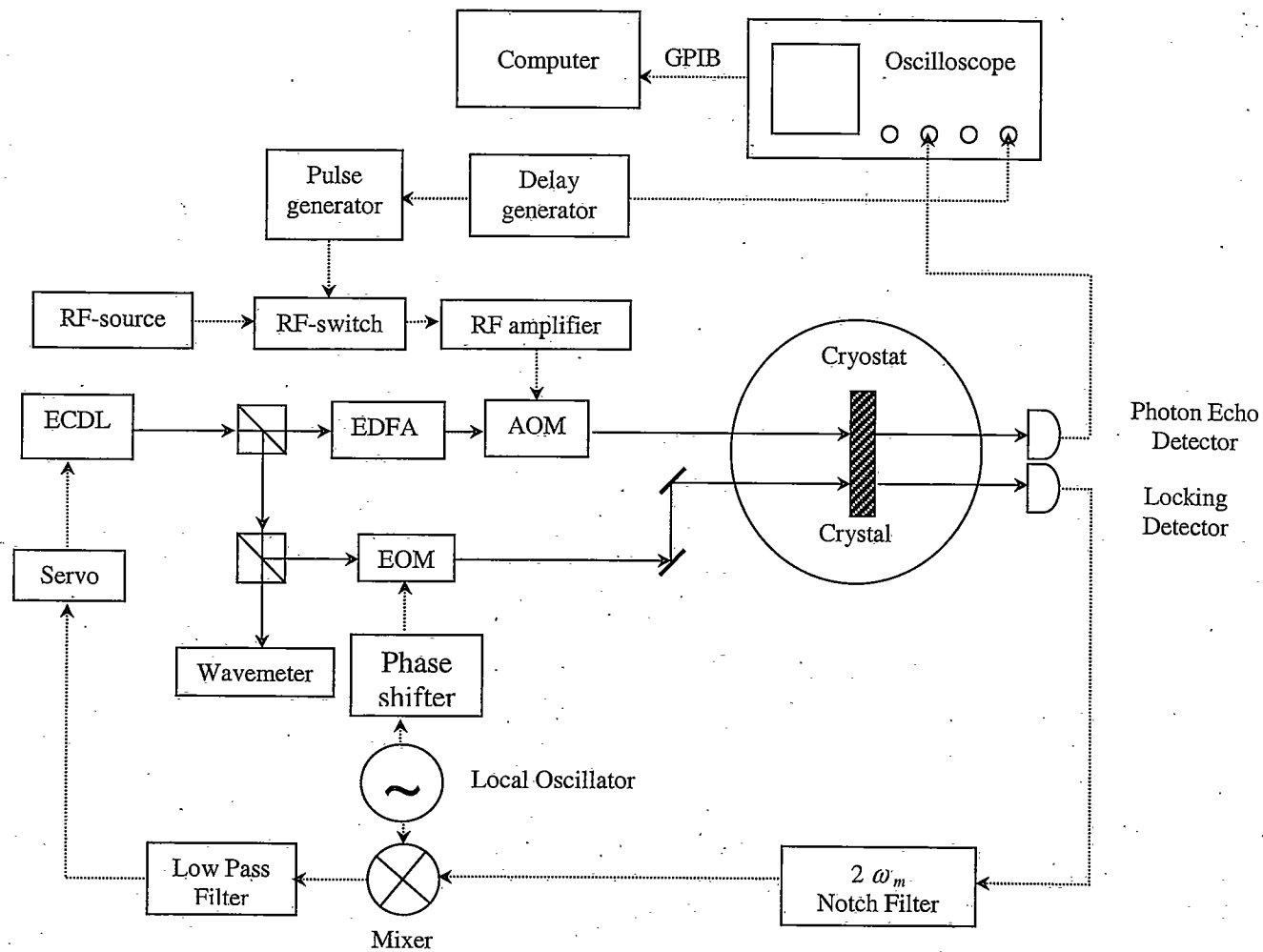


Figure 5.21 Experimental setup to measure two pulse photon echoes and stimulated echoes with a laser stabilized to a spectral hole frequency reference in a separate region of the same or different crystal.

The $\text{Er}^{3+}:\text{Y}_2\text{SiO}_5$ crystal was placed in an Oxford Instruments SpectroMag cryostat that allowed measurements as a function of magnetic field and temperature. For angle-dependent measurements, the sample was mounted on the rotating sample rod described earlier. The ECDL output power of ~ 1.8 mW saturated an Erbium doped ILX Model FOA-8100 fiber amplifier at 35 mW. For most experiments, the laser beam was focused inside the crystal to a waist of radius ~ 25 μm using a lens of $f = 125$ mm (not shown), and a 125 mm lens collimated the beam exiting the cryostat. A Crystal Technology model 3165-1 acousto optic modulator (AOM) gated the photon echo pulse sequence at a 10 Hz repetition rate from the amplified continuous wave ECDL laser beam. A $\lambda/2$ -plate (not shown) in front of the cryostat controlled the linear polarization of the exciting pulse. The AOM was driven with a 165 MHz RF signal, that was generated by a PTS-500 synthesizer (RF-source), switched with a Watkins-Johnson S1 RF-switch, and amplified by a 40 dB Minicircuits ZHL-5W-1 amplifier. The pulse sequence was programmed with a Stanford Research model DG 535 delay generator interfaced by GPIB to the data acquisition computer. The pulse sequence was produced by up to three Hewlett Packard model 8013 B pulse generators whose outputs were summed with a summing amplifier (not shown).

For experiments with a laser stabilized to a spectral hole frequency reference, part of the laser beam was split off before the AOM and used to lock to a spectral hole located either at a different location in the same crystal or in another crystal that was spatially separated from the photon echo beam. A complete description of the

locking apparatus was given in Chapter 4. Initial experiments were performed with the laser stabilized. However, choosing typical $\pi/2$ -pulse widths to be of ~ 500 ns length, led to a ~ 2 MHz spectral width. That value was large compared to the homogeneous broadening observed and relaxed the requirement for an ultra-sharp laser linewidth, so that most experiments were carried out without the stabilization engaged.

To improve the on / off contrast ratio for the echo excitation pulses, and to cancel any net shift in the laser frequency due to the AOM, a second AOM (not shown) was used in the photon echo beam. The observed photon echo signals were strong enough for direct detection with a New Focus 1811 photodiode. The signal was displayed on a Tektronix TDS 520D digital oscilloscope that was interfaced by GPIB with the data acquisition computer. To enhance the separation of weak echoes, the photon echo signal from weak echoes was gated from the transmitted beam by a third AOM (not shown) to discriminate against the excitation pulses. The absolute frequency of the laser was monitored with a Burleigh WA 1500 wavemeter. All photon echo experiments were fully computer controlled using data acquisition routines developed by previous students and refined by C. W. Thiel.

Two-Pulse Photon Echo Spectroscopy as a Function of Field Orientation

The previous section on rotational optical Zeeman spectroscopy determined the magnetic field direction in the D_1 - D_2 plane that should minimize optical dephasing

in $\text{Er}^{3+}:\text{Y}_2\text{SiO}_5$ due to Er^{3+} interactions and therefore minimize the homogeneous linewidth. To confirm those predictions, two-pulse echoes were used to measure optical dephasing as a function of magnetic field orientation in the D_1 - D_2 and the b - D_2 plane. Slow dephasing, i.e. narrow homogeneous linewidths, should be expected along the magnetic field direction that simultaneously maximizes the g-values of ground and excited state for both crystallographic sites. In contrast, faster dephasing, i.e. large homogeneous linewidths, should be expected along magnetic field orientations with small g-values for both sites. Furthermore, due to the magnetic inequivalency of ions in the b - D_2 plane, the lack of a distinct magnetic field orientation that simultaneously maximizes the g-values for all site orientations should result in larger homogeneous linewidths for this plane.

Experiments were carried out at $B = 3$ T and $T = 1.6$ K with the magnetic field orientation adjustable in two optical extinction planes. For the D_1 - D_2 plane, a 0.001 % $\text{Er}^{3+}:\text{Y}_2\text{SiO}_5$ crystal was used and two-pulse photon echoes were measured on site 1. In the b - D_2 plane, a 0.005 % $\text{Er}^{3+}:\text{Y}_2\text{SiO}_5$ crystal was used and two-pulse echo experiments were performed on orientation 2 of site 1, as specified from the Zeeman experiments.

Results

Figure 5.22 (a) summarizes the rotational g-value pattern for site 1 and 2 in the D_1 - D_1 plane in order to facilitate comparison to the orientation dependent homogeneous linewidth shown in Fig. 5.22 (b).

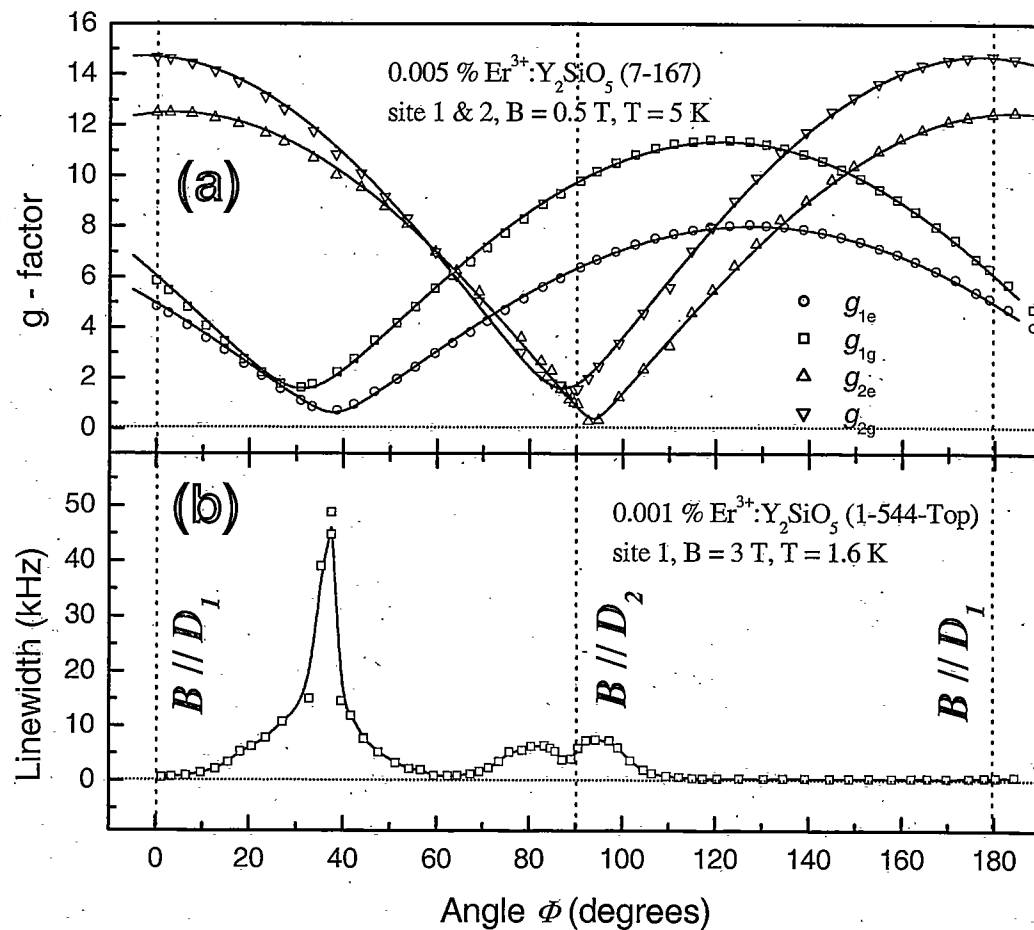


Figure 5.22 (a) Orientation-dependent g values of site 1 and site 2 in the D_1 - D_2 plane, g_{1g} denotes the g value for the ground state of site 1, g_{2e} the g value for the excited state of site 2, etc.; solid lines are fits to the data. (b) Correlation with the homogeneous linewidth of site 1 measured with two pulse echoes in the D_1 - D_2 plane as a function of magnetic field orientation.

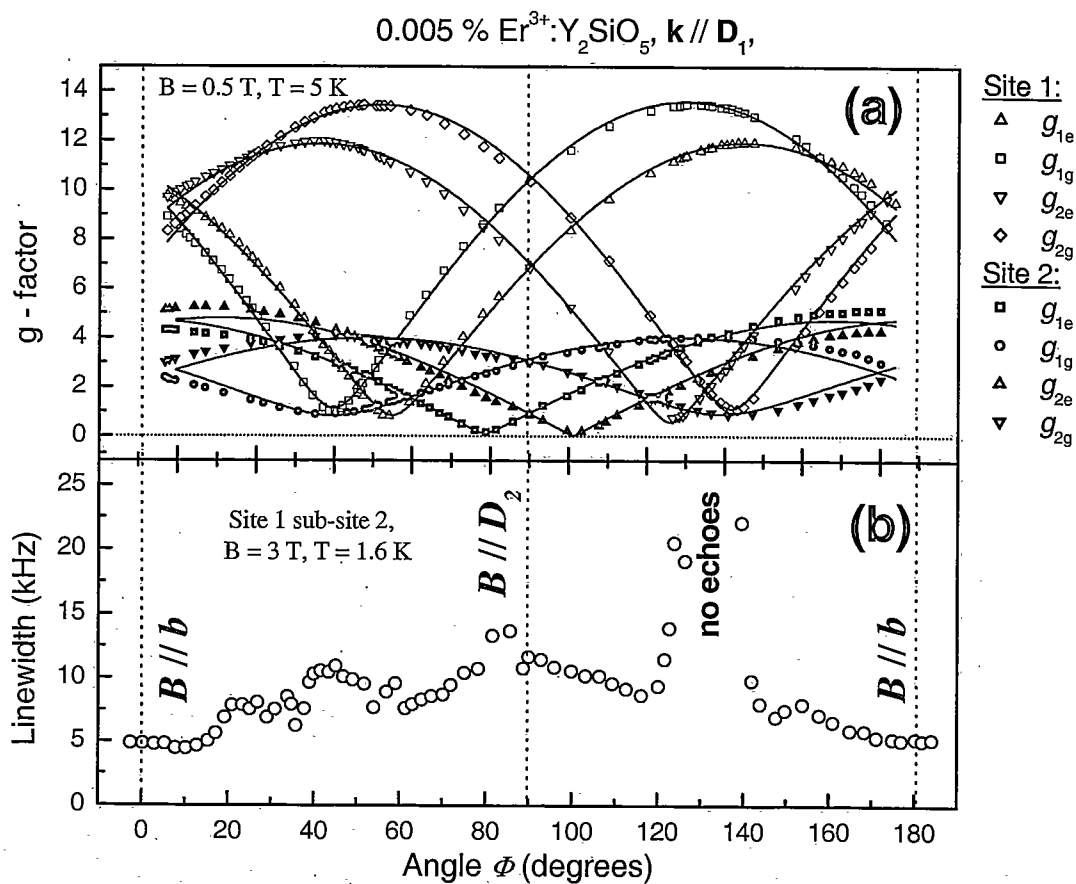


Figure 5.23 (a) Orientational dependent g values of site 1 and 2 orientations in the b - D_2 plane, g_{1g} denotes the g value for the ground state of orientation 1, g_{2e} the g value for the excited state of orientation 2, etc.; solid lines are fits to the data. (b) Correlation with the homogeneous linewidth of site 1 orientation 2 measured with two-pulse photon echoes in the b - D_2 plane as a function of magnetic field orientation.

